

COHERENTLY STIMULATED BRILLOUIN SPECTROSCOPY

By Joel N. Johnson

A Dissertation

Submitted in Partial Fulfillment
of the Requirements for the Degree of

Doctor of Philosophy
in Applied Physics and Materials Science

Northern Arizona University

May 2025

Ryan O. Behunin, Ph.D., Co-Chair

Aaron R. Hawkins, Ph.D., Co-Chair

Inès Montaño, Ph.D.

Jennifer S. Martinez, Ph.D.

David Cole, Ph.D.

ABSTRACT
COHERENTLY STIMULATED BRILLOUIN SPECTROSCOPY
JOEL N. JOHNSON

Dedication

Science is temporal arbitrage; invest in it.

Table of Contents

Abstract	ii
Dedication	iii
List of Tables	vii
List of Figures	viii
List of Acronyms	xv
1 Introduction	1
1.1 Light Scattering	4
1.2 Spontaneous Brillouin Scattering	5
1.3 Stimulated Brillouin Scattering	5
1.4 Phase-matching	5
1.5 Brillouin Gain of Materials	5
1.6 Raman Scattering	5
1.7 Raman-like Brillouin Modes	5
2 Laser Cooling of Traveling-Wave Phonons in an Optical Fiber	7
2.1 Introduction	7
2.2 Optomechanical Cooling and Heating	8
2.2.1 Physical Mechanism	8
2.2.2 Spectral Signatures of Cooling and Heating	9
2.3 Methods	9
2.3.1 CS_2 -Filled Liquid-Core Optical Fiber	10
2.3.2 Experiment A: Spontaneous Brillouin Cooling	11
2.3.3 Experiment B: Pump-Probe Verification	12
2.4 Results	14
2.4.1 Experiment A Results	14
2.4.2 Experiment B Results	14
2.4.3 Evidence of Transmission Degradation	14
2.5 Discussion	18
2.5.1 Standardized Cooling Metric	18
2.5.2 Alternative Platforms	18
2.5.3 Pathways to Net Cooling	18
2.5.4 Applications to Ground State Cooling	20
3 A Coherently Stimulated Phonon Spectrometer	27
3.1 Abstract	27
3.2 Introduction	27
3.3 Theoretical Framework	29
3.3.1 Coherently Stimulated Four-Wave Brillouin Scattering	29
3.3.2 Phase Matching Relaxation	30
3.4 Methods	31

3.4.1	Instrument Design	31
3.4.2	Experimental Techniques	33
3.5	Results	34
3.5.1	Instrument Sensitivity	34
3.5.2	Measurements	36
3.5.3	Phase Matching Bandwidth	41
3.5.4	Fano-Resonant Asymmetries at Small Signals	43
3.6	Conclusion	45
4	Brillouin-Induced Raman Modes and Device Exploration	47
4.1	Abstract	47
4.2	Introduction	47
4.3	Methods	47
4.4	Results	47
4.5	Discussion	47
5	Discussion & Future Work	49
A	Supplementary Information for Chapter 2	51
A.1	Fabrication of CS_2 -Filled Liquid-Core Optical Fiber	51
A.1.1	Splicing	51
A.1.2	Reservoir Assembly	54
A.1.3	Filling with Carbon Disulfide	58
A.1.4	Typical Optical Performance	60
A.2	Improvements in Yield and Efficiency of LCOF Samples	61
B	Supplementary Information for Chapter 3	65
B.1	Coupled-Wave Equations	65
B.1.1	Acoustic Field	66
B.1.2	Optical Fields	67
B.2	Scattered Power Comparison to Traditional Brillouin Scattering Processes	72
B.3	Observance of Fano-Resonant Asymmetries at Small Signals	77
B.3.1	Experiment A: Extended 1 cm UHNA3 Fiber Spectra	77
B.3.2	Experiment B: 1 mm CS_2 Spectra and Fano Distortions	80
B.4	Mini Experiment: Equal Contribution of Pump, Stokes, and Probe	86
B.5	Data	89
C	Supplementary Information for Chapter 4	91
C.1	Fiber-Chip-Fiber Butt-Coupling Alignment	91
D	Code and Data Availability	93
D.1	Plotting Data In Go	93
References		94

List of Tables

3.1	Measurement parameters for sensitivity measurement and calculation.	36
B.1	Parameters relevant to the coherently stimulated backward Brillouin scattering process for the example UHNA3 fiber. G_B is the effective Brillouin gain, P_P is the pump power, P_S is the Stokes power, P_{Pr} is the probe power, and $\Delta\lambda$ is the wavelength detuning of the probe from the pump.	74
B.2	Parameters relevant to the spontaneous and/or stimulated backward Brillouin scattering processes for the example UHNA3 fiber. G_B is the Brillouin gain coefficient, P_P is the pump power, ω is the optical angular frequency, Γ_B is the acoustic damping rate, k_B is Boltzmann's constant, T is the temperature, and Ω_B is the acoustic angular frequency.	75
B.3	Power values for each source (Pump, Stokes, Probe) across the three measurements, with the multiplicative total power for each setup.	86

List of Figures

1.1	Relative domains of typical frequency shifts for Rayleigh, Rayleigh-wing, Brillouin, and Raman scattering. Figure adapted from Boyd Nonlinear Optics (2020). ¹	3
1.2		5
2.1	Illustration of optomechanical heating and cooling processes. Figure 2.1a shows an incident photon of frequency ω scattering with a retreating phonon of frequency Ω , resulting in the annihilation of the incident photon and the creation of both an additional retreating phonon of frequency Ω and a backwards propagating photon of reduced frequency and thereby energy ($\omega_{\text{Stokes}} = \omega - \Omega$). Figure 2.1b shows the inverse process, whereby an incident photon, ω , scatters with an approaching phonon, Ω , annihilating the incident photon and the phonon to produce a backwards propagating photon of increased frequency and thereby energy ($\omega_{\text{anti-Stokes}} = \omega + \Omega$).	8
2.2	Schematic of liquid-core optical fiber (LCOF) design. A length of single mode fiber (SMF-28) is arc-spliced to 5-10 cm of Ultra High Numerical Aperture 7 (UHNA7) fiber, with a post-arc process applied to taper the larger SMF-28 core down to the smaller UHNA7 core for better mode matching and coupling efficiency. The UHNA7 fiber is angle-cleaved and fusion-spliced to a flat-cleaved hollow-core fiber via a heated filament in a Vytran fusion splicer system. The angle cleave results in a splice that only partially fuses the two fibers, leaving a pathway for liquid to enter the hollow core fiber via capillary action once submerged. A mirrored splice configuration on the other end of the length of hollow-core fiber allows air to escape as the fiber fills, and a reverse taper again provides improved mode matching for the light to recouple into SMF-28.	10

2.3 Schematic of experimental setup for Experiment A. In this experiment, a Continuous Wave (CW) pump laser emitting at $1.55\text{ }\mu\text{m}$ is amplified, passed through a circulator, and injected into the CS_2 -LCOF. Backscattered light is routed to a bandpass filter (BPF) for selection of Stokes or anti-Stokes frequencies and sent to a detector. A local oscillator (LO) is synthesized from the pump laser for heterodyne detection, whereby a polarization controller is used to align the polarization of the LO to that of the backscattered signal. The signal passes through a radio frequency amplifier before being sent to a radio-frequency spectrum analyzer (RFSA) for collection. Pump power is controlled by a Variable Optical Attenuator (VOA) placed just after the Erbium-Doped Fiber Amplifier (EDFA). Stokes and anti-Stokes spectra are collected sequentially for each pump power by adjusting the placement of the BPF.	12
2.4 Schematic of experimental setup for Experiment B. A pump, probe, and LO are generated from a single CW laser operating at $1.55\text{ }\mu\text{m}$. Pump light is amplified and directed through a VOA and polarization controller (PC), where its polarization is adjusted to reflect at the polarizing beam splitter (PBS). Probe light passes through a VOA for careful power control across measurement sets before being routed by a circulator to the PBS. Polarization of the probe light is adjusted for transmission through the PBS for co-injection with the pump into the LCOF. A 99-1 splitter directs 1% of the total pump and probe light to a second PBS for monitoring of respective powers injected into the LCOF. Backscattered Stokes and anti-Stokes components of both the pump and the probe retrace to the first PBS, where the respective polarization states of each ensure a re-separation of backscattered pump and probe light. The probe light is filtered by a tunable BPF and heterodyned with the LO prior to detection. Detector output is amplified by an radio frequency (RF) amplifier and fed to an RFSA for data collection.	13
2.5	15
2.6	16
2.7	17
2.8	18
2.9	19
2.10	20
2.11	21
2.12	22
2.13	23
2.14	24

2.15	25
2.16	26
3.1 Illustration of 4-Wave Brillouin Scattering	29
3.2 Design schematic of a coherently stimulated phonon spectrometer. A tunable CW laser at approximately $1.55\text{ }\mu\text{m}$ emits light that passes through an isolator (Iso) and a splitter, diverting 10% to a 27 dBm EDFA followed by a VOA. This pump light (ω_P) is polarization-controlled to reflect off a PBS and is recoupled to fiber via a fiber port (FP), then directed to the sample either by direct fiber coupling or through a pair of FPs and lenses (L) for free-space samples. After passing through the sample, the pump light traverses a corrective polarization controller that mitigates fiber twists and bends before reflecting off a second PBS, where it is routed to port (c) for power monitoring. To synthesize the Stokes wave, a 90% split from the original pump is processed through a fiber-optic intensity modulator (IM) and a fiber Bragg grating (FBG), generating a Stokes sideband downshifted from the pump by Ω . This frequency shift is swept via a signal generator to capture Ω_B . A 99/1 splitter provides a tap at port (a) to optimize Stokes synthesis. The Stokes wave (ω_S), amplified by a 1 W EDFA and VOA-controlled, counter-propagates along the pump path and is monitored at port (b). A second tunable CW laser, detuned from the pump, generates the probe wave (ω_{Pr}), which is amplified by a 1 W EDFA, attenuated variably, and polarization-controlled to pass through the initial PBS where it is incident on the sample. Backscattered signal light (ω_{Sig}) transmits back through the PBS, while unscattered probe light transmits to a power meter at port (d). A circulator parts the signal from the probe path, with an FBG filtering out any unwanted noise or Stokes light. Finally, the signal is heterodyned with an EDFA-amplified, acousto-optic modulator (AOM)-shifted LO derived from the probe laser and directed to a photodiode for detection. The resulting RF signal is mixed with an alternating current (AC) LO supplied by the signal generator which sweeps synchronously with the Stokes synthesis frequency, and collected by a lock-in amplifier for data processing.	32
3.3 $\sim 5\text{ fW}$ sensitivity measurement	35
3.4 1 cm UHNA3	38
3.5 100 μm CS_2	40
3.6 Phase-matching sinc^2 func	42

A.1 Picture of Vytran software interface camera imaging system showing a microscope view of the two fiber ends pre-splice (Section A.1.1). The left angle-cleaved fiber is the UHNA7 fiber. The right flat-cleaved fiber is the hollow-core fiber. Subsequent alignment processes, first automatic then manual fine-tuning, align the fibers in xy space for optimal fusion-splicing and optical transmission once filled.	52
A.2 Picture of both lengths of fiber braced by folded paper and two Kimwipe boxes on either side to prevent bending and flexing while transferring the delicate splice onto a glass slide (Section A.1.1).	53
A.3 Picture of splice successfully transferred onto a glass slide and tacked on either side with drops of epoxy (Section A.1.1). An arrow points to the location of the critical splice between the angle-cleaved UHNA7 fiber and the flat-cleaved hollow-core fiber.	54
A.4 Example images of LCOF splices (Section A.1.1). Figure (a) shows an earlier example of a splice which featured a large visible wedge-shaped gap for liquid to enter the hollow-core fiber. While gaps of this size were sometimes successfully transferred onto a slide, further investigation showed gaps of this scale to reduce optical transmission through the splice. This fact became critical later for collecting the data for the pump-probe experiment. Figure (b) shows images of the two splices featured on the ultimate sample which was used to gather final data for publication.	56
A.5 Picture of a complete splice assembly (Section A.1.2). The hardened epoxy around the base of the vial securely holds the cut and notched vial onto the slide, forming a sealed reservoir around the critical splice. The reservoir is later filled with liquid CS ₂ by easy removal of the screw-off cap in order to submerge the critical splice and begin the filling process of the hollow-core fiber via capillary action.	58
A.6 Picture of a complete sample under the fume hood with lights dimmed and red laser light injected into the end of the sample for monitoring (Section A.1.3). The red light is partially guided along the length of fiber which has filled with liquid CS ₂ and a thumb tack marks the progress of the CS ₂ -air interface.	59

A.7	Images of an LCOF sample in the filling process (Section A.1.3). Figure (a) shows the CS ₂ -air interface a few centimeters from the end of the length hollow-core fiber, indicated by the red dot of scattered light just underneath the epoxy tack. From this position, the meniscus will typically reach the exit splice in approximately 4 hours. Figure (b) shows evidence of a fully-filled LCOF sample, indicated by the red dot of scattered light having reached the exit splice. If the pictured reservoir were to be filled prematurely, an air bubble would be locked in, reducing full transmission through the sample to nearly 0%.	60
A.8	Images of a fully finished CS ₂ -LCOF sample (Section A.1.4). Figure (a) shows a sample secured with tape to an optical table and integrated into an optical setup. Liberal use of tape ensured the safety of the sample as well as reduced vibrations and minimized changes in the polarization of light travelling through the sample. Figure (b) shows one splice assembly secured directly to the optical table via tape. Transfer of all parts of the sample from the poster board directly onto the optical table proved critical for eliminating noise and polarization drift issues with the pump-probe experiment.	60
B.1	Comparison of scattered power from a spontaneous Brillouin scattering process and our coherently stimulated Brillouin spectrometer.	75
B.2	All measured Brillouin spectra for 1 cm UHNA3 at detuning steps of 0.5 GHz from 5 GHz (top spectrum) to 42 GHz (bottom spectrum). Each trace is offset for clarity. The resulting asymmetries highlight the characteristic Fano-resonant behavior under low signal conditions.	79
B.3	All measured Brillouin spectra for 1 mm CS ₂ at detuning steps of 0.25 GHz from 10 GHz (top spectrum) to 14 GHz (bottom spectrum). Each trace is offset for clarity.	81
B.4	Comparison of representative spectra at 11 GHz and 13 GHz, showing the positive vs. negative q asymmetry in 1 mm CS ₂ . A Fano function fit has been applied to each spectra, with χ^2 value for each fit listed in the plot legend.	83
B.5	Comparison of representative spectra at 11 GHz and 13 GHz, showing the positive vs. negative q asymmetry in 1 mm CS ₂ . Here, a naïve Lorentz function fit has been applied to each spectra, with χ^2 value for each fit listed in the plot legend. These spectra show strong Fano-resonant asymmetry and thus the standard Lorentz function offers a poor fit for these spectra, quantified by the χ^2 evaluation metric for goodness of fit as compared to the same evaluation of the Fano function fit.	84
B.6	Signal power contributions with error bars representing one standard deviation of the mean for each measurement.	87

B.7 Signal power contributions with error bars extended to two standard deviations of the mean for each measurement.	88
---	----

List of Acronyms

SBS Stimulated Brillouin Scattering

CW Continuous Wave

CoBS the Coherently stimulated Brillouin Spectrometer

AOM acousto-optic modulator

EDFA Erbium-Doped Fiber Amplifier

VOA Variable Optical Attenuator

RFSA radio-frequency spectrum analyzer

RF radio frequency

AC alternating current

DC direct current

SNR signal-to-noise ratio

LO local oscillator

BPF bandpass filter

PBS polarizing beam splitter

FP fiber port

PC polarization controller

FBG fiber Bragg grating

IM fiber-optic intensity modulator

LCOF liquid-core optical fiber

UHNA7 Ultra High Numerical Aperture 7

UHNA3 Ultra High Numerical Aperture 3

SMF-28 single mode fiber

Chapter 1

Introduction

Optomechanics is the study of light-matter interactions; it is the study of how the intangible (light) can affect change in the tangible (matter) and vice versa. Injecting light into a material under specific conditions allows for an exchange of energy to occur between the light and the mechanical oscillations of the material which changes the mechanical energy of the material. This interaction can be controlled to deposit or withdraw mechanical energy into/from a system and thus leave the system in a more, or less, mechanically energetic state respectively. The same interaction can also be harnessed for passive observation of material properties. Mechanical systems from bulk to atomic scales can be probed and characterized with light by retrieving the inelastically scattered light resulting from interaction with the material. This retrieved light contains embedded information about the energy exchange that occurred, which, when considered as part of a population of scattering events, reveals natural resonances of a mechanical system.

Optomechanics comprises a broad range of phenomena involving the interaction of optical and mechanical systems, from basic photothermal absorption to more complex nonlinear processes. This section offers a brief overview of notable optomechanical phenomena and the remainder of this chapter is devoted to a more detailed description of the specific interactions that play a role in the research detailed in this document. Photothermal absorption is the process by which light is absorbed by a material, leading to an increase in temperature of the material and consequent changes in the material's dimensions (thermal expansion) or refractive index (thermo-optic effect). This effect has applications in optical switches, actuators, and sensors. Photothermal therapy in medicine is an emerging application of this effect, where light is used to target and heat specific areas, causing localized damage to diseased tissue. This technique becomes especially effective when combined with nanoparticle-enhanced absorption, allowing for dramatically increased absorption in ultra-localized zones within the body.

Light scattering, in its many forms, is also an optomechanical process as it involves the interaction of an optical field with the fluctuation, motion, or vibration of matter. Rayleigh scattering, perhaps the most well-known example, is the elastic scattering of light by particles much smaller than the wavelength of the

incident light, leading to scattering in possibly a new direction but without a change in wavelength. It is responsible for the blue color of the sky because the efficiency of Rayleigh scattering is inversely proportional to the fourth power of the wavelength (λ) of the light ($\frac{1}{\lambda^4}$) and so shorter (blue) wavelengths are scattered much more than longer (red) wavelengths by the molecules in the atmosphere.²

Raman scattering is the interaction of light with vibrational and rotational modes within a material (often molecular), resulting in scattered light with frequencies that are shifted from the incident light. This inelastically scattered light provides insights into the material's molecular structure and properties. Raman scattering is widely used in chemical and material science for identifying chemical compounds, analyzing molecular structures, and studying molecular dynamics. It finds application in the characterization of pharmaceuticals, monitoring changes in biological tissues for medical diagnostics, and investigation of stress and temperature distributions in engineering materials, among others.

Brillouin scattering, around which much of the work detailed in this document is centered, is the scattering of light with acoustic phonons or coherent traveling density waves in a material, resulting in scattered light with a frequency that is slightly shifted from the incident light. This inelastically scattered light reveals mechanical properties of the material such as its bulk and elastic moduli. This phenomenon is used in materials science to measure elastic properties and viscoelasticity of materials, in fiber optic sensing to monitor temperature and strain over large distances, and in physics to study phase transitions and mechanical properties of crystals, liquids, and gases.

Rayleigh-wing scattering is the broad, smooth extension of the Rayleigh scattering spectrum that results from interactions with low-frequency excitations in a material, providing insights into dynamic processes like rotational and translational diffusion of molecules that make up a material. This scattering is particularly useful in studying the dynamics of complex fluids, gases, and soft materials, where it can reveal information about molecular orientation, diffusion rates, and interactions within the medium. Applications include the analysis of atmospheric phenomena, characterization of liquid crystals, and investigations into the properties of polymers and biological materials, aiding in the understanding of their behavior at the molecular level.

Figure 1.1 shows the relative domains of typical frequency shifts for Rayleigh, Rayleigh-wing, Brillouin, and Raman scattering. Rayleigh-wing scattering is broad and shares part of its domain with Brillouin scattering. This makes sense because for any given molecule and within the timescale that it occurs, diffusive translational motion can be thought of as indistinguishable from motion caused by traveling density waves that host brillouin scattering. In this way, Rayleigh-wing scattering represents a sporadic distribution of fleeting, localized Brillouin scattering. Of course, the difference between incoherent diffusion of molecules and coherently traveling acoustic modes within a material is an important distinction. However, this thought experiment offers a perspective for bridging the gap between Rayleigh-wing and Brillouin scattering and for

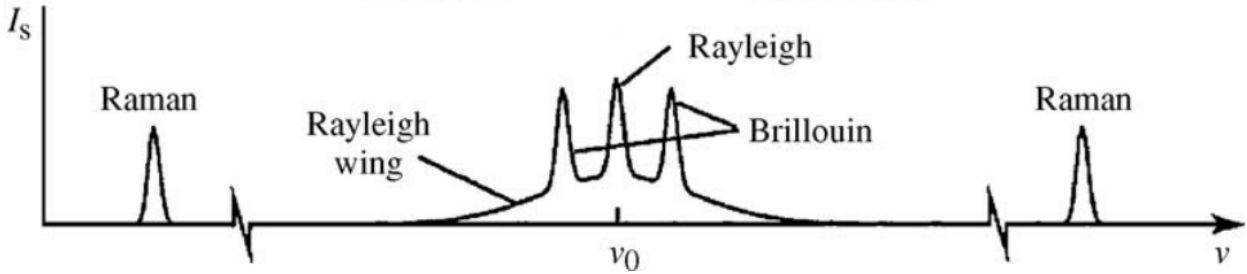


Figure 1.1: Relative domains of typical frequency shifts for Rayleigh, Rayleigh-wing, Brillouin, and Raman scattering. Figure adapted from Boyd Nonlinear Optics (2020).¹

understanding their common frequency domains. Moreover, it serves as a reminder of the rich continuum of material behavior and responses that affect light scattering as opposed to the distinct categories we ascribe for convenience. This is a core concept of the research described in further chapters.

Returning to other optomechanical phenomena beyond scattering processes, the momentum of photons can exert forces on objects, leading to phenomena like radiation pressure, optical tweezing, and optical trapping. These effects are widely used in manipulating microscopic particles, biological cells, and atoms, enabling studies of single molecules, cold atoms, and quantum computing elements.

The final category of optomechanical interactions to be noted here is that of nonlinear optical phenomena. Second harmonic generation, parametric oscillation, and four-wave mixing all feature the interaction between light and material nonlinearities that lead to the generation of new light frequencies.¹ The Kerr effect is the change in the refractive index of a material in response to an applied electric field, which can be induced optically with sufficient intensities of light. In general, nonlinear optical responses of materials are often only accessible with the use of high intensity laser light. This is emphasized by the fact that the field of nonlinear optics can be traced back to the discovery of second-harmonic generation in 1961³, just one year after the first demonstration of the laser by American physicist Theodor Maiman.⁴ These nonlinear effects provide the foundation for a range of technologies, including high-speed optical communication systems, frequency converters, and lasers for materials processing.

Also included within nonlinear optical phenomena is electrostriction. Electrostriction is a reversible material deformation induced by an electric field, which can be generated by light in electro-optic materials. This effect is quadratic, scaling with the square of the applied electric field, and hence a nonlinear optical effect. At sufficiently high intensities, electrostrictive forces serve to enhance Brillouin scattering whereby the scattered light electrostrictively reinforces the acoustic wave that caused its scattering, leading to a nonlinear positive feedback loop known as Stimulated Brillouin Scattering (SBS). Photostriction is a related phenomenon that occurs when light absorption causes a change in the lattice structure of a material, leading to mechanical strain. It combines photovoltaic and piezoelectric effects and can be seen as an optically

induced strain. These effects are utilized in designing optical modulators, tunable photonic devices, and smart materials that respond to light.

The remainder of this chapter further describes the specific optomechanical phenomena that pertain to the research presented in this document: Brillouin scattering, electrostriction as it pertains to the SBS process, and Raman scattering.

1.1 Light Scattering

Light scattering involves the redirection of light as a result of interactions with the constituent particles or molecules within a material medium. In every case, light scattering occurs because of variations in the material's optical properties. To understand why, envision a material with completely uniform particles—spatially and temporally consistent, or in other words, perfectly homogeneous. Figure 1.2 shows an incident optical plane wave encountering a segment of such a material, denoted δz , containing a volume element δV_1 . For any given incident wavelength λ and any non-zero scattering angle θ at volume δV_1 , there exists a corresponding volume element δV_2 , located a distance $\frac{\lambda}{2\sin\theta}$ apart, which scatters light at the same angle θ . The scattered waves from δV_1 and δV_2 would be out of phase by $\frac{\lambda}{2}$, leading to perfect destructive interference and no resultant scattered field. Thus, to achieve observable scattering, the material must possess inhomogeneities, allowing for variations in the optical properties between neighboring volumes. Fortunately, perfect homogeneity is not characteristic of real materials; all matter undergoes thermodynamic fluctuations at any temperature above absolute zero, and quantum fluctuations are inherent even at the ground state.

We now begin with a theoretical description of spontaneous light scattering as a result of thermodynamic fluctuations, presented in Boyd Nonlinear Optics.¹ This foundation will serve as a framework for distinguishing between light that scatters as a result of coherent propagating pressure or density variations (Brillouin scattering) and light that scatters as a result of static or random thermodynamic variations (Rayleigh scattering). Later we will treat the case of higher-intensity SBS. Ultimately we will build upon this theoretical basis to derive the coupled-wave equations of the Coherently stimulated Brillouin Spectrometer (CoBS), a novel instrument which underpins many of the results presented in future chapters. To begin building a theoretical description of light scattering, we consider thermodynamic fluctuations as the origin of the scattering process.

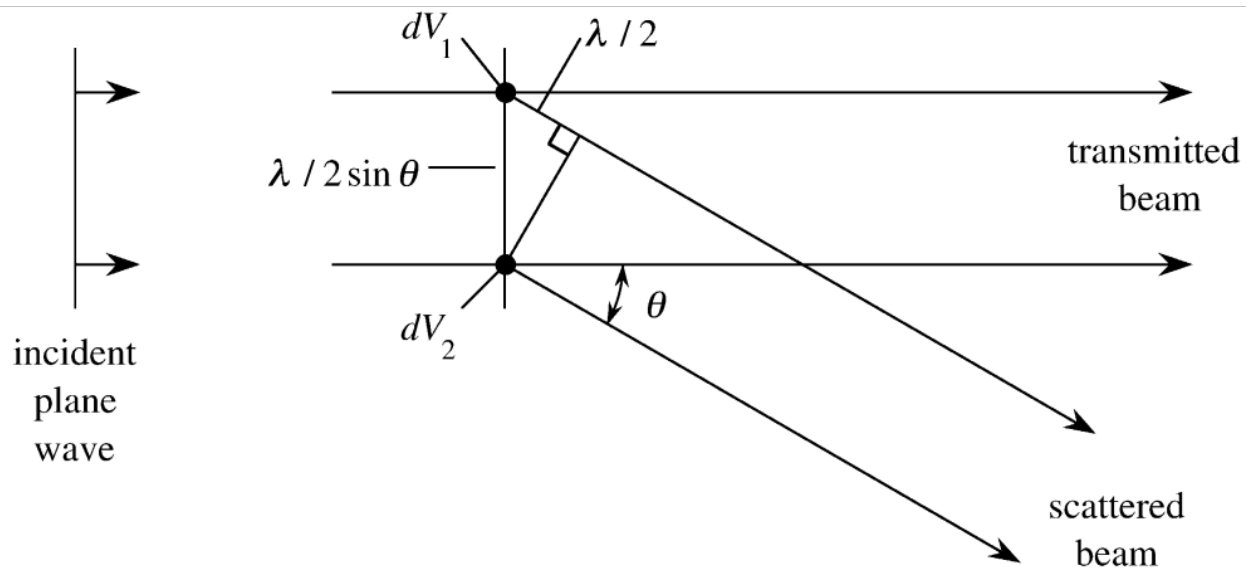


Figure 1.2

1.2 Spontaneous Brillouin Scattering

1.3 Stimulated Brillouin Scattering

1.4 Phase-matching

1.5 Brillouin Gain of Materials

1.6 Raman Scattering

1.7 Raman-like Brillouin Modes

Chapter 2

Laser Cooling of Traveling-Wave Phonons in an Optical Fiber

Joel N. Johnson^{1,2}, Danielle R. Haverkamp^{1,2}, Yi-Hsin Ou³, Khanh Kieu³, Nils T. Otterstrom⁴, Peter T. Rakich⁵, Ryan O. Behunin^{1,2}

This chapter elaborates on experiments and results related to the demonstration of optomechanical cooling of traveling wave phonons in optical fiber which have been published as an article by the same name in Physical Review Applied by Johnson et al. (2023)⁵. Any discrepancies, omissions, or errors that may exist between the published paper and this dissertation chapter are the sole responsibility of the author, as the text, analyses, and interpretations herein represent an independent and original presentation of the work.

2.1 Introduction

Materials above the ground state experience thermodynamic variations such as temperature and density. These thermal fluctuations alter the optical properties of a given material, allowing a scattering process to occur (see Section 1.1). Spontaneous Brillouin scattering is the inelastic scattering of light with these thermal fluctuations within a material, facilitating an energy exchange between the optical and acoustic domains. While a given medium typically supports a multitude of thermally excited acoustic modes (including both transverse and longitudinal modes) we focus here specifically on longitudinally travelling acoustic waves to demonstrate cooling in a continuous (non-resonant) system.

[lit review, state of the art]

¹ Department of Applied Physics and Materials Science, Northern Arizona University, Flagstaff, AZ 86011, USA

² Center for Materials Interfaces in Research and Applications, Flagstaff, AZ 86011, USA

³ College of Optical Sciences, University of Arizona, Tucson, AZ, USA

⁴ Photonic and Phononic Microsystems, Sandia National Laboratories, Albuquerque, New Mexico, USA

⁵ Department of Applied Physics, Yale University, New Haven, CT, USA

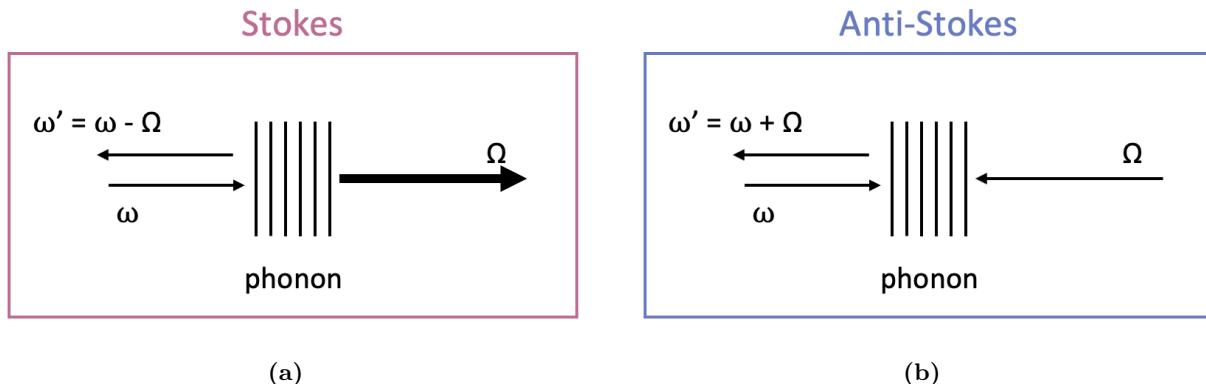


Figure 2.1: Illustration of optomechanical heating and cooling processes. Figure 2.1a shows an incident photon of frequency ω scattering with a retreating phonon of frequency Ω , resulting in the annihilation of the incident photon and the creation of both an additional retreating phonon of frequency Ω and a backwards propagating photon of reduced frequency and thereby energy ($\omega_{\text{Stokes}} = \omega - \Omega$). Figure 2.1b shows the inverse process, whereby an incident photon, ω , scatters with an approaching phonon, Ω , annihilating the incident photon and the phonon to produce a backwards propagating photon of increased frequency and thereby energy ($\omega_{\text{anti-Stokes}} = \omega + \Omega$).

2.2 Optomechanical Cooling and Heating

2.2.1 Physical Mechanism

Backward Brillouin scattering targets longitudinally traveling acoustic waves (or phonons) through two complementary processes—Stokes and anti-Stokes, illustrated in Figures 2.1a and 2.1b, respectively. In the Stokes process, an incident photon of frequency ω scatters with a *retreating* phonon of frequency Ω annihilating the *photon* and creating both an additional phonon of frequency Ω and a backscattered photon at the difference energy ($\omega_{\text{Stokes}} = \omega - \Omega$). In this way, both energy and momentum are conserved. This can be visualized by an analogy, in which the incident light experiences a doppler *down*-shift in frequency as though the photon were reflected from a retreating mirror. Since this process results in an increase in the phonon population within the respective longitudinal mode of the material, this process is referred to as optomechanical heating. The energy lost by the light is gained by the material in the form of mechanical vibrations.

The anti-Stokes process is the inverse process, whereby an *approaching* phonon of frequency Ω scatters with an incident photon of frequency ω , annihilating the *phonon* and creating a backscattered photon at the addition energy ($\omega_{\text{anti-Stokes}} = \omega + \Omega$). Both energy and momentum are again conserved, however in the anti-Stokes process, the incident light experiences a doppler *up*-shift in frequency as if, to continue the analogy, the photon were reflected from an approaching mirror.

2.2.2 Spectral Signatures of Cooling and Heating

Spectral amplitude provides a measure of the power of the backscattered light, increasing with both pump power P_P as well as temperature T of the phonon mode (see Equation B.50 in Appendix B.2). As a result, both Stokes and anti-Stokes spectral amplitudes increase with increasing pump power, but at unequal rates respective of pump power. With increasing pump power, the anti-Stokes scattering process serves to cool the anti-Stokes phonon mode, partially discounting the scattered power of the anti-Stokes light collected by the detector. The simultaneous Stokes process experiences an inverse effect, whereby increasing pump power serves to heat the Stokes phonon mode, contributing to an increase in scattered power of Stokes light collected by the detector. The overall effect of these processes is a sublinear growth in amplitude of the anti-Stokes spectrum and superlinear growth of the Stokes spectrum.

2.3 Methods

While spontaneous Brillouin scattering processes naturally alter phonon populations (and thus mode temperatures), practical demonstration and detection of these effects pose significant challenges. Foremost among these is the requirement to remain in the spontaneous regime: we wish to probe the natural thermal phonons in a medium, so we cannot rely on artificially driving the mechanical modes to enhance scattered power (see Appendix B.2, and specifically Figure B.1, for a comparison of scattered power produced by different Brillouin techniques). Although stimulated Brillouin scattering (SBS) is often employed to boost signal levels, it actively drives phonon populations via injected optical fields, and thus no longer measures the intrinsic thermal phonons. In practical terms, SBS occurs when the overall process gain factor $G = G_B P_P L$ (where G_B is the effective Brillouin gain, P_P the pump power, and L the effective length) far exceeds unity ($G \gg 1$).

To demonstrate optomechanical cooling (i.e., an anti-Stokes process that lowers phonon energy), one must detect scattered light from a mode whose phonon population has been reduced. This is intrinsically difficult because a decreased phonon population means fewer scattering events, and hence diminished backscattered light. Consequently, an ideal testbed should provide sufficiently high single-pass gain (overall gain factor near unity) to enable clear detection, yet remain below the threshold that would drive the process into the stimulated regime. Achieving this balance ensures that measurements reflect genuine spontaneous cooling of a thermally populated phonon mode, rather than an artifact of optically driven phonons.

In addition to the requirement that the overall process gain be near but below unity, temporal constraints impose further critical conditions. Specifically, the rate at which phonons are removed from the system must exceed the rate at which they are replenished by the thermal bath to ensure net cooling of the anti-Stokes mode. This condition demands that backscattered photons leave the system rapidly, carrying away the

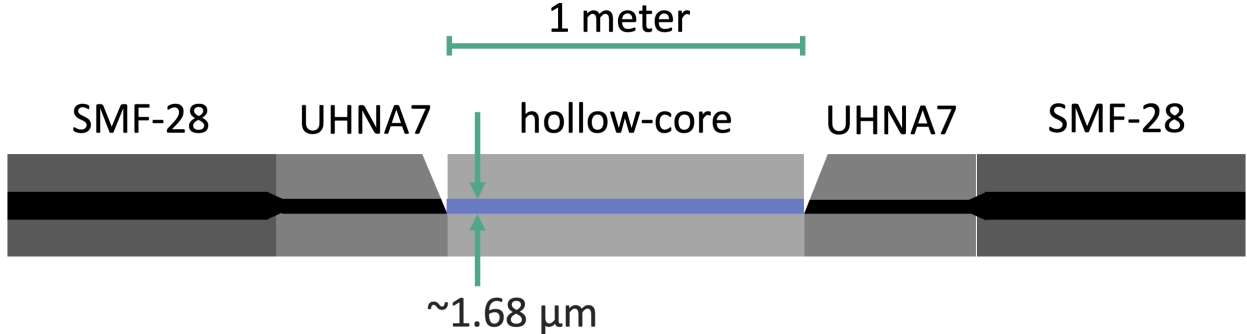


Figure 2.2: Schematic of liquid-core optical fiber (LCOF) design. A length of single mode fiber (SMF-28) is arc-spliced to 5-10 cm of Ultra High Numerical Aperture 7 (UHNA7) fiber, with a post-arc process applied to taper the larger SMF-28 core down to the smaller UHNA7 core for better mode matching and coupling efficiency. The UHNA7 fiber is angle-cleaved and fusion-spliced to a flat-cleaved hollow-core fiber via a heated filament in a Vytran fusion splicer system. The angle cleave results in a splice that only partially fuses the two fibers, leaving a pathway for liquid to enter the hollow core fiber via capillary action once submerged. A mirrored splice configuration on the other end of the length of hollow-core fiber allows air to escape as the fiber fills, and a reverse taper again provides improved mode matching for the light to recouple into SMF-28.

extracted mechanical energy. A mean-field analysis (see Appendix A of Johnson et al. (2023)⁵) shows that the relevant depletion rate is $4v_g/L$, where v_g is the group velocity of the anti-Stokes light and L is the system length. This must exceed the mechanical dissipation rate Γ_0 , which represents the natural return of the phonon mode to thermal equilibrium. Hence, a suitable platform for demonstrating optomechanical cooling of traveling-wave phonons must fulfill the fast escape condition $4v_g/L > \Gamma_0$. Meeting this requirement on system length, however, directly conflicts with the desire for a sufficiently high overall gain factor, illustrating the delicate balance needed for effective cooling.

2.3.1 CS_2 -Filled Liquid-Core Optical Fiber

To demonstrate optomechanical cooling of traveling wave phonons, we utilize 1 m of liquid-core optical fiber filled with carbon disulfide, first developed by Kieu et al. (2012).⁶ This platform features large optomechanical coupling due to the high electrostrictive response of CS_2 ¹ and the small effective area defining acousto-optic mode overlap offered by the small 0.9 μm core radius of the capillary fiber. These characteristics of the LCOF system combine to produce an effective Brillouin gain coefficient $G_B \sim 2.3 \text{ W}^{-1} \text{ m}^{-1}$, enabling sufficient scattering within the relatively short length required to satisfy the fast-escape condition $4v_g/L > \Gamma_0$ ($4v_g/L \approx 0.82 \text{ GHz}$ and $\Gamma_0 \approx 0.61 \text{ GHz}$).⁵ Additionally, this CS_2 -filled LCOF system provides excellent acoustic and optical guidance due to the large electromagnetic and acoustic impedance differential between the CS_2 core and surrounding silica.⁷

Figure 2.2 shows a schematic of the LCOF design. Coupling into and out of the LCOF is facilitated by a short length of tapered UHNA7 for better mode matching between the $4.8\text{ }\mu\text{m}$ core radius SMF-28 and the $0.84\text{ }\mu\text{m}$ core radius of the capillary fiber. An angled cleave of the UHNA7 fiber allows for a small wedge gap to remain after fusion splicing to the capillary fiber. This gap allows liquid CS_2 to enter and fill the hollow core of the capillary fiber via capillary action. Appendix A.1 describes the fabrication and filling processes of the LCOF and details key insights which contributed to significant reductions in failure rate as well as time and material cost of sample preparation.

2.3.2 Experiment A: Spontaneous Brillouin Cooling

We conducted two independent experiments to demonstrate and verify laser cooling of traveling wave phonons in our CS_2 -LCOF platform. The first experiment (Experiment A) employs a pump laser to launch $1.55\text{ }\mu\text{m}$ light into the LCOF. The backscattered Stokes and anti-Stokes components are filtered and collected by a detector. In this experiment, evidence of cooling is given by symmetry breaking between the amplitudes and widths of the Stokes and anti-Stokes spectra as pump power is varied.

Figure 2.3 shows a schematic diagram of the experimental setup for Experiment A. A Continuous Wave (CW) pump laser emitting at $1.55\text{ }\mu\text{m}$ (ω_P) is amplified by an Erbium-Doped Fiber Amplifier (EDFA) and its power is controlled by a Variable Optical Attenuator (VOA). This light is subsequently routed via a circulator to the CS_2 -LCOF, where some of the light backscatters within the length of the LCOF. Backscattered light is frequency-shifted, up for anti-Stokes ($\omega_{\text{aS}} = \omega_P + \Omega_B$) and down for Stokes ($\omega_S = \omega_P - \Omega_B$), by a band of frequencies centered around the Brillouin frequency of the LCOF ($\Omega_{B,\text{LCOF}} \approx 2.27\text{ GHz}$). Backscattered light is routed by circulators to a 5 GHz bandpass filter (BPF) to allow selection of either the Stokes or anti-Stokes light while also reducing unwanted frequency noise. The filtered signal is then incident on a photodiode detector sensitive to GHz frequencies. A local oscillator (LO) is synthesized from the pump laser, polarization controlled, amplified, and combined with the signal pre-detector for heterodyne detection. Output from the detector is amplified with a radio frequency (RF) amplifier and sent to a radio-frequency spectrum analyzer (RFSA) for data collection.

To conduct the experiment, pump power was varied from 10 mW to 290 mW in increments of 10 mW , as measured pre-injection into the LCOF, and respective Stokes and anti-Stokes spectra for each pump power were collected sequentially by tuning the placement of the BPF. Optical transmission through the entire LCOF sample which was used for the published data was measured to be 17% , giving $100\sqrt{0.17} \approx 41\%$ transmission through just the first splice assuming equal transmission through both LCOF splices. This provides a scaling factor for obtaining intrafiber powers from injected pump power ($P_{\text{intrafiber}} = \sqrt{0.17}P_P$)

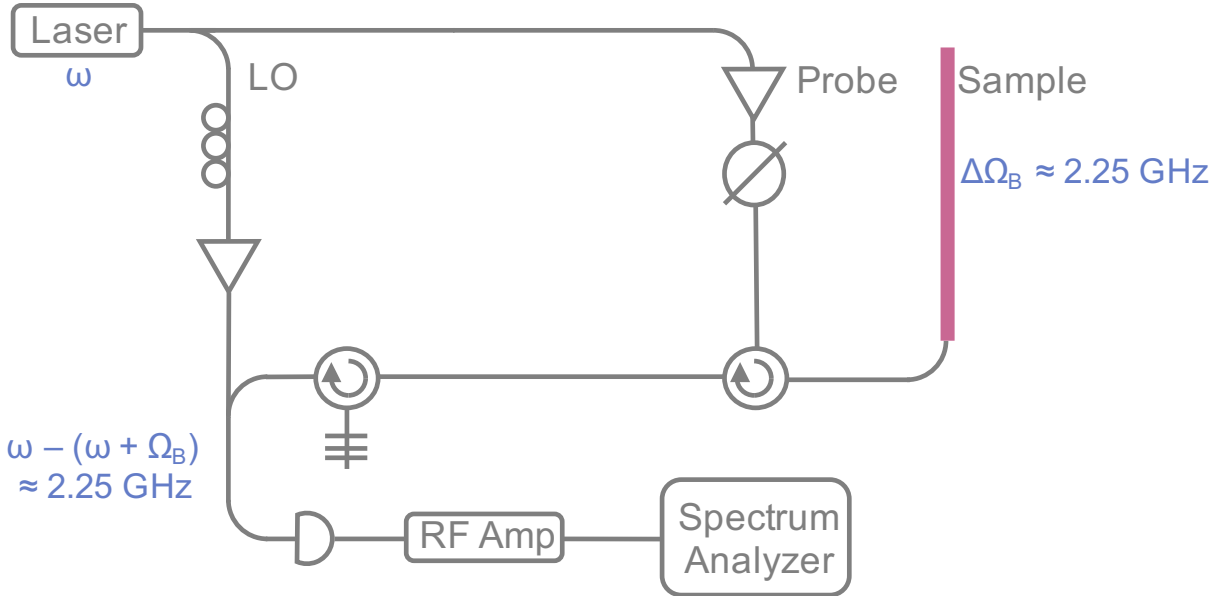


Figure 2.3: Schematic of experimental setup for Experiment A. In this experiment, a CW pump laser emitting at $1.55 \mu\text{m}$ is amplified, passed through a circulator, and injected into the CS_2 -LCOF. Backscattered light is routed to a BPF for selection of Stokes or anti-Stokes frequencies and sent to a detector. A LO is synthesized from the pump laser for heterodyne detection, whereby a polarization controller is used to align the polarization of the LO to that of the backscattered signal. The signal passes through a radio frequency amplifier before being sent to a RFSA for collection. Pump power is controlled by a VOA placed just after the EDFA. Stokes and anti-Stokes spectra are collected sequentially for each pump power by adjusting the placement of the BPF.

which was used for data processing and analysis.

2.3.3 Experiment B: Pump-Probe Verification

A second experiment (Experiment B) was conducted to provide direct evidence of cooling via a pump-probe spectroscopy technique, whereby a separate probe laser is held at constant power while a pump laser is varied to affect cooling in the LCOF. In Experiment B, backscattered light from the probe laser provides direct evidence of cooling through spectral changes in amplitude and width as pump power is independently varied. To achieve independence of the pump and probe, probe light was controlled to be polarized orthogonal to the pump.

Figure 2.4 shows a schematic of the experimental design for Experiment B. Starting from a single CW laser operating at $1.55 \mu\text{m}$, we generate a pump ω_P , probe ω_{P_r} , and LO. A polarizing beam splitter (PBS) combines the pump and probe for co-injection into the LCOF. The pump light is amplified by an EDFA, and its polarization is adjusted so that it reflects at the PBS for launching into the LCOF. The probe light passes through a circulator and is polarization-adjusted to transmit through the PBS for injection into the

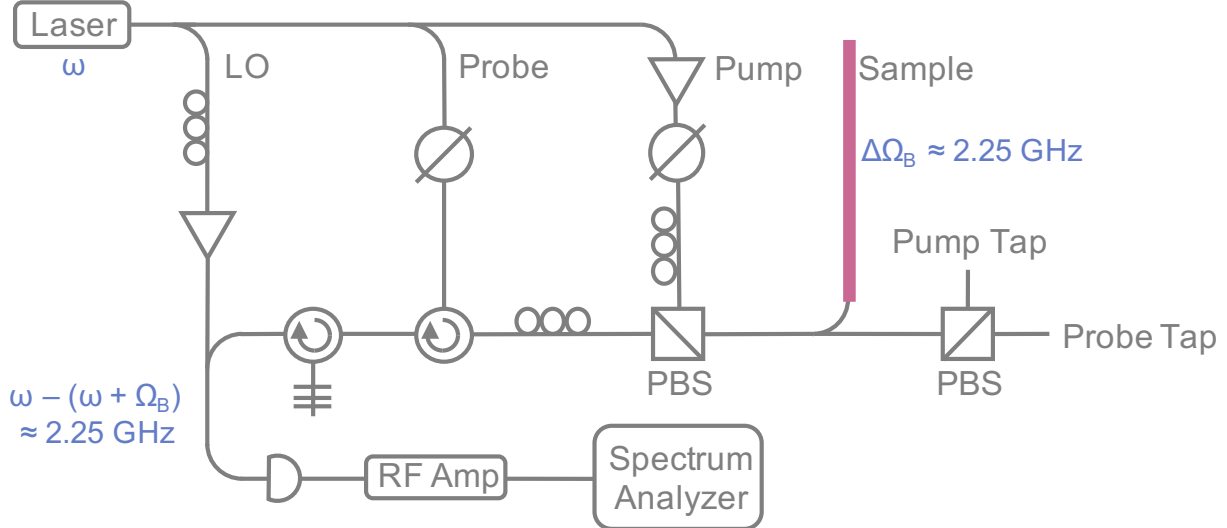


Figure 2.4: Schematic of experimental setup for Experiment B. A pump, probe, and LO are generated from a single CW laser operating at $1.55\text{ }\mu\text{m}$. Pump light is amplified and directed through a VOA and polarization controller (PC), where its polarization is adjusted to reflect at the PBS. Probe light passes through a VOA for careful power control across measurement sets before being routed by a circulator to the PBS. Polarization of the probe light is adjusted for transmission through the PBS for co-injection with the pump into the LCOF. A 99-1 splitter directs 1% of the total pump and probe light to a second PBS for monitoring of respective powers injected into the LCOF. Backscattered Stokes and anti-Stokes components of both the pump and the probe retrace to the first PBS, where the respective polarization states of each ensure a re-separation of backscattered pump and probe light. The probe light is filtered by a tunable BPF and heterodyned with the LO prior to detection. Detector output is amplified by an RF amplifier and fed to an RFSA for data collection.

LCOF. A 99-1 splitter directs 1% of the combined pump and probe light to a second PBS for monitoring of respective powers injected into the LCOF.

Backscattered light from both pump and probe is shifted in frequency by approximately the Brillouin frequency of the LCOF ($\Omega_{B,\text{LCOF}} \approx 2.27\text{ GHz}$). The Stokes components (downshifted) satisfy

$$\omega_{P,S} = \omega_P - \Omega_B, \quad \omega_{Pr,S} = \omega_{Pr} - \Omega_B, \quad (2.1)$$

while the anti-Stokes components (upshifted) satisfy

$$\omega_{P,aS} = \omega_P + \Omega_B, \quad \omega_{Pr,aS} = \omega_{Pr} + \Omega_B. \quad (2.2)$$

These four backscattered signals are centered within a band of frequencies due to the finite phonon lifetime

in the LCOF. The polarization state of the backscattered pump and probe light is recovered after retracing their paths, permitting only probe light to transmit through the PBS for filtration and heterodyne detection. Output from the detector is again amplified by an RF amplifier and routed to an RFSA for data collection. With the probe power inside the LCOF held constant, changes in the amplitude and width of the probe spectra provide direct evidence of laser cooling from varying pump powers within the LCOF.

2.4 Results

2.4.1 Experiment A Results

Figures 2.5 and 2.6 show the respective Stokes and anti-Stokes spectra gathered across a range of intra-fiber pump power from 4.12 mW to 119.57 mW. Both Stokes and anti-Stokes spectra sets are centered at approximately $f_B = 2.27 \text{ GHz}$, representing a respective up- and downshift from the pump frequency by the Brillouin frequency of the CS₂-LCOF at 1.55 μm. For increasing pump power, we see an asymmetry in evolution of peak spectral density between Stokes and anti-Stokes. The anti-Stokes peak amplitudes increase sublinearly while that of the Stokes increase superlinearly. This is a key fingerprint of optomechanical cooling. As phonon occupation decreases (cooling) in the anti-Stokes phonon mode, the rate of scattering also decreases due to the diminished population of phonons able to participate in scattering. A lesser rate of scattering produces less backscattered light incident on the detector, causing the peak spectral density to be less than if no cooling had occurred. The opposite effect occurs in the Stokes process; as phonon occupation increases (heating) in the Stokes phonon mode, the rate of scattering also increases owing to a bolstered number of phonons available to participate in scattering. This increased rate of scattering results in more backscattered light collected by the detector and causing the peak spectral density to be greater than if no heating had occurred. Critically, since scattered power is also dependent on pump power (see Equation B.50), the peak amplitude of both processes increases with increasing pump power. However, the sublinear (superlinear) growth rate in peak amplitude of the anti-Stokes (Stokes) spectra as pump power increases provides key evidence of optomechanical cooling (heating) of the respective LCOF phonon modes.

2.4.2 Experiment B Results

2.4.3 Evidence of Transmission Degradation

After comparing the anti-Stokes linewidths measured in Experiments A and B, we conclude that significant splice transmission degradation occurred in the interim. Experiment B was performed first (with a through-fiber transmission of 17%), followed by Experiment A a few days later. If the experimental conditions

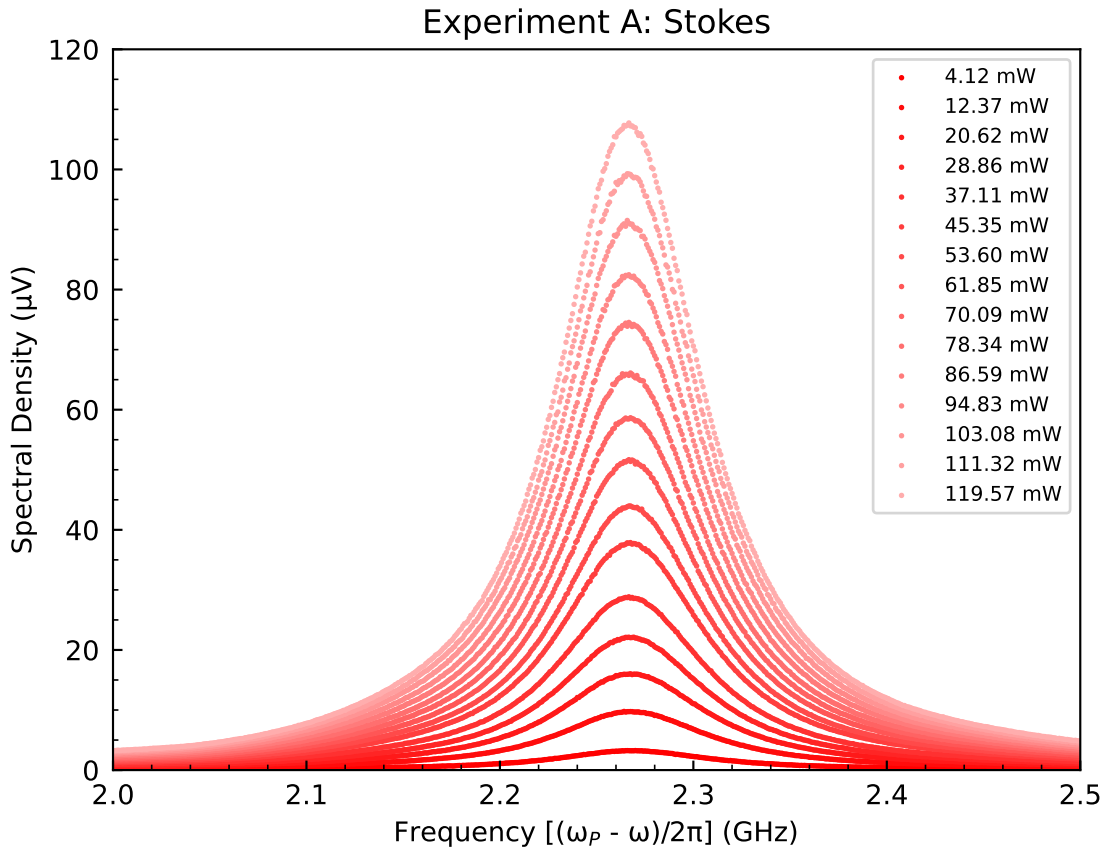


Figure 2.5: .

were unchanged between the two experiments, the slopes of the anti-Stokes linewidth versus pump power would be identical (Figures 2.8 and 2.15). Instead, Experiment B exhibits a noticeably steeper slope than Experiment A. A reanalysis shows that reducing the assumed transmission for Experiment A so the two slopes match would require the total fiber transmission to have dropped from 17% down to approximately 3%. While large, this degradation is plausible and is supported by several further observations.

First, the fiber immediately following the exit splice of the LCOF broke off after Experiment B, making it no longer possible to remeasure the full through-fiber transmission during Experiment A. If that transmission had declined in the meantime, we had no direct means to detect it. Additionally, during both experiments, the pump power was recorded via a 1% tap prior to launching into the LCOF. Hence, any losses incurred at the damaged splice were not accounted for. As a result, if the splice transmission had indeed worsened, we overestimated the actual intracore power in Experiment A.

Further quantitative analysis supports this hypothesis as well. As we reported in Johnson et al. (2023)⁵, Experiment A yields a Brillouin gain of roughly $2.3 \text{ W}^{-1} \text{ m}^{-1}$, calculated using

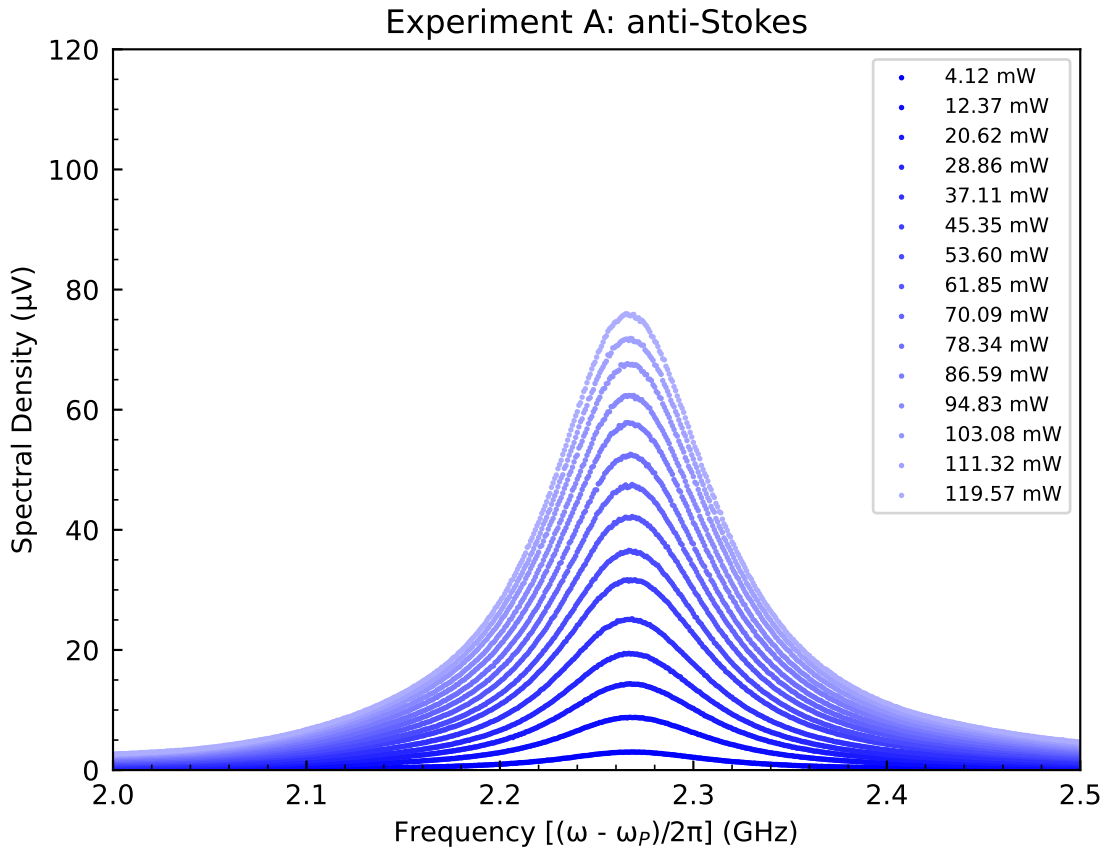


Figure 2.6: .

$$\Gamma_{\pm} \approx \Gamma_0 \left(1 \pm \frac{1}{4} G \right), \quad (2.3)$$

where is the overall process gain factor $G = G_B P_P L$ (see Section B.2). This value is smaller than the $5.8(1) \text{ W}^{-1} \text{ m}^{-1}$ reported by Behunin et al. in 2019⁷ for a near-identical LCOF geometry and fabrication method. If instead we calculate the Brillouin gain from Experiment B data, this results in a Brillouin gain of approximately $8.1(2) \text{ W}^{-1} \text{ m}^{-1}$, which is in excellent agreement with the prior published value from the literature. In estimating the uncertainty here we have taken the 2σ confidence level in linewidths and allowed a 10% uncertainty in intracore pump powers. The natural explanation is that for Experiment A we overstated the intrafiber pump power due to significant splice transmission degradation between experiments, causing an underestimation the true gain of the LCOF.

Finally, the linewidth vs power plots appear to exhibit a slight sublinear trend (especially that of Experiment B), but any saturation effect or similar which could cause a sublinear trend in linewidths with

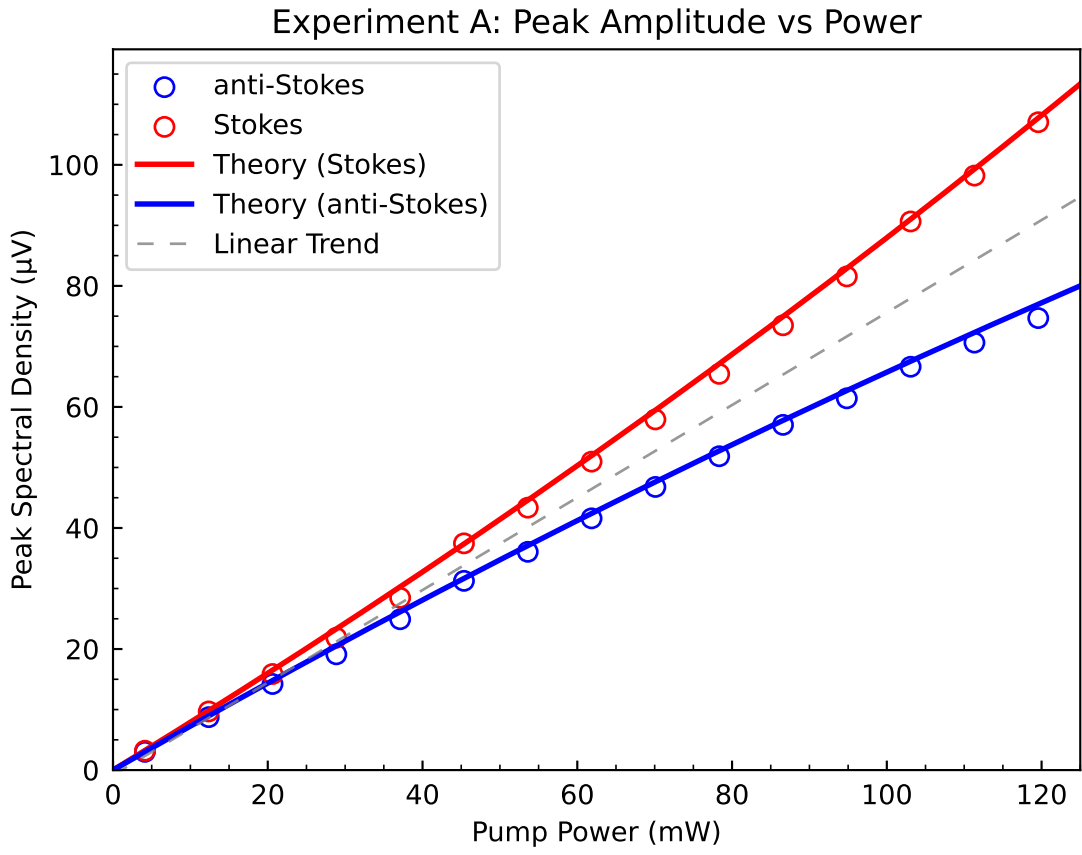


Figure 2.7: .

pump power should activate at the same intracore optical power. However, with our two data sets, a slight sublinear trend invoked by the much higher pump powers used in Experiment A should then not cause the same saturation effect for the much lower pump powers used in Experiment B, if the optical transmission were the same across experiments. If instead the transmission of the LCOF splice at entrance had been significantly greater for the earlier-run Experiment B than for Experiment A, the intracore powers for Experiment B could have been similar or far greater than those for Experiment A. This might explain why Experiment B linewidths appear to exhibit slightly sublinear growth with pump power despite the lower pump powers launched into the LCOF. Experiment A in fact does not seem to exhibit as apparent of a sublinear growth trend in linewidths as is seen for Experiment B. This is consistent with an approximate factor of 5 drop in transmission through the LCOF splice at the time Experiment A was performed, as indicated by the discrepancy in linewidth growth rates between experiments.

In summary, all these lines of evidence indicate that the LCOF splice transmission fell substantially between Experiments B and A, plausibly on the order of a factor of five. This fully reconciles the differing

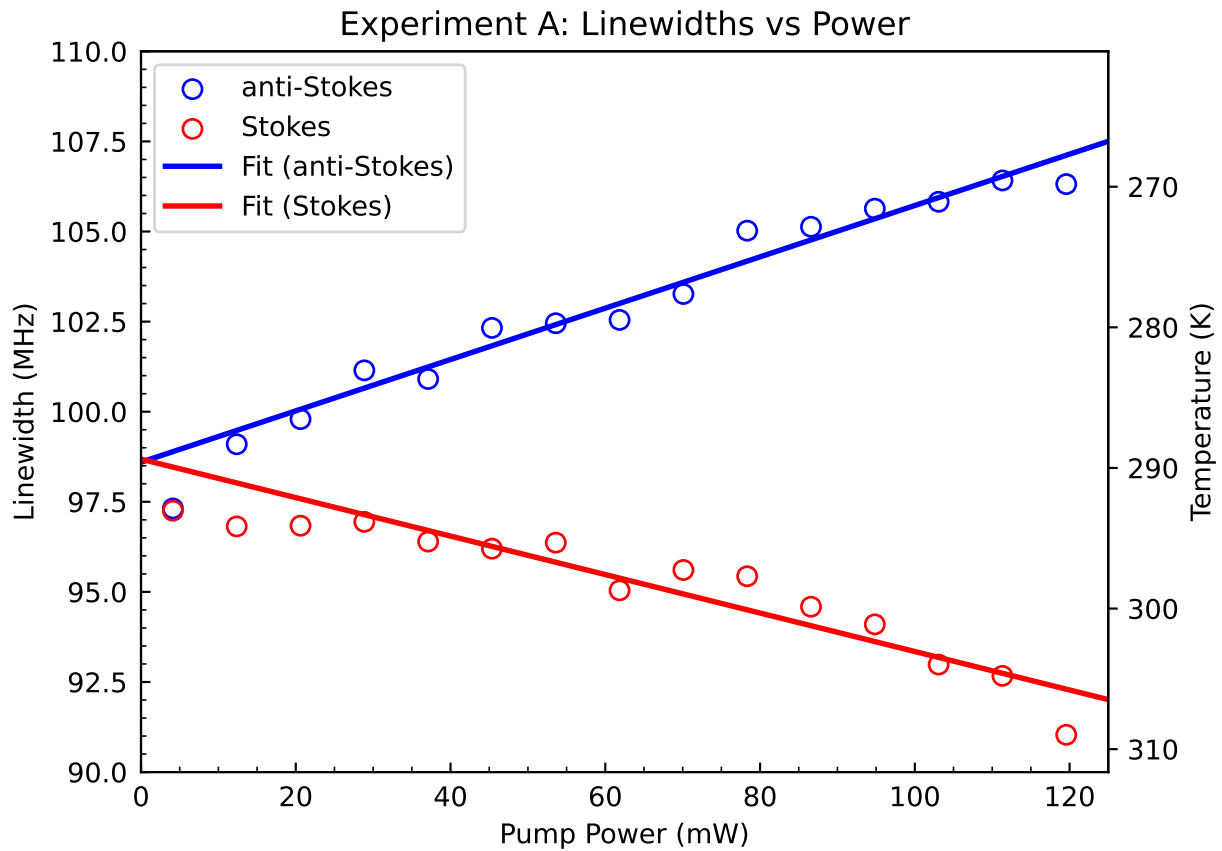


Figure 2.8: .

slopes in the anti-Stokes linewidth data and explains the otherwise surprising discrepancy in inferred Brillouin gain compared to values published in the literature for identical CS_2 -filled LCOFs.

2.5 Discussion

2.5.1 Standardized Cooling Metric

2.5.2 Alternative Platforms

Tapered chalcogenide Photonic Crystal Fiber: Max Plank Results (corroborate our results)

2.5.3 Pathways to Net Cooling

Ideas to achieve net cooling, one might design a system where:

- 1) single pass gain bias swing energy transfer bias to favor anti-Stokes over Stokes (mode-dependent

Experiment A: Simulated Gain Spectrum Predicts Lineshape

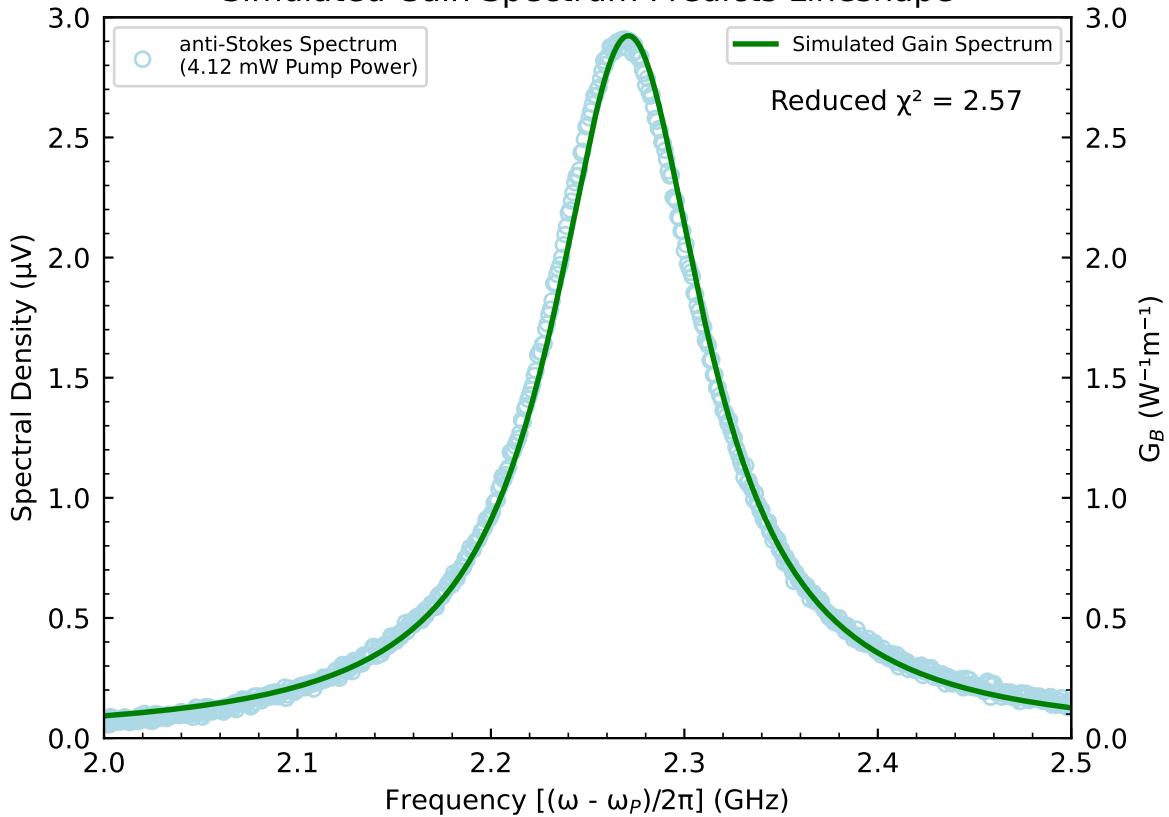


Figure 2.9:

gain) the Stokes process were not permitted (ryan's only idea), or just significantly restricted - what is that bias threshold requirement? currently, we are net *heating* the system because it is easier to heat from equilibrium than cool (right? explore this. it's also hard to make it hotter beyond a certain point.) implementation ideas: multi-pump scheme to destructively interfere with Stokes and/or constructively interfere with anti-Stokes doping or specialized waveguide gratings that pick out the Stokes band for out-of-plane scattering

2) time bias create an energy transfer *rate* bias between Stokes and anti-Stokes can be accomplished with either the brillouin energy transfer rate or the repopulation rate

brillouin process rate: $4vg/L$, have either group velocity or length be different for Stokes vs anti-Stokes (smaller vg or larger L for Stokes than anti-Stokes) make anti-Stokes fast light and/or Stokes slow light vg inversely proportional to pump power, so it's a balance increasing pump power = slower escape time ($4vgL$), and also larger dissipation (Gamma+)

repopulation rate: thermally insulate the anti-Stokes mode from the thermal bath that would repopulate

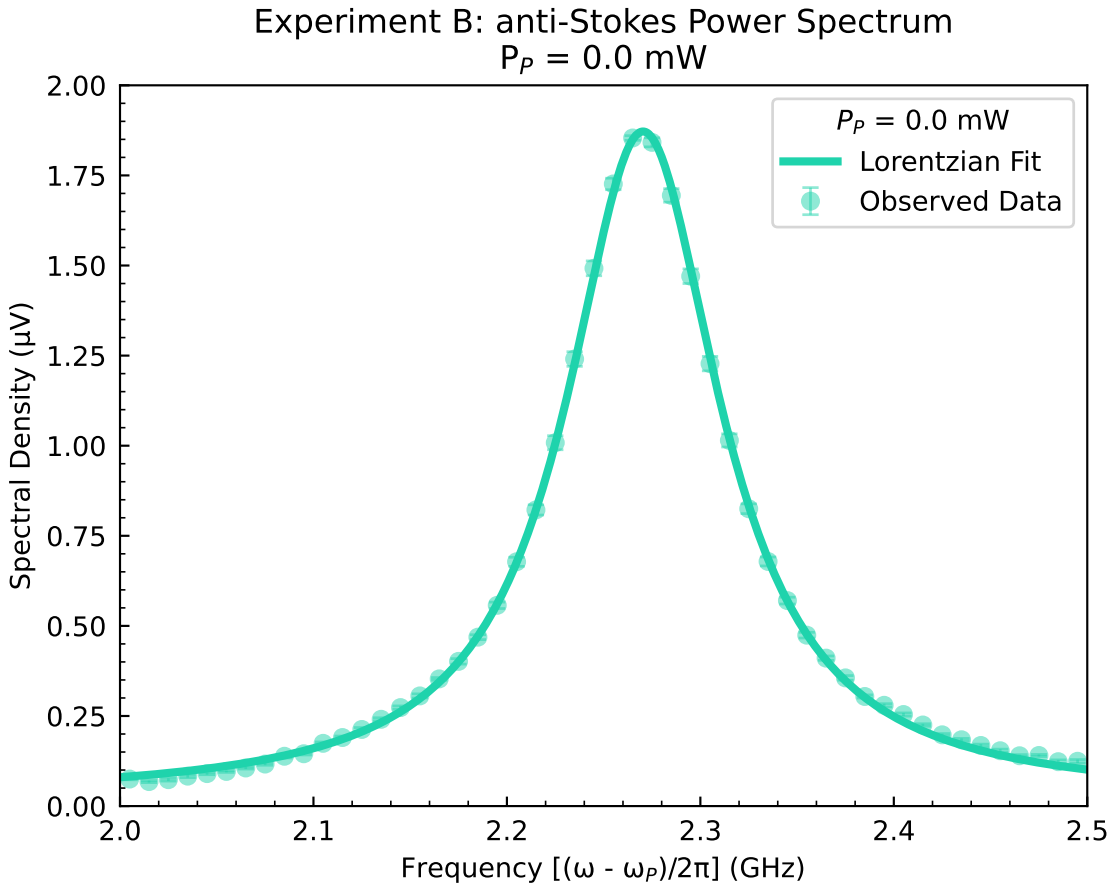


Figure 2.10: .

it or at least insulate it some amount more than Stokes (what is that threshold? even if it's only net cooled for picoseconds, what is that minimum crossover point insulation bias point) essentially locks in the cooled mode while letting the heated mode spill out implementation idea: design a fiber/waveguide with acoustic directional bias, such that phonons travelling one direction dissipate quicker because of the geometry/acoustic properties of the fiber. (triangles? acting as tapered acoustic dissipators, pointing in one direction?)

3) starting temperature Could you achieve net cooling in a cheap and dirty sense by starting the system in a very heated state, thus invoking a natural dissipation rate bias?! - yes! Things do naturally run hot, perhaps no extra fancy engineering is needed for some practical systems? (data processing, reduce thermal noise from above ambient heat) not traditional definition of optical refrigeration below ambient/thermal bath, but still *useful* is this already done? lit search

Think about a practical device or system for each of these cases (think waveguide playground!)

2.5.4 Applications to Ground State Cooling

Experiment B: anti-Stokes Power Spectrum
 $P_P = 22.7 \text{ mW}$

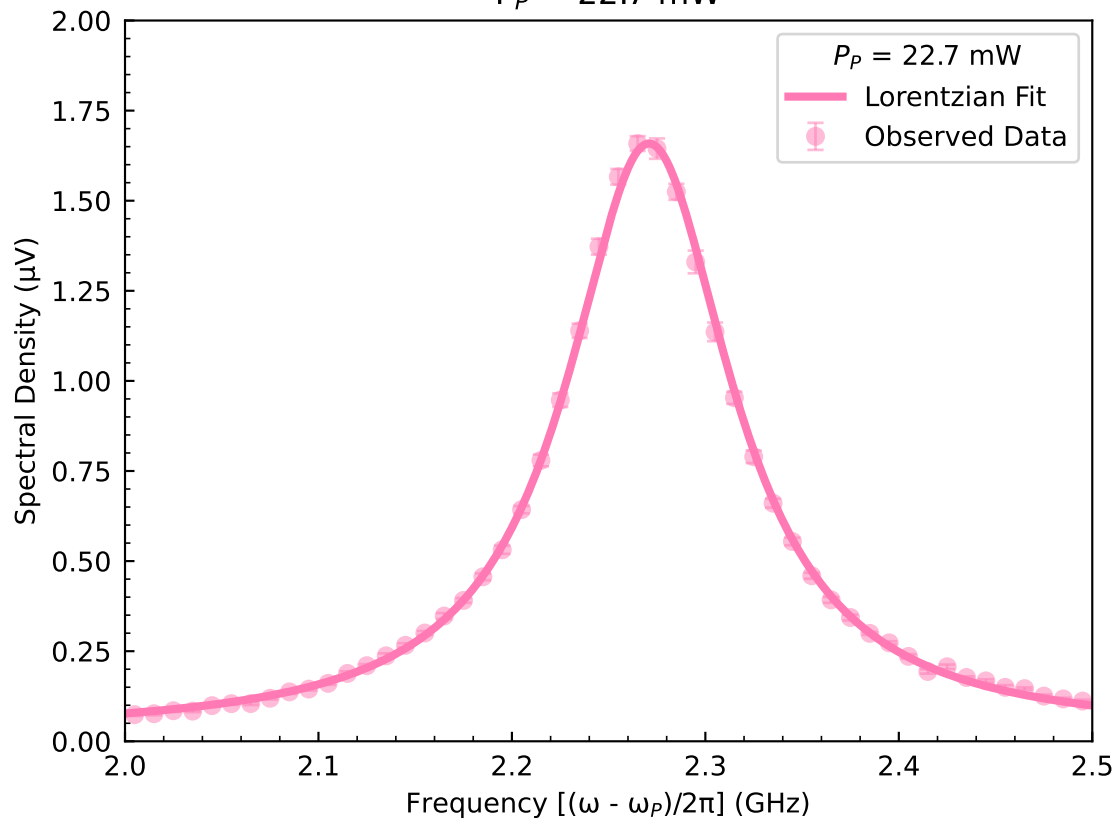


Figure 2.11: .

Experiment B: anti-Stokes Power Spectrum
 $P_P = 45.4 \text{ mW}$

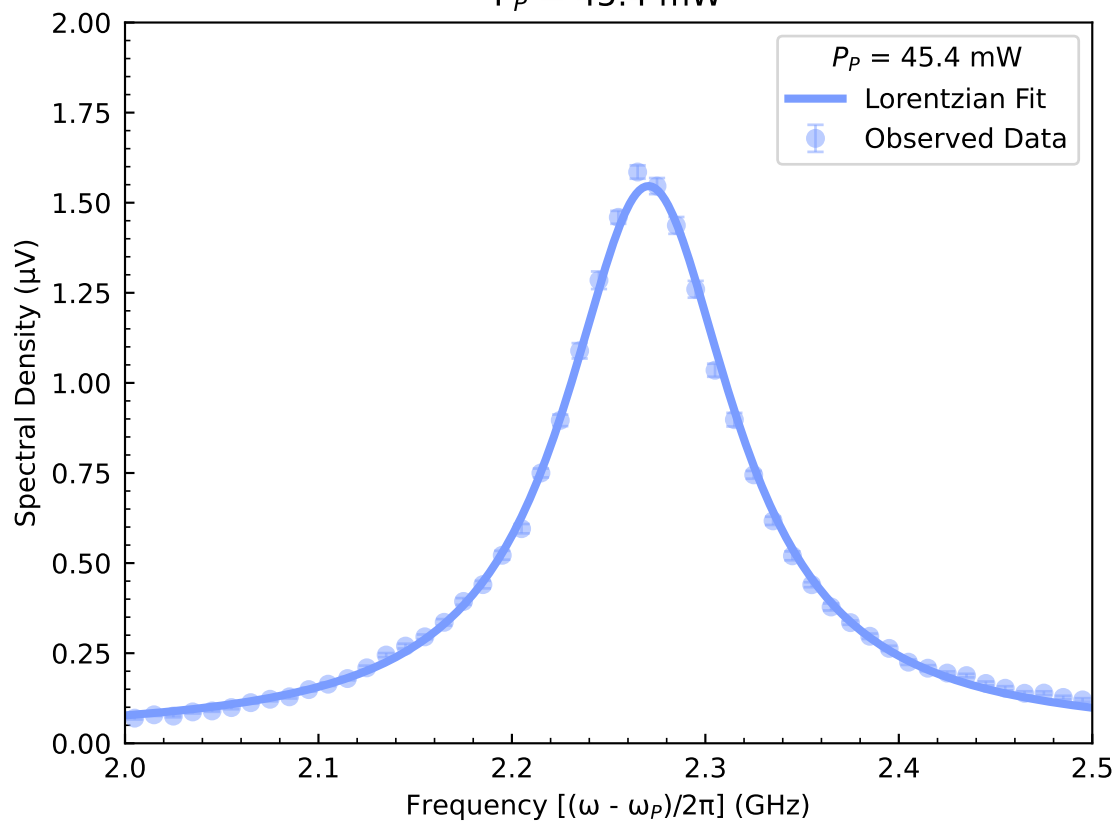


Figure 2.12: .

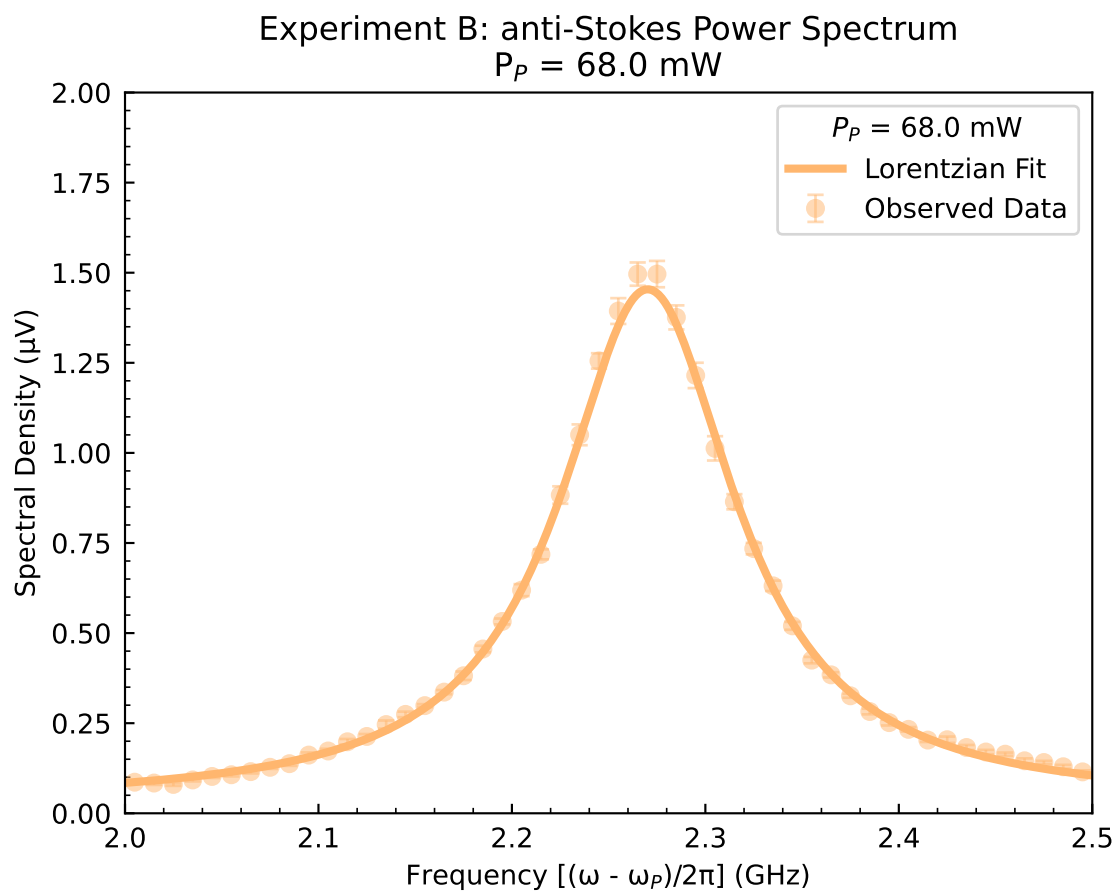


Figure 2.13: .

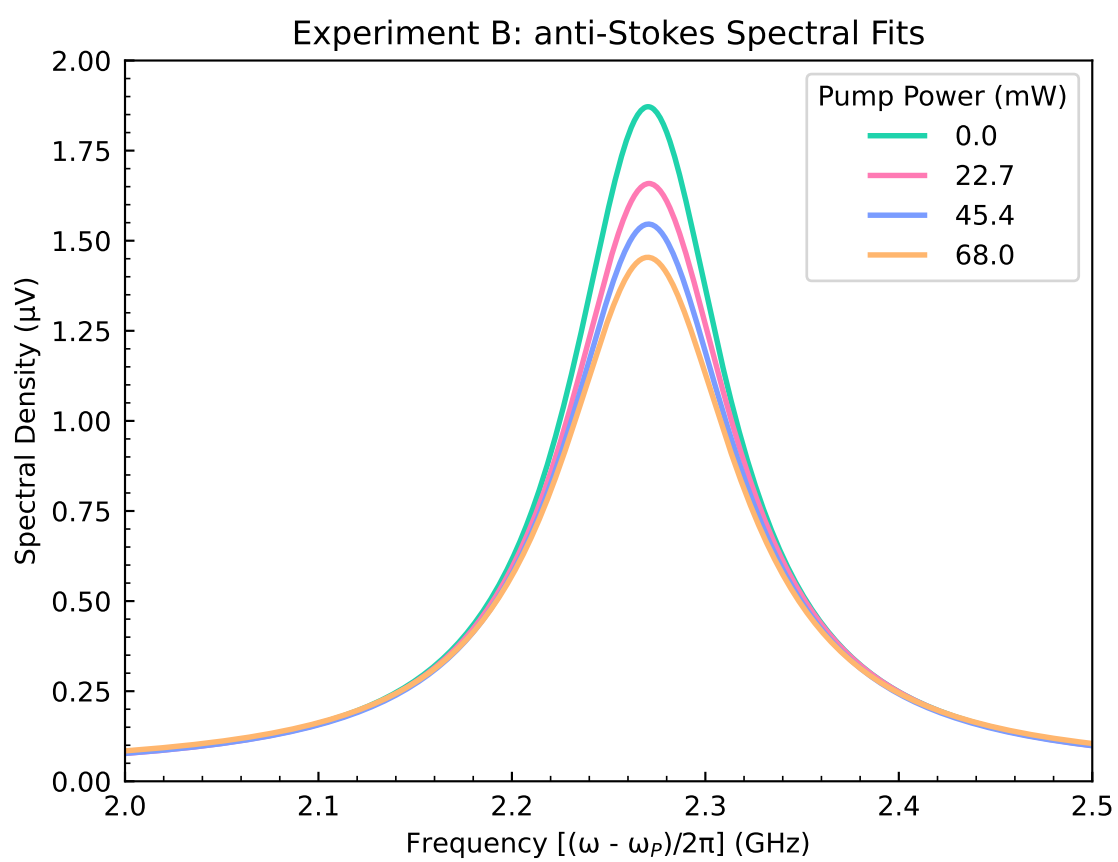


Figure 2.14: .

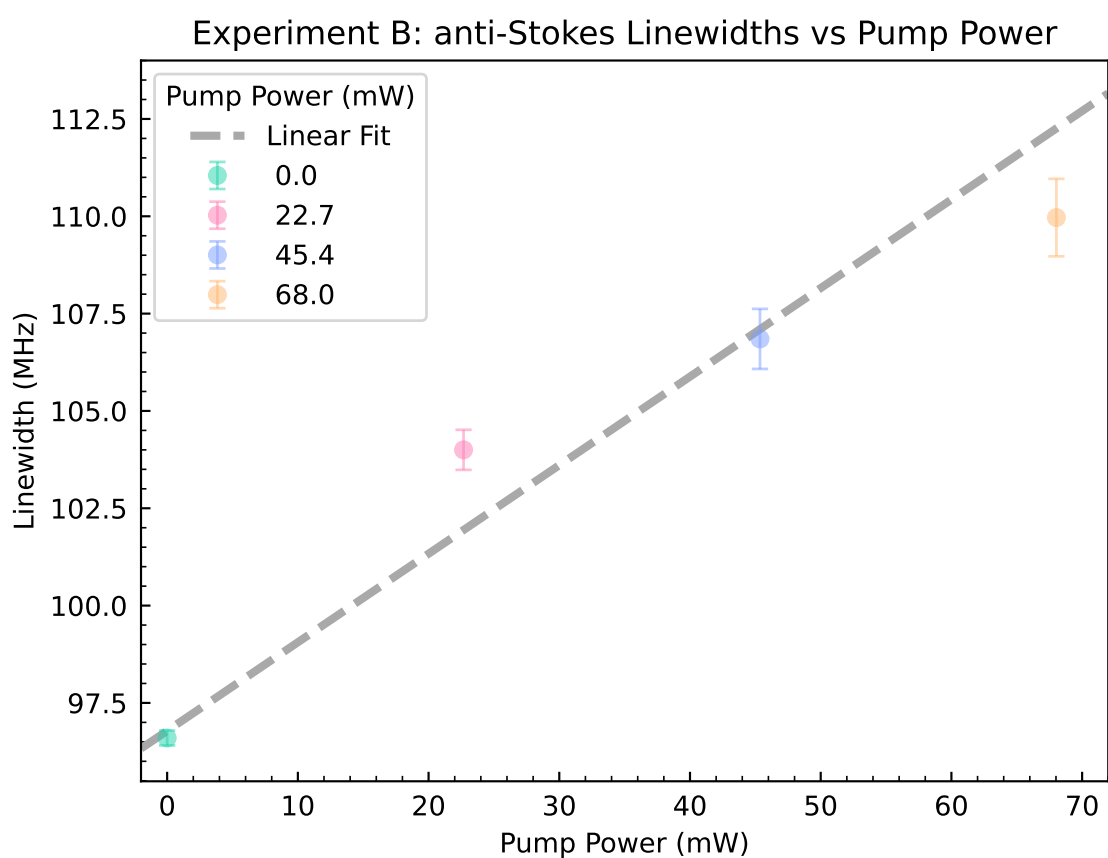


Figure 2.15: .

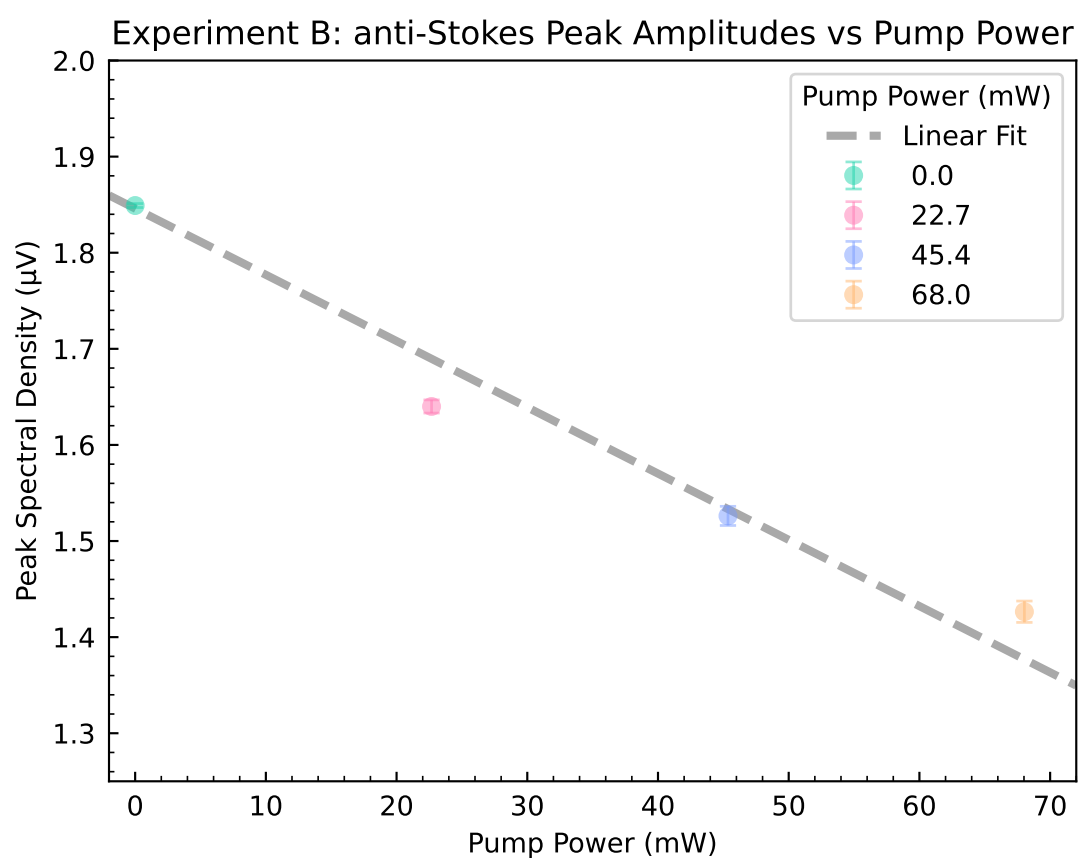


Figure 2.16: .

Chapter 3

A Coherently Stimulated Phonon Spectrometer

This chapter presents a preview of an article in-prep for publication. Neither the author nor the publisher are responsible for any errors or omissions in any future publication derived from this version of the manuscript.

3.1 Abstract

We present a novel coherently stimulated Brillouin spectrometer utilizing a detuned pump-probe design that exploits a relaxation of phase-matching requirements at small lengths, enabling room-temperature traveling-wave phonon spectroscopy at the micrometer scale with sub-10 fW sensitivity. This approach overcomes the limitations of traditional stimulated Brillouin techniques, particularly regarding phase-matching constraints and spatial resolution. We validated my instrument's sensitivity with 1 cm of Ultra High Numerical Aperture 3 (UHNA3) fiber and 100 μm of bulk carbon disulfide liquid, demonstrating its capability to measure Brillouin scattering in materials with low Brillouin gain or, with particular advantage, small effective lengths. This advancement opens new possibilities for nanometer-scale Brillouin spectroscopy and the development of nano-acousto-optic devices.

3.2 Introduction

Brillouin scattering, the inelastic interaction between light and acoustic phonons, is a fundamental phenomenon for probing the mechanical and structural properties of materials at microscopic scales. In spontaneous Brillouin scattering, thermally excited acoustic phonons scatter incident light, causing frequency shifts that reveal information about the material's elastic properties and acoustic modes¹. However, the weak signal inherent to spontaneous Brillouin scattering often demands long acquisition times and limits spatial resolution, posing challenges for high-resolution material characterization.

Stimulated Brillouin Scattering (SBS) uses intense optical fields to amplify the acoustic wave through a

nonlinear optical process⁸. In SBS, a strong pump laser interacts with a counter-propagating Stokes wave in the medium, generating acoustic phonons via electrostriction. As the phonon population grows, it further amplifies the Stokes wave. In turn, that amplified Stokes wave interferes with the pump and reinforces the acoustic field, creating a positive feedback loop that drives exponential amplification. This mechanism enables more efficient excitation and detection of acoustic phonons and underpins numerous applications in optical signal processing, sensing, and high-resolution spectroscopy including mechanobiology^{9–18}.

However, conventional SBS techniques struggle with short samples or materials of inherently low Brillouin gain and strict phase matching requirements continue to pose a challenge.^{19–21} Because the Stokes amplitude depends on the product of the Brillouin gain coefficient, pump power, and interaction length, small volumes often yield weak signals unless extremely high optical powers are used. Moreover, while backward SBS sends the scattered wave in the opposite direction of the pump, parasitic reflections and pump leakage can still obscure the Stokes signal, demanding careful optical isolation and sometimes elaborate filtering. These constraints make it difficult to measure thin films and micro- and nanoscale devices, particularly if high optical intensities risk damaging sensitive samples. As a result, standard SBS approaches are not easily adapted to sub-centimeter lengths or low-gain media, prompting the need for new methods that maintain high sensitivity in short interaction regions.

To overcome these challenges, researchers have explored various approaches^{22–27}. Techniques based on optical cavities increase the effective interaction length, but require precise alignment and are sensitive to environmental fluctuations²⁸. Forward Brillouin scattering methods, such as those demonstrated by Kittlaus et al.²⁹, offer relaxed phase-matching conditions but introduce increased modal complexity. Meanwhile, coherent probe beam amplification can boost sensitivity, yet it can introduce additional noise and complexity because phase noise in laser sources can cause significant gain fluctuations³⁰.

Here, we demonstrate a detuned pump–probe design that relaxes the usual phase-matching constraints at short lengths. This approach offers a new route to measure traveling-wave phonons in sub-centimeter or even micrometer-scale samples at room temperature with unprecedented sensitivity. We demonstrate the capabilities of my instrument by measuring Brillouin scattering in 1 cm of UHNA3 fiber and 100 μm of bulk carbon disulfide (CS₂) liquid. These measurements highlight the instrument’s ability to characterize materials with low Brillouin gain or small effective lengths.

The development of this coherently stimulated Brillouin spectrometer opens new avenues for nanometer-scale Brillouin spectroscopy and advances the characterization and design of nano-acousto-optic devices. It holds promise for pushing research in material science, photonics, and sensing technologies toward higher spatial resolution and sensitivity, marking a significant step toward practical, room-temperature Brillouin-based spectroscopy and sensing solutions.

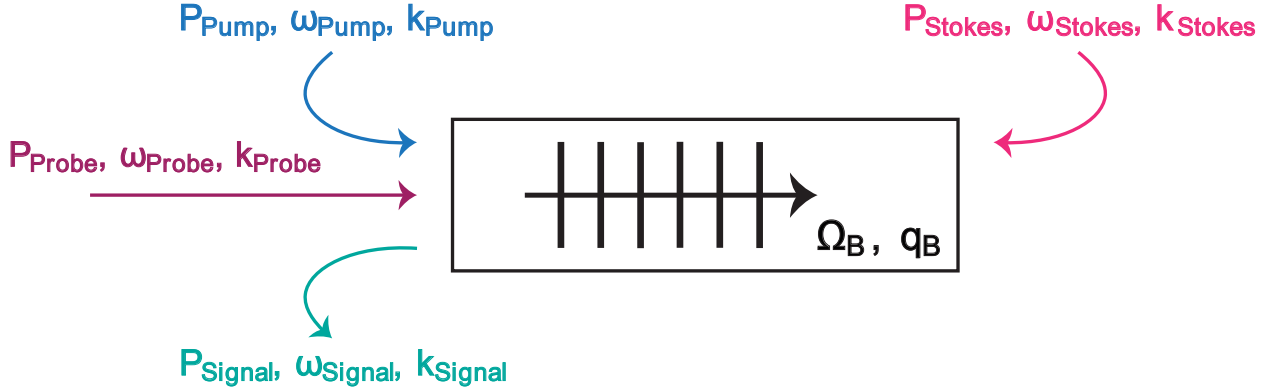


Figure 3.1: Illustration of 4-Wave Brillouin Scattering.

3.3 Theoretical Framework

3.3.1 Coherently Stimulated Four-Wave Brillouin Scattering

Traditional SBS, illustrated by the schematic in Figure 3.1(a) for the Stokes process, is a three-wave mixing process in which incident pump laser light of frequency ω_{Pump} inelastically scatters from a traveling-wave phonon of frequency Ω to produce light that is frequency-shifted by the phonon frequency. In the Stokes process the phonon is retreating from the incident laser light and the scattered light is shifted down in frequency ($\omega_{\text{Stokes}} = \omega_{\text{Pump}} - \Omega$). Spatial overlap of the backscattered light with the incident laser light allows for interference of the two optical fields to produce a frequency at the difference of the two ($\omega_{\text{Pump}} - \omega_{\text{Stokes}}$). Since this difference frequency is exactly equal to the frequency of the acoustic field Ω , the beating of the incident pump light with the backscattered Stokes light produces an electrostrictive reinforcement of the acoustic wave. This driving of the acoustic wave in turn increases the scattering rate of the incident pump light, producing a positive feedback process and an exponential increase of the amplitude of the backscattered Stokes wave.

Figure 3.1(b) illustrates coherently stimulated four-wave Brillouin scattering for the Stokes process. We introduce a strong, controlled external Stokes wave of frequency ω_{Stokes} that drives electrostrictive reinforcement of the acoustic field in the medium. The backscattered Stokes light is normally collected in an SBS process, but the external Stokes laser overwhelms it. To resolve this, we inject light of a distinct frequency ω_{Probe} from an additional external laser which copropagates with the Pump and backscatters in the medium from the strongly driven acoustic field. This produces backscattered Signal light to be collected

$(\omega_{\text{Signal}} = \omega_{\text{Probe}} - \Omega)$ which is spectrally distinct from the high-powered Stokes laser light.

To describe this interaction and characterize the performance of the instrument, we derive the coupled-wave equations for the four-wave mixing process in Appendix B.1. These equations describe the relationship between the optical fields and the acoustic field in the material and result in the following expression for the scattered power of the backscattered signal,

$$P_{\text{Sig}} = \frac{1}{4}(G_B L)^2 P_P P_S P_{Pr} \text{sinc}^2 \left(\frac{\Delta k L}{2} \right), \quad (3.1)$$

where P_P , P_S , and P_{Pr} are the powers of the pump, Stokes, and probe lasers, respectively. G_B is the effective Brillouin gain, given by

$$G_B = \frac{g_0}{A_{eff}} \frac{\left(\frac{\Gamma_B}{2}\right)^2}{(\Omega - \Omega_B)^2 + \left(\frac{\Gamma_B}{2}\right)^2}, \quad (3.2)$$

with the on-resonance gain factor of the material given by

$$g_0 = \frac{\gamma_e^2 \omega^2}{n v c^3 \rho_0 \Gamma_B}. \quad (3.3)$$

Here, γ_e is the electrostrictive constant, ω is the pump frequency, n is the refractive index of the material, v is the sound speed of the material, c is the speed of light, ρ_0 is the mean density of the material, and Γ_B is the Brillouin linewidth, or phonon dissipation rate, of the material. In Equation 3.2, Ω_B is the resonant Brillouin frequency of the material, A_{eff} is the effective area of the material, Δk is the wavevector mismatch between the optical fields, to be discussed next, and L is the effective length of the material.

3.3.2 Phase Matching Relaxation

In all nonlinear optical processes, efficiency is maximized when phase matching conditions are satisfied. A frequency mismatch (energy unconservation) or a wavevector mismatch (momentum unconservation) each result in drastically reduced efficiency of a given process.³¹ This can be seen by Equation 3.1, where the wavevector mismatch, Δk , is contained within a sinc^2 function. This sinc^2 term thereby defines the phase matching bandwidth of the system, notably scaling with effective interaction length L .

We apply this wavevector mismatch allowance to the pump and probe waves ($\Delta k = k_{\text{Pump}} - k_{\text{Probe}}$) so that the backscattered signal is different than the applied Stokes wave. This choice allows for selection of

the signal and rejection of the Stokes with a bandpass filter. Expressed in terms of wavelengths, this gives

$$\Delta k = \frac{4\pi n \Delta \lambda}{\lambda_{Pump} \lambda_{Probe}} \approx \frac{4\pi n \Delta \lambda}{\lambda_{Pump}^2}. \quad (3.4)$$

We can apply this to the phasematching bandwidth term to find the fraction of maximum scattered power, Φ , that can be expected for a given interaction length, L , and phase mismatch $\Delta\lambda$ between the pump and probe,

$$\Phi \equiv \text{sinc}^2 \left(\frac{2\pi n \Delta \lambda L}{\lambda_{Pump}^2} \right). \quad (3.5)$$

Using this expression for Φ , we see that for an effective length of 1 m, a wavelength mismatch of only 0.6 pm from a typical wavelength of 1.55 μm pump light in UHNA3 fiber drops the scattered power to half of the maximum. However, for shorter effective lengths the wavevector mismatch becomes more forgiving; a 36 pm mismatch preserves 82.5% of the maximum signal for a length of 1 cm under identical conditions. This separation translates to about 4.5 GHz, providing enough spectral separation for the backscattered signal to be isolated from the applied Stokes light.

Furthermore, for decreasing lengths, Equation 3.5 predicts an increase in the fraction of maximum signal produced, given equivalent pump–probe detuning, as the sinc^2 function is sampled closer to its peak center. Alternatively, as length decreases, the probe may be further detuned from the pump and still achieve the same fraction of the maximum signal as for longer lengths, perhaps offering a slight advantage in noise reduction. It should be noted that the scattered power, as given by Equation 3.1, scales with the square of the effective length. Thus, while smaller lengths allow for the ability to capture a larger fraction of this maximum scattered power, the actual amount of scattered power decreases dramatically as length decreases.

3.4 Methods

3.4.1 Instrument Design

Figure 3.2 shows the instrument’s design. A pump and Stokes wave is synthesized from a single tunable laser source for coherent stimulation of a sample. The pump wave (ω_{Pump}) is amplified by an EDFA and passed through a VOA for power control. The output is then polarization-controlled to reflect at a PBS for injection into the sample. For Stokes synthesis, an AC signal (Ω) is supplied to an IM with carrier frequency nulled and a tunable filter is used to select the lower-frequency Stokes side band ($\omega_{Pump} - \Omega$). This Stokes light is then amplified by an EDFA, passed through a VOA, and polarization-controlled to reflect at a second

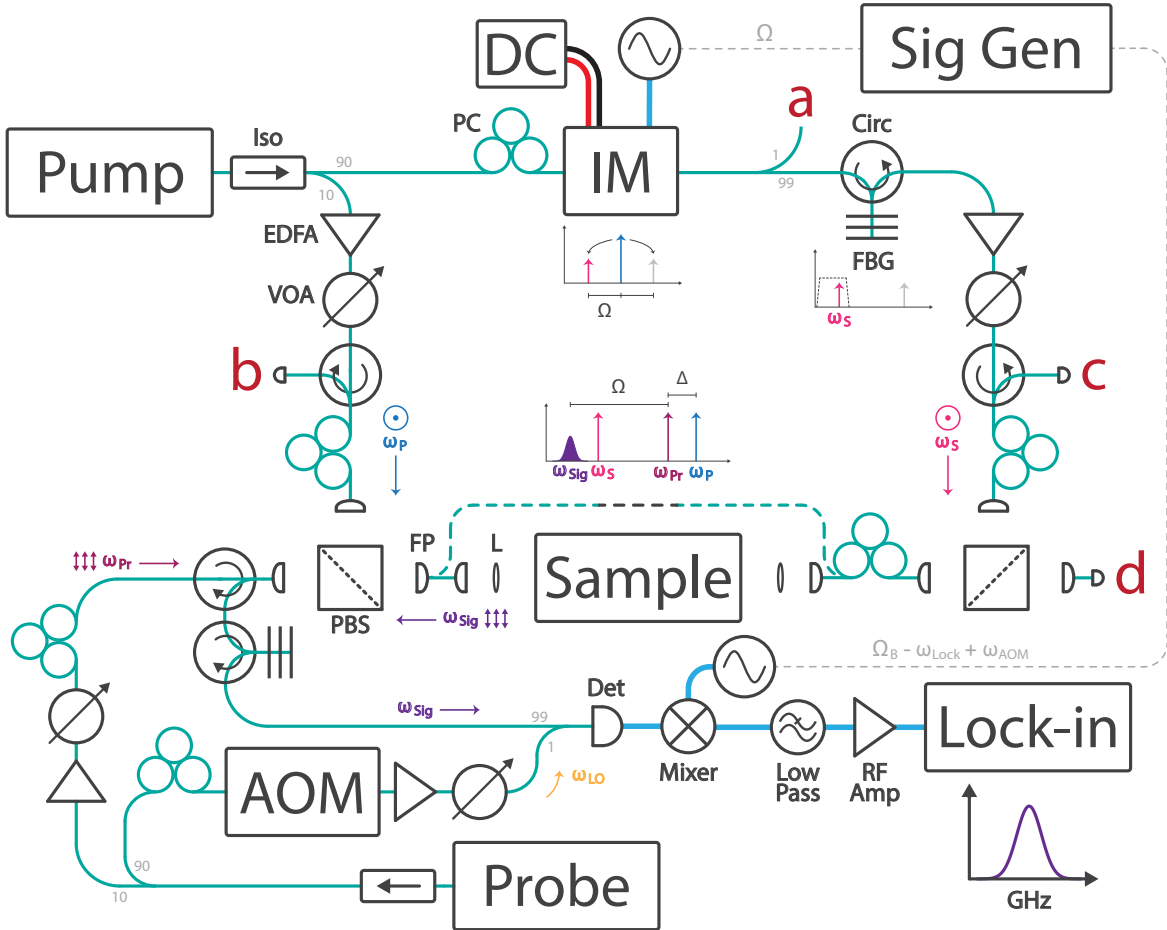


Figure 3.2: Design schematic of a coherently stimulated phonon spectrometer. A tunable Continuous Wave (CW) laser at approximately $1.55\text{ }\mu\text{m}$ emits light that passes through an isolator (Iso) and a splitter, diverting 10% to a 27 dBm Erbium-Doped Fiber Amplifier (EDFA) followed by a Variable Optical Attenuator (VOA). This pump light (ω_P) is polarization-controlled to reflect off a polarizing beam splitter (PBS) and is recoupled to fiber via a fiber port (FP), then directed to the sample either by direct fiber coupling or through a pair of FPs and lenses (L) for free-space samples. After passing through the sample, the pump light traverses a corrective polarization controller that mitigates fiber twists and bends before reflecting off a second PBS, where it is routed to port (c) for power monitoring. To synthesize the Stokes wave, a 90% split from the original pump is processed through a fiber-optic intensity modulator (IM) and a fiber Bragg grating (FBG), generating a Stokes sideband downshifted from the pump by Ω . This frequency shift is swept via a signal generator to capture Ω_B . A 99/1 splitter provides a tap at port (a) to optimize Stokes synthesis. The Stokes wave (ω_S), amplified by a 1 W EDFA and VOA-controlled, counter-propagates along the pump path and is monitored at port (b). A second tunable CW laser, detuned from the pump, generates the probe wave (ω_{Pr}), which is amplified by a 1 W EDFA, attenuated variably, and polarization-controlled to pass through the initial PBS where it is incident on the sample. Backscattered signal light (ω_{Sig}) transmits back through the PBS, while unscattered probe light transmits to a power meter at port (d). A circulator parts the signal from the probe path, with an FBG filtering out any unwanted noise or Stokes light. Finally, the signal is heterodyned with an EDFA-amplified, acousto-optic modulator (AOM)-shifted local oscillator (LO) derived from the probe laser and directed to a photodiode for detection. The resulting radio frequency (RF) signal is mixed with an alternating current (AC) LO supplied by the signal generator which sweeps synchronously with the Stokes synthesis frequency, and collected by a lock-in amplifier for data processing.

PBS for counter-propagation to the pump through the sample.

A separate tunable laser is used to supply a probe wave ($\omega_{\text{Probe}} = \omega_{\text{Pump}} + \Delta k$) and LO. Probe light is amplified by an EDFA and passed through a VOA and a polarization controller aligns the polarization for transmission through the first PBS whereby it copropagates with the pump through the sample. Backscattered light exits the sample and transmits back through the first PBS, whereas the orthogonally polarized Stokes light reflects at this same point to be diverted to a tap for power monitoring. The backscattered signal ($\omega_{\text{Signal}} = \omega_{\text{Probe}} - \Omega$) then routes through two subsequent circulators for spectral filtering by a 5 GHz bandpass tunable filter. This filter allows the desired backscattered signal to pass while rejecting any reflected probe light as well as any reflected, transmitted, or backscattered light from the pump or Stokes waves that was not already diverted by the PBS.

The filtered signal then heterodynes via a 99-1 splitter with the LO which is frequency-upshifted by an AOM ($\omega_{\text{LO}} = \omega_{\text{Probe}} + \omega_{\text{AOM}}$) and controlled to be copolarized with the signal. Of the resulting frequencies from the heterodyne process, only the difference frequency term is considered, as all others are beyond the range of detection. This heterodyned signal ($\omega_{\text{Signal}} = \Omega + \omega_{\text{AOM}}$) is then captured by a photodiode detector and heterodyned again by a RF mixer with a second AC signal ($\Omega + \omega_{\text{AOM}} - \omega_{\text{Lock}}$), where ω_{Lock} is a fixed-frequency to be detected by a lock-in amplifier set to this frequency after being passed through a low-pass filter and amplified by an RF amplifier. Synchronous sweeping of both AC signals, each involving Ω , allows for ω_{Lock} to remain fixed throughout measurement over a frequency range.

3.4.2 Experimental Techniques

We optimized the signal-to-noise ratio (SNR) of my instrument through specific design choices and device settings. my setup simultaneously generates pump, Stokes, and probe optical fields for coherently stimulated Brillouin scattering. The pump laser provides ~ 45 mW total output, of which 10% is split and amplified to ~ 0.5 W for the pump field; the remaining 90% is frequency-shifted and amplified to ~ 1 W for the Stokes field. Likewise, the probe laser also outputs ~ 45 mW, with 10% amplified to ~ 1 W for the probe field and the remaining 90% reserved for the LO. To combine the backscattered signal and LO with minimal loss, weuse a 99/1 splitter instead of a typical 50/50, preserving 99% of the signal. The LO is therefore amplified to ~ 230 mW so the total optical power at the detector remains below the 2.4 mW damage threshold. After detection, the electronic signal is mixed with a 17 dBm AC reference and further amplified by 23 dBm before input to the lock-in amplifier. We find that running both the pump and probe lasers in “whisper” mode (as opposed to “dither”) significantly enhances the measured SNR.

We use a Zurich Instruments HF2LI 50 MHz lock-in amplifier whose demodulator settings are carefully

tuned to maximize SNR. A 10 MHz reference clock from the signal generator is fed into the lock-in to synchronize timing. The input-signal range, which sets the analog input amplifier’s gain, should exceed the measured signal (including any direct current (DC) offset) by at least a factor of two. This is best achieved by using the lock-in software’s auto feature, which continuously adjusts the range over a rolling 100 ms window. We set the input coupling to AC, insert a high-pass filter to remove DC components, and choose $1\text{ M}\Omega$ input impedance. For noise suppression, we also engage the lock-in’s eighth-order low-pass filter (roll-off 48 dB Oct^{-1}) and sample the data at 1.84 MSa s^{-1} , the maximum rate available.

Further SNR improvements are gained by narrowing the lock-in’s low-pass filter bandwidth to match both the sub-Hz natural linewidth of the heterodyne signal and the thermally-driven frequency drift of the apparatus. After a ~ 30 min warm-up, we observe less than 100 Hz of drift in the detected signal frequency, so we typically set a 100 Hz low-pass bandwidth for multi-hour measurements. For shorter scans (< 15 min), we can reduce this bandwidth to 40 Hz if needed. In addition to linewidth variability, the signal’s center frequency can shift due to thermal changes in the AOM and related electronics. Although Ω is nominally controlled to sub-hertz precision by the signal generator, our AOM’s shift ω_{AOM} drifts from 40 MHz up to $\sim 40.000\,82$ MHz over roughly 30 min. Once at thermal equilibrium, the AOM remains stable within ± 50 Hz, enabling a reliable lock-in frequency reference and minimal filter bandwidth. This stability is crucial for repeatable, high-resolution Brillouin measurements.

3.5 Results

3.5.1 Instrument Sensitivity

1 cm UHNA3 CABS

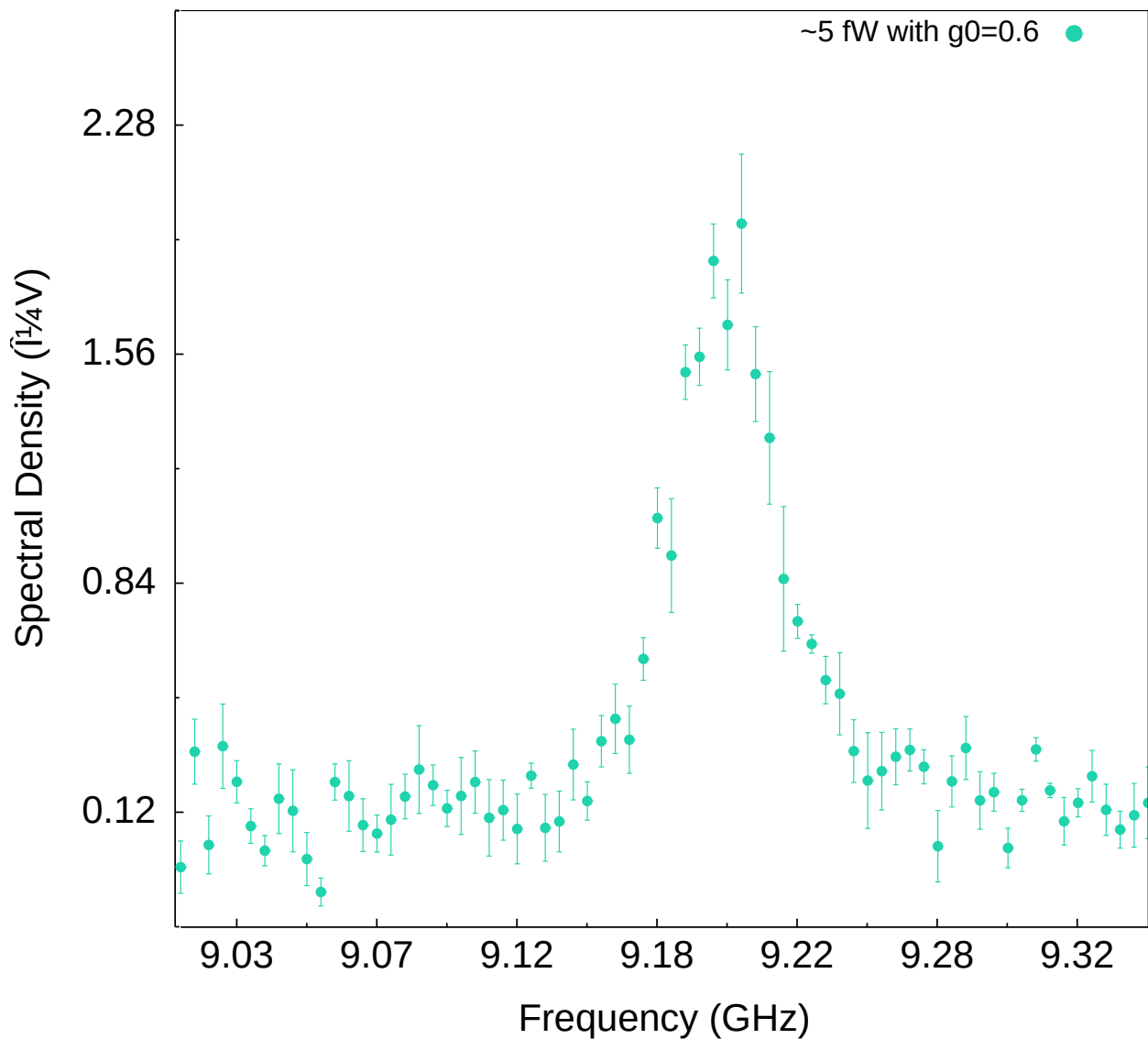


Figure 3.3: $\sim 5 \text{ fW}$ sensitivity measurement

We begin by testing the sensitivity of the instrument as a way of defining a performance metric for the instrument which can be used to indicate what material, power, and length combinations might be possible to measure. From Equation 3.1, the sensitivity of the instrument is the minimum scattered power, P_{Sig} , to produce a statistically significant measurement. To determine this, we target a specific length, L , of a sample of known effective Brillouin gain, G_B . We keep the pump-probe detuning, $\Delta\lambda$, constant across measurements and record the pump, Stokes, and probe optical powers to calculate the scattered power. Starting with sufficient optical powers to produce a clearly distinguishable measurement, we gradually reduce the optical powers until the sensitivity floor is reached.

To serve as our sensitivity testbed, we prepared 1 cm of Nufern's UHNA3 fiber, a well-studied fiber with known effective Brillouin gain³². Additionally, UHNA3 fiber offers several properties that make it ideal for this task of unambiguous detection of the Brillouin signal as it diminishes with each subsequent reduction in optical powers. First, it offers a Brillouin shift that is spectrally far from that of the single mode fiber (SMF-28) which constitutes much of the instrument. This ensures that the Brillouin response of the sample is not conflated with the Brillouin response of the instrument itself. Additionally, the core of UHNA3 fiber features a high concentration of germanium which improves the optical and acoustic guidance in the fiber as a result of the large refractive index difference between core and cladding. Finally, UHNA3 fiber offers a high optomechanical nonlinear response, with an effective Brillouin gain of $0.6 \text{ W}^{-1} \text{ m}^{-1}$ measured at room temperature³². This gain factor is larger than that of SMF-28 by an order of magnitude³³.

Figure 3.3 presents a measurement in which the instrument's sensitivity reaches $P_{Sig} = 5 \text{ fW}$. Each trace is the average of five consecutive scans, and an average of five background scans has been subtracted to isolate the signal. Error bars represent the standard error (1σ of the mean). By comparing the peak amplitude at resonance to the off-resonance baseline, we estimate an SNR greater than 5. Under a normal-noise assumption, an SNR of 5 corresponds to a 5σ significance level (99.7% confidence). Achieving this 5 fW threshold demonstrates the feasibility of measuring weaker signals in materials with lower Brillouin gain or smaller effective lengths.

G_B ($\text{W}^{-1} \text{ m}^{-1}$)	L (m)	P_P (μW)	P_S (μW)	P_{Pr} (μW)	$\Delta\lambda$ (pm)
0.6	0.01	506	504	2.01	20

Table 3.1: Measurement parameters for sensitivity measurement and calculation.

3.5.2 Measurements

We demonstrate the capabilities of the instrument on two common sample classes: fiber and bulk material. For a fiber sample we again choose UHNA3 for its higher nonlinear response and excellent optical

and acoustic guidance. In contrast to the sensitivity measurements, we now seek to demonstrate the full measuring capabilities of the instrument and so apply all available optical power (~ 1.5 W) to maximize the backscattered signal from the sample. We target the same 1 cm segment of UHNA3 fiber as was used for determining sensitivity.

1 cm UHNA3 CABS

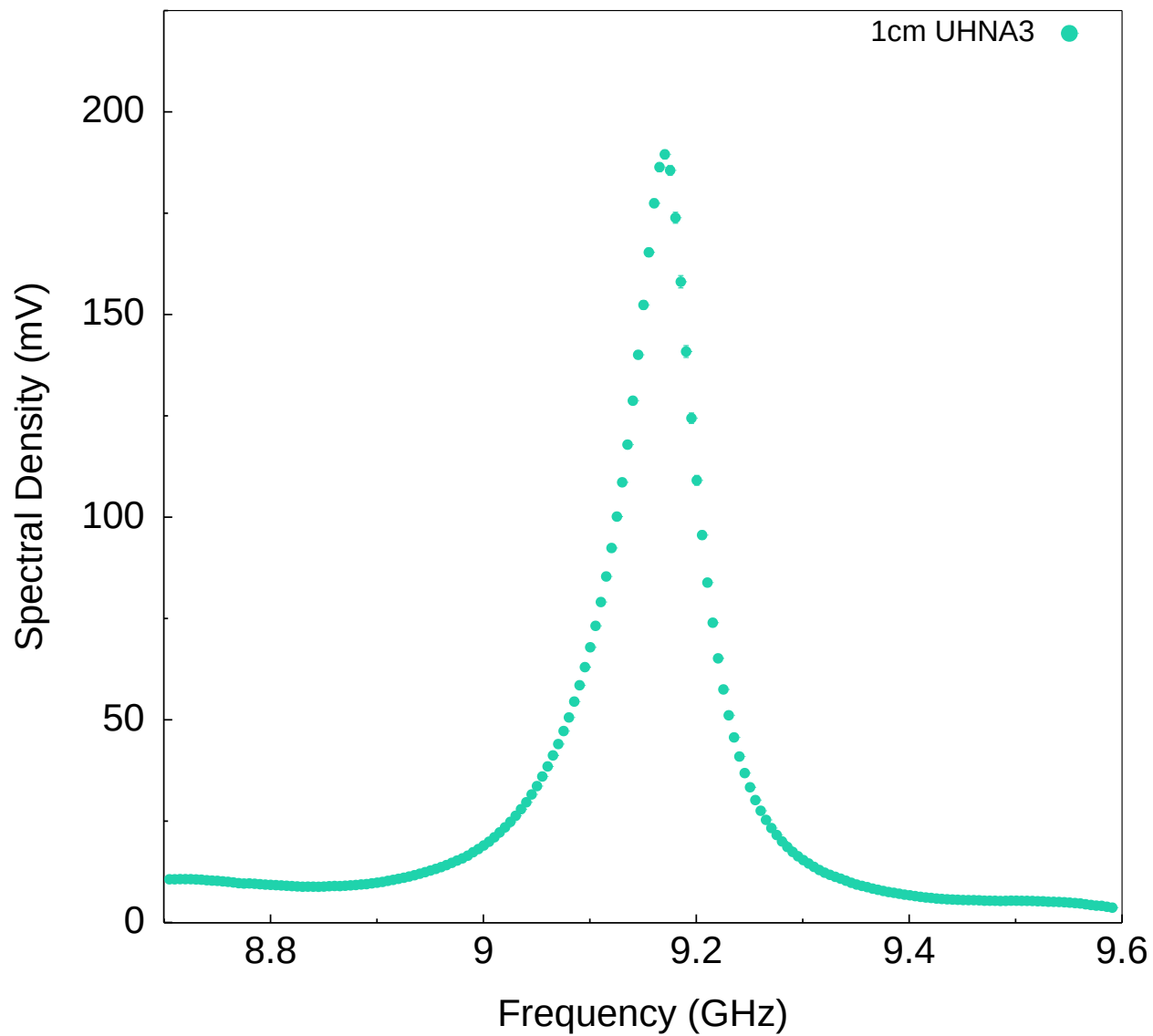


Figure 3.4: 1 cm UHNA3

Figure 3.4 shows the spectral profile captured for 1 cm of UHNA3 fiber, revealing the expected lorentzian profile consistent with Equation 3.2. The peak amplitude of the spectra occurs at 9.1704 GHz, indicating the Brillouin resonance frequency of the longitudinal traveling-wave mode in the fiber. The FWHM of the measurement is 80 MHz and provides a measure of the phonon dissipation rate. Both values match what is seen in the literature for SBS measurements of UHNA3 fiber.³² The data shown are a background-subtracted average of five successive measurements taken over ten minutes with error bars corresponding to 1σ of the mean.

To achieve this measurement of UHNA3 fiber, the instrument design was altered to include only fiber-coupled segments connecting the fiber ports between the two PBSs. We set the pump laser wavelength to 1549.000 nm and the probe laser wavelength to 1549.020 nm, giving a frequency mismatch of approximately 2.5 GHz. The pump–probe mismatch is chosen to be only as large as needed to allow the edge of the pass-band of the probe filter to split the backscattered pump and probe light, thus rejecting any backscattered light from the pump laser and accepting only the backscattered signal from the probe laser. We placed the Stokes filter at 1549.073 nm, an offset of approximately 9.18 GHz from the pump laser to capture the Stokes sideband from the intensity modulator. This corresponds to the center of the measured frequency range and was chosen to allow the Stokes sideband output from the intensity modulator to remain within the pass band of the Stokes filter as the RF signal fed to the intensity modulator is swept through the full measurement range. The probe filter was set to 1549.109 nm, an offset of approximately 11.18 GHz from the probe laser, to capture the Stokes-shifted backscattered signal from the probe. The center frequency of the backscattered signal is of course shifted 9.18 GHz from the probe laser, however an extra offset of 2 GHz is chosen for improved rejection of any pump light as the pass band of our filter extends approximately 2.5 GHz on either side of center.

100 $\text{l}^{1/4}\text{m}$ CS₂ CABS

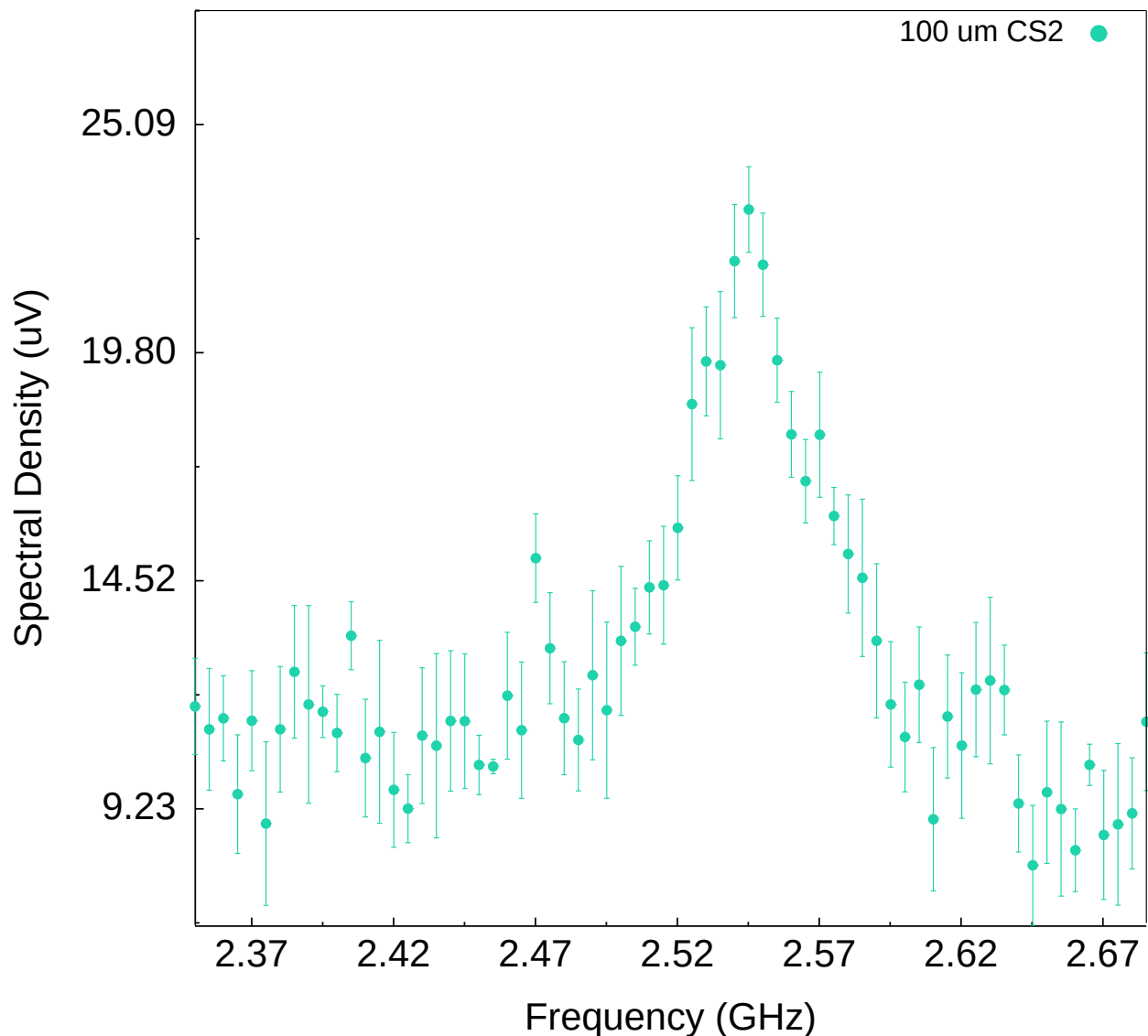


Figure 3.5: 100 μm CS₂

For a free-space bulk example we target liquid CS₂ for its exceptionally high Brillouin gain factor of 1.5 mGW⁻¹.¹ Figure 3.5 reveals the Brillouin signal of bulk CS₂ liquid contained in a 100 μm path length cell. To our knowledge, measurement of longitudinal Brillouin scattering at this scale has not been reported in the literature. A scattered power comparison would reveal that achieving such a measurement using traditional SBS techniques would require excessively high optical powers or cooling the material to cryogenic temperatures, which, of course, would be prohibitive for carbon disulfide in the liquid state.

For this measurement of CS₂, the pump and probe laser wavelengths were set to 1548.808 nm and 1548.898 nm, respectively. The short path length of the sample significantly broadens Φ , the sinc² term defining the phasematching bandwidth, allowing for further separation of the pump and probe wavelengths for improved signal isolation without significant reduction in scattered power of the signal produced in the CS₂. Specifically, the additional pump–probe wavelength separation of 70 pm employed for this measurement compared to the UHNA3 measurement results in a negligible 0.045% reduction in scattered power. This additional separation contributes meaningfully, however, to improved rejection of pump light by the probe filter and thus higher SNR of the signal.

Placement of the Stokes filter is critical for measurements of materials that give small Brillouin shifts, such as with CS₂ 2.55 GHz shift. We offset our 5 GHz bandwidth Stokes filter an additional 2 GHz to ensure the nearby carrier signal and anti-Stokes sideband from the intensity modulator are rejected and only the Stokes sideband is allowed to pass. For the measurement shown in Figure 3.5, this corresponds to a Stokes and probe filter placement of 1548.844 nm and 1548.934 nm, respectively.

3.5.3 Phase Matching Bandwidth

To characterize the phase matching tolerance of the instrument for a given length of sample, we performed an additional experiment whereby we took a series of measurements of 1 cm of UHNA3 at constant optical powers while letting the detuning of the pump and probe lasers vary. In the language of Equation 3.1, this experiment holds G_B , L , P_P , P_S , and P_{Pr} constant while letting Δk vary. For the experiment to support the validation of Equation 3.1, we would expect the peak amplitudes of these measurements to trace out a sinc² profile, also given by Equation 3.5. Figure 3.6 shows the results of this experiment. We performed 75 measurements between 5 GHz and 42 GHz pump–probe detuning, at 0.5 GHz intervals. We found peak amplitudes by fitting each spectra with a Fano profile (see Section 3.5.4) and represented each peak as a data point in Figure 3.6. The theoretical sinc² function matching the parameters used in the experiment is shown on the plot with a solid red line.

1 cm UHNA3 Phase-Matching Bandwidth

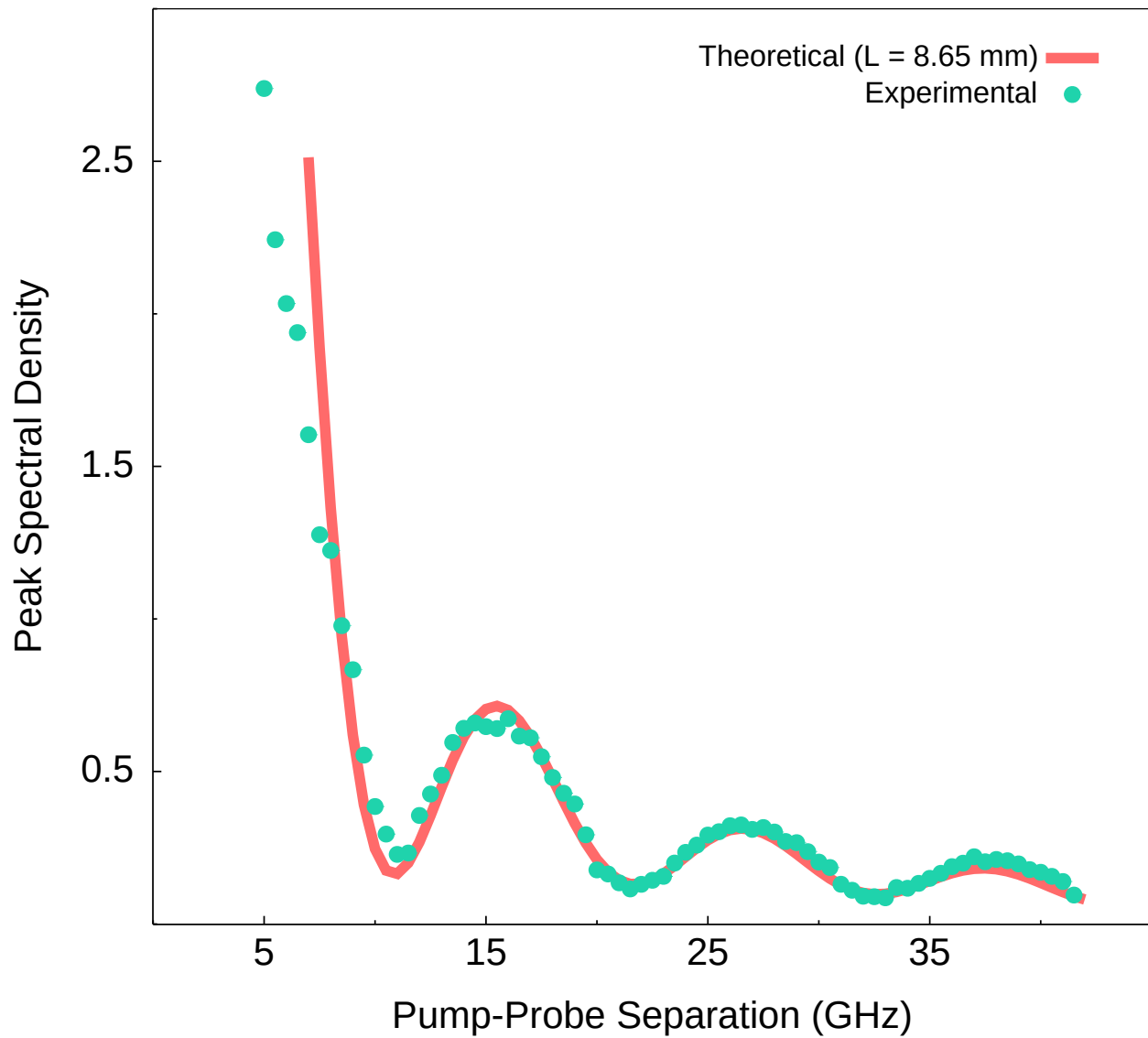


Figure 3.6: Phase-matching sinc^2 func

3.5.4 Fano-Resonant Asymmetries at Small Signals

Under certain conditions where the resonant Brillouin amplitude approaches the background continuum level, we observe an asymmetric, Fano-type line-shape^{34–37}. These Fano distortions can shift the apparent peak frequency, complicate simple Lorentzian fitting, and affect the extracted linewidth in small-signal measurements.³⁸ To properly handle these occurrences, it is necessary to understand when they are likely to arise with this technique and how they may be corrected for or controlled. Fano resonances arise when a discrete resonance (in our case, the Brillouin mode) interferes with a continuum background (e.g., noise floor or broad, non-resonant scattering). When the resonance amplitude is no longer much larger than the continuum, the interference leads to an asymmetric line-shape described by the Fano formula³⁴,

$$I(\omega) \propto \frac{(q + \epsilon)^2}{1 + \epsilon^2}, \quad (3.6)$$

where $\epsilon \equiv (\Omega - \Omega_B)/(\Gamma_B/2)$ is the dimensionless detuning from the Brillouin peak (measured in half the spectral linewidth) and q is the Fano asymmetry parameter. The Fano asymmetry parameter captures the ratio of the resonant scattering to the background scattering amplitudes as well as the relative phase of each. It can be defined as

$$q = \frac{(\text{resonant amplitude})}{(\text{background amplitude})} \cot(\Delta\phi), \quad (3.7)$$

where $\Delta\phi$ is the phase difference between the oscillation driven by the discrete resonant mode and that of the background continuum^{35;39;40}.

In the event of Fano interference, the complex background amplitude often varies slowly with energy and can be seen as having a fixed phase reference, while the resonant amplitude undergoes a rapid π phase change as the energy passes through the resonance.³⁵ When the resonant and background contributions are exactly out of phase at the resonance frequency (phase difference $\Delta\phi = \pi/2$, meaning destructive interference), the spectral line exhibits a dip to zero (anti-resonance) at the discrete resonance frequency, corresponding to $q = 0$ in Equation 3.6. If they are exactly in phase ($\Delta\phi = 0 \text{ or } \pi$, fully constructive interference at resonance), the resonance appears purely Lorentzian without asymmetry and $|q| \rightarrow \infty$. For intermediate phase offsets, one lobe of the resonance is enhanced while the other is suppressed, yielding an asymmetric peak or dip with finite q . The sign of q indicates the direction of asymmetry (which wing of the resonance is enhanced). A positive q means the discrete mode *leads* the background in phase. In this case, the spectral profile has a sharp rise on the low-frequency side and a more gradual fall-off on the high-frequency side. Conversely, a negative q means the discrete mode *lags* the background in phase, leading to a flipped orientation featuring

a sharp rise on the *high*-frequency side and a gradual fall-off on the *low*-frequency side.

We first noticed this behavior appearing in our small-length CS₂ data, where a small shift in probe wavelength revealed an asymmetric line-shape. For the measurements of 100 μm CS₂ (Figure 3.5) and 1 cm UHNA3 fiber at low power (Figure 3.3), the amplitude of the resonant Brillouin peak is on the order of that of the non-resonant continuum, giving a strong chance for Fano interference. Whenever $\frac{I_{\text{res}}}{I_{\text{bkg}}} \approx 1$, the parameter q as given by Equation 3.6 can become finite rather than $\pm\infty$ in the limit that the background is negligible, and Fano interference arises. To explore this further, we performed a similar phase-matching experiment as was done for 1 cm UHNA3 (see Phase Matching Bandwidth subsection), this time with 1 mm of CS₂. Results from this experiment are presented in Appendix B.3 and offer examples of line shapes with pronounced asymmetry and featuring clear characteristic morphologies associated with Fano interference. These pronounced distortions in spectral line shape for small signal measurements underscore the role Fano interference in small resonant amplitudes relative to the background.

Because our instrument offers sub-10 fW sensitivity signal amplitudes have the potential to approach the order of the background continuum amplitude. For this reason, and because the instrument offers an advantage in measurements of samples of short length (<10 m) (see Appendix B.2), Fano effects may often arise with usage of this technique and must be handled appropriately. This includes properly fitting data with a Fano profile as opposed to a Lorentzian to ensure accurate capture of relevant parameters such as linewidth, resonant frequency, and peak amplitude. Beyond fitting and parameter extraction, it is important to be mindful that these effects are likely to occur in ambitious measurements at the limits of equipment sensitivity. Expectation and proper handling of Fano effects in measurements of this nature ensures that they may be more easily recognized and confirmed, as the data is likely to present a spectrum that deviates considerably from the standard Lorentzian. Appendix B.2 offers a comparative analysis of two example spectra featuring highly assymetric profiles fitted with a naïve Lorentzian vs. a more appropriate Fano function.

In some cases, and of particular interest for ambitious measurements, Fano interference may even *boost* the measured peak above the naïve Lorentzian amplitude—i.e., ‘amplify’ it—when $q \neq 0$. In principle, a Fano-type lineshape can exhibit a locally higher peak amplitude than a pure Lorentzian if the discrete Brillouin response constructively interferes with the background continuum near the resonance. Crucially, this does not represent net energy gain but rather a redistribution of intensity through interference. Although the resonance peak may appear taller, the continuum also contributes noise and can partially interfere destructively elsewhere, so the global SNR may or may not improve. Nonetheless, our technique offers the ability to dynamically tune the phase of the Brillouin response relative to the background via adjustment of the probe laser wavelength. This interference-tuning of the continuum and discrete components allows

some control over constructive or destructive interference. Moreover, we can achieve this without sacrificing independent control of the pump–probe detuning: by simultaneously shifting the pump laser in step with the probe, we can preserve the desired phase-matching bandwidth while optimizing the relative phase for Fano interference.

In the phase-matching bandwidth experiment on 1 cm of UHNA3 fiber (Figure 3.6), several effects—noise floor, alignment drifts, fiber dispersion, etc.—slightly distort the ideal sinc^2 response. Near the troughs of the sinc^2 function and for larger pump–probe detunings, the measured Brillouin peaks are weaker and exhibit small spectral asymmetries (see Appendix B.3). This is consistent with a Fano-type distortion in which the Brillouin amplitude and background continuum are comparable, allowing interference to skew the lineshape and shift the peak away from the naïve Lorentzian center. Consequently, a simple Lorentzian fit underestimates the true peak amplitude in these regimes. By fitting a standard Fano profile, we more accurately capture the asymmetric peak and its shifted center frequency.

3.6 Conclusion

In conclusion, we have introduced a coherently stimulated Brillouin spectrometer utilizing a detuned pump–probe design to achieve high sensitivity and room-temperature operation in μm -scale samples. This approach successfully overcomes the spatial resolution limitations imposed by conventional SBS methods, demonstrating sub-10 fW sensitivity in UHNA3 fiber and enabling Brillouin measurements in bulk liquid carbon disulfide with unprecedented efficiency. By relaxing phase-matching constraints, this instrument opens new possibilities for characterizing nanoscale material properties and developing nano-acousto-optic devices in standard laboratory settings without the need for cryogenic environments. Moving forward, our methodology could facilitate advancements in high-resolution phonon spectroscopy and inspire further innovations in the study of material mechanics at the microscale, reinforcing the broader applicability of Brillouin-based techniques across materials science, photonics, and sensing technologies.

Chapter 4

Brillouin-Induced Raman Modes and Device Exploration

4.1 Abstract

4.2 Introduction

4.3 Methods

4.4 Results

4.5 Discussion

Chapter 5

Discussion & Future Work

Appendix A

Supplementary Information for Chapter 2

A.1 Fabrication of CS_2 -Filled Liquid-Core Optical Fiber

Fabrication of the liquid-core optical fiber (LCOF) followed the methods described by Kieu et al. (2012)⁶. The fabrication process involved several key steps for each of the two ends: splicing single mode fiber (SMF-28) to Ultra High Numerical Aperture 7 (UHNA7) fiber, preparing and angle-cleaving fibers, cutting and preparing a protective glass vial, and finally securing the assembly on a microscope slide. Figure 2.2 in the main text illustrates the overall schematic of the fiber fusion strategy, showing how SMF-28 and UHNA7 fibers flank the hollow core. The following sections detail each step in the splicing, assembly, and filling processes in fabricating the CS_2 -filled LCOF.

A.1.1 Splicing

Before integrating the hollow-core segment, a segment of Corning SMF-28 was spliced to Thorlabs UHNA7 fiber. This transition was necessary to gradually match the mode fields and reduce losses at the interface with the hollow-core region.

To begin, a short length (0.5 m) of SMF-28 was stripped, cleaved flat, and arc-spliced to 5–10 cm of similarly prepared UHNA7 fiber. The UHNA7 fiber was fully stripped of its coating prior to arc-splicing. This was done to prevent up-and-down bending of the fiber end in subsequent horizontal alignment with the Vytran fusion splicer. The initial splice was performed with standard parameters, but the arc was then repeated four to five times in order to produce a “tapering” effect which helped narrow the SMF-28 core (9.2 μm diameter) where it contacted the smaller UHNA7 core (2.4 μm diameter), improving coupling efficiency. Prior to and following the splice, optical transmission measurements were taken to assess the splice quality and ensure maximum transmission was preserved.

After the preliminary SMF-28–UHNA7 splice, the UHNA7 fiber needed to be angle-cleaved to ensure a gap remained for CS_2 to be able to enter the hollow-core fiber after fusion-splicing the two fiber segments. An

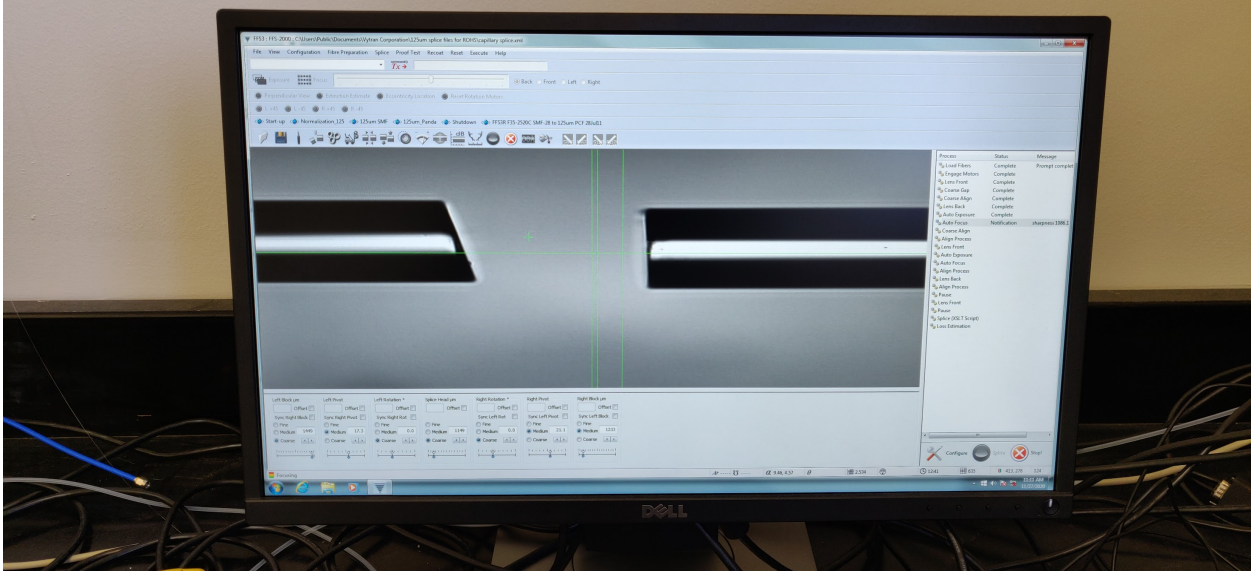


Figure A.1: Picture of Vytran software interface camera imaging system showing a microscope view of the two fiber ends pre-splice (Section A.1.1). The left angle-cleaved fiber is the UHNA7 fiber. The right flat-cleaved fiber is the hollow-core fiber. Subsequent alignment processes, first automatic then manual fine-tuning, align the fibers in xy space for optimal fusion-splicing and optical transmission once filled.

angle-cleaver with an adjustable torque and tension mechanism was used for this process. The angle-cleaved SMF-28-UHNA7 segment was then loaded into the Vytran fusion splicing system:

1. Equipment Setup: The Vytran fusion splicing station and its vacuum pump were turned on, and the system's dedicated software interface was opened. Approximately two minutes was allowed for the vacuum level to stabilize.
2. Fiber Positioning: The left fiber clamp block was pivoted fully to the left, and the UHNA7 fiber was placed so that its freshly cleaved tip was centered over the reference circle at the splice head.
3. Alignment: While the vacuum held the fiber in place, the system's camera view was used to rotate the fiber such that the sharpest angle of the UHNA7's end face was in the camera's view. A small "flag"—a piece of unstripped fiber with a small tape handle on one end—was used as needed to help the clamp grip the bare UHNA7 fiber securely.
4. Pivot and Support: The left block was pivoted back and forth until the UHNA7 tip was near the correct horizontal position. A folded piece of support paper and two boxes of Kimtech Kimwipes on the benchtop were used to prevent the fiber from drooping and to minimize the risk of breakage during handling.

Once the UHNA7 fiber was properly angle-cleaved, the hollow-core fiber segment was prepared for splicing.

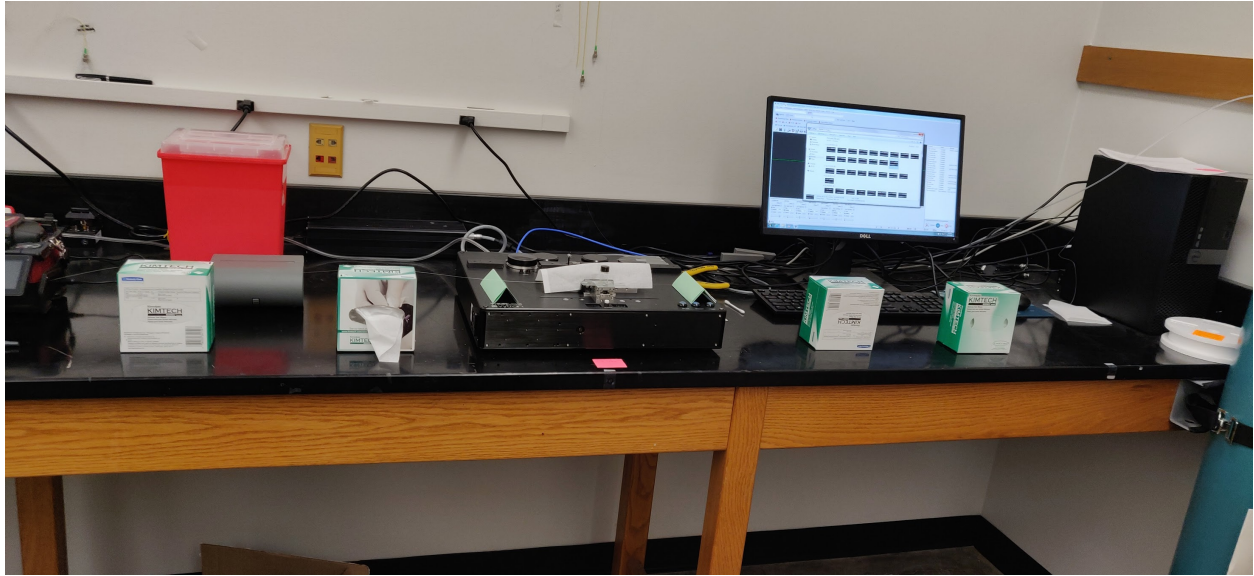


Figure A.2: Picture of both lengths of fiber braced by folded paper and two Kimwipe boxes on either side to prevent bending and flexing while transferring the delicate splice onto a glass slide (Section A.1.1).

ing:

1. Stripping and Cleaving: The hollow-core fiber coating was gently dissolved in acetone and wiped away to expose the bare glass. It was then cleaved flat rather than at an angle.
2. Positioning on the Vytran fusion splicer: The right clamp block was pivoted to its stop position, and the hollow-core fiber was placed so its end was centered over the splice head's circle, ensuring no physical contact with the UHNA7 fiber.
3. Flag and Alignment: As with the UHNA7, a flag of unstripped fiber was placed above the hollow-core fiber to facilitate stable clamping. The right clamp block was slowly pivoted toward the center until the fiber tips were close but still not touching. Like before, the fiber was supported with folded paper and Kimwipe boxes to prevent bending.

The next step was to form the final fusion splice between the UHNA7 fiber and the hollow-core segment within the fusion splicer:

1. Positioning and Auto-Alignment: With both fibers supported and extending naturally from opposite blocks, the splicer's auto-alignment was initiated. The system brought the fibers within viewing distance so the operator could adjust vertical and horizontal positioning.
2. Core Alignment: Using the splicer's camera interface, the UHNA7 core was lined up with the hollow-core's central region. Small vertical and horizontal translations ensured good overlap.

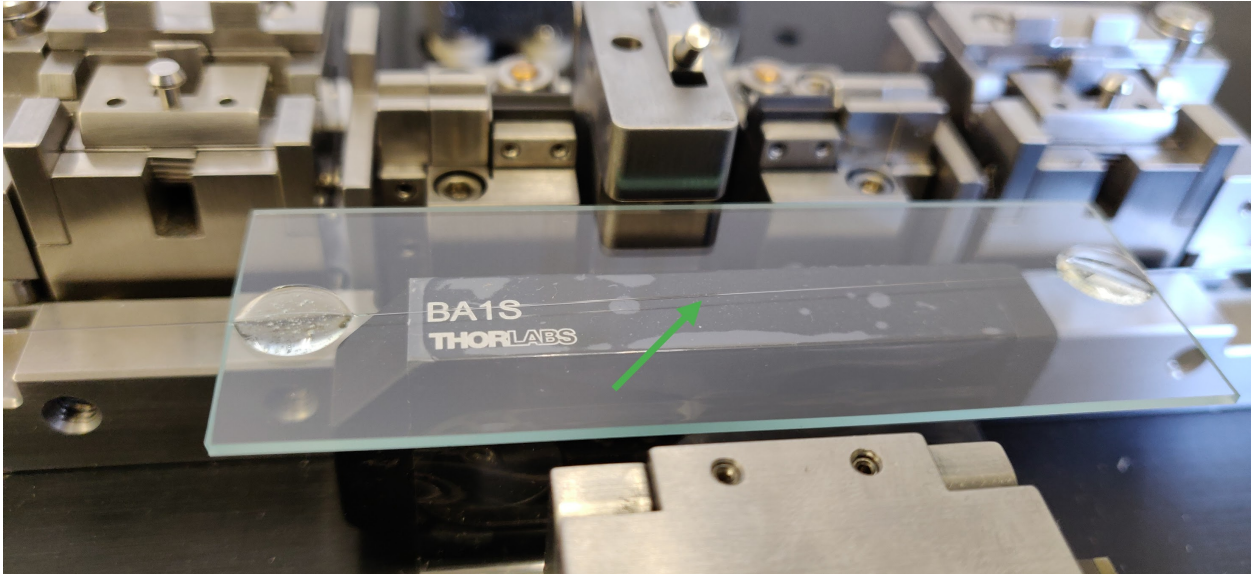


Figure A.3: Picture of splice successfully transferred onto a glass slide and tacked on either side with drops of epoxy (Section A.1.1). An arrow points to the location of the critical splice between the angle-cleaved UHNA7 fiber and the flat-cleaved hollow-core fiber.

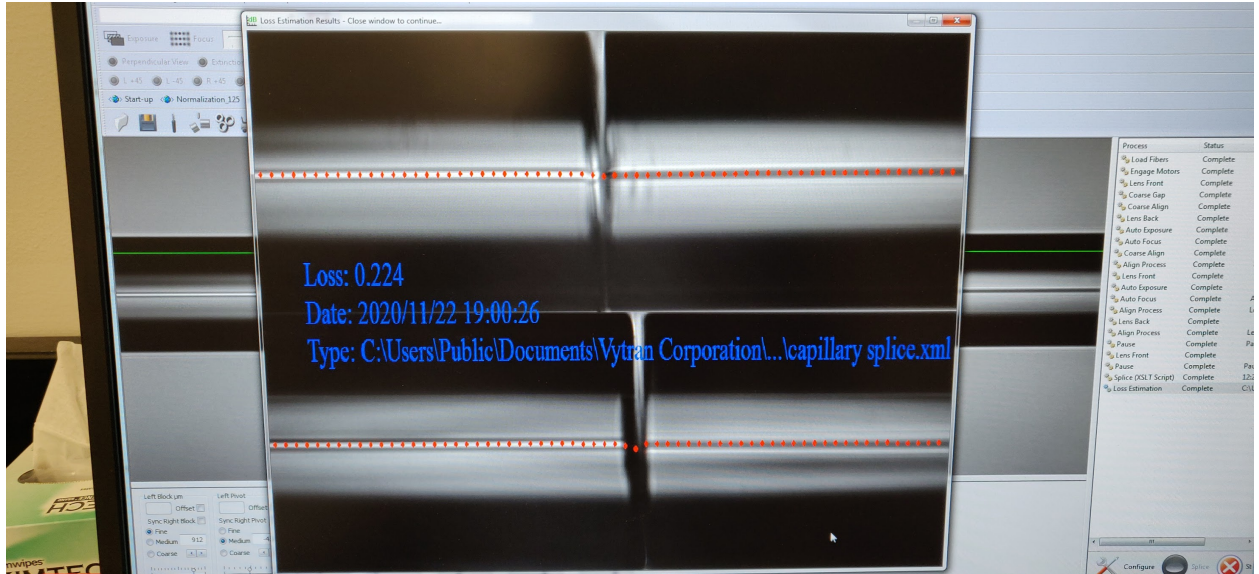
3. Fiber Touch-Off: The left fiber (UHNA7 side) was carefully advanced until the tips touched, then retracted two clicks for optimal separation during splicing. Precise final positioning of the fiber ends ensured that a small gap remained in the hollow core to accommodate liquid infiltration during the filling process. Simultaneously, this same fiber end positioning ensured the cladding regions were fused sufficiently to preserve splice integrity under the delicate handling steps that followed.
4. Argon Gas Flow and Fusion: An argon flow was introduced to shield the fusion region from contaminants, and the fusion filament heating was applied. Images were taken at each step to verify the splice quality. If alignment or splicing was inadequate, the fibers were separated, re-cleaved if necessary, and the procedure repeated. After confirming a good splice, the argon was turned off and the splicer was shut down.

A.1.2 Reservoir Assembly

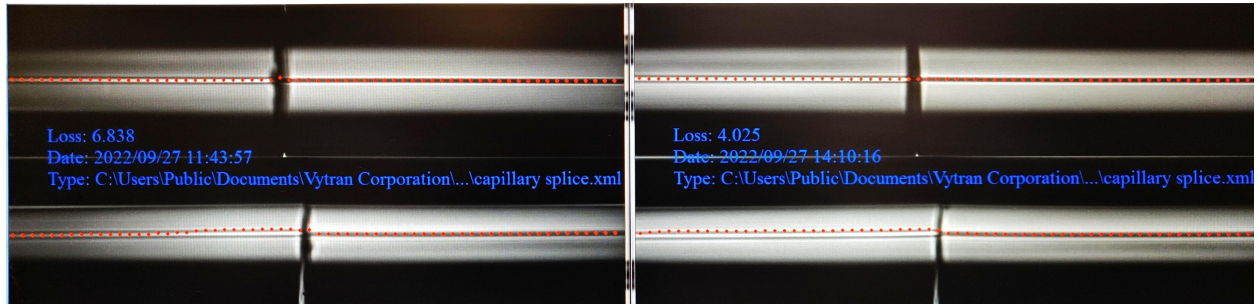
Because the final splice assembly must be encapsulated for protection, it was mounted on a clean microscope slide. The slide was scrubbed with soap and a soft toothbrush under running hot water, then thoroughly rinsed and dried with an air gun. Clean handling was crucial, so the slide was placed inside a folded Kimwipe for safekeeping until needed.

A small glass vial was used to form a protective enclosure over the splice region and allow liquid to fill the hollow core.

1. Cutting the Vial: Wearing gloves and safety glasses, a new glass vial was secured carefully by hand and cut at low rotational speed on a saw. The cut removed only the bottom portion of the vial so that the main body of the vial remained relatively long.
2. Flattening and Notching: The cut edge was smoothed and flattened with a file block, and two shallow, wide straddle-gaps were added on opposite sides of the new opening. These gaps would later accommodate the fiber on the slide.
3. Cleaning: Finally, the vial was scrubbed with dish soap and a pipe cleaner, rinsed, dried with compressed air, and recapped until needed.



(a)



(b)

Figure A.4: Example images of LCOF splices (Section A.1.1). Figure (a) shows an earlier example of a splice which featured a large visible wedge-shaped gap for liquid to enter the hollow-core fiber. While gaps of this size were sometimes successfully transferred onto a slide, further investigation showed gaps of this scale to reduce optical transmission through the splice. This fact became critical later for collecting the data for the pump-probe experiment. Figure (b) shows images of the two splices featured on the ultimate sample which was used to gather final data for publication.

Upon completing the angle splice, the fiber assembly needed to be moved gently off the splicer onto the prepared microscope slide:

1. Release and Stabilization: With the splicer's vacuum pump still on to hold the splice securely, the magnetic latches clamping the fiber on either side of the splice to the translation/rotation stages were carefully lifted. Tweezers were used to remove any fiber "flags," and wooden craft sticks helped lift the fibers from the block grooves to free the fiber from any stuck position within the grooves.
2. Vacuum Shut-Off: The splicer's vacuum pump was switched off and the vacuum seal securing the fibers on either end of the splice was allowed to gradually release as air slowly equilibrated the pressure differential. The splice head and camera assembly remained overtop the splice for monitoring the camera feed on the computer screen. After approximately five minutes the camera feed would show the splice quickly move out of focus, indicating that the entire length of fiber was free and ready to be handled.
3. Placement on the Slide: With the splice head lifted, the slide was positioned directly in front of the splice and the fiber was transferred carefully in a smooth motion. Two small drops of epoxy were placed on each side of the splice region to tack the fiber down. This was allowed to cure for at least five minutes.

The splice region was enclosed in a glass vial to protect the hollow-core's interior and to facilitate later filling with liquid:

1. Positioning the Vial: The prepared vial was placed over the splice region by sliding one straddle-gap around the fiber first, then tilting it so the second gap aligned. Gloves were worn to prevent transferring skin oils onto the vial.
2. Epoxy Sealing: A fresh mixture of two-part epoxy was prepared in roughly equal proportions and thoroughly mixed for 10–15 seconds to ensure a uniform bond. Generous epoxy was applied around the vial's perimeter where it contacted the slide. Care was taken to avoid epoxy wicking into the splice itself. The assembly was then left undisturbed for at least five minutes to cure.

Once the epoxy had set, the slide was labeled with the date, splice reference, and relevant notes using a marker. For long-term handling, the slide and its fibers were taped to a poster board to facilitate transport and prevent accidental breakage from jostling. This procedure ensured a robust, low-loss transition from SMF-28 to UHNA7 to the hollow-core fiber. The careful cleaning steps, controlled splicing environment with argon shielding, and meticulous handling minimized the risk of fiber breakage and guaranteed a clean

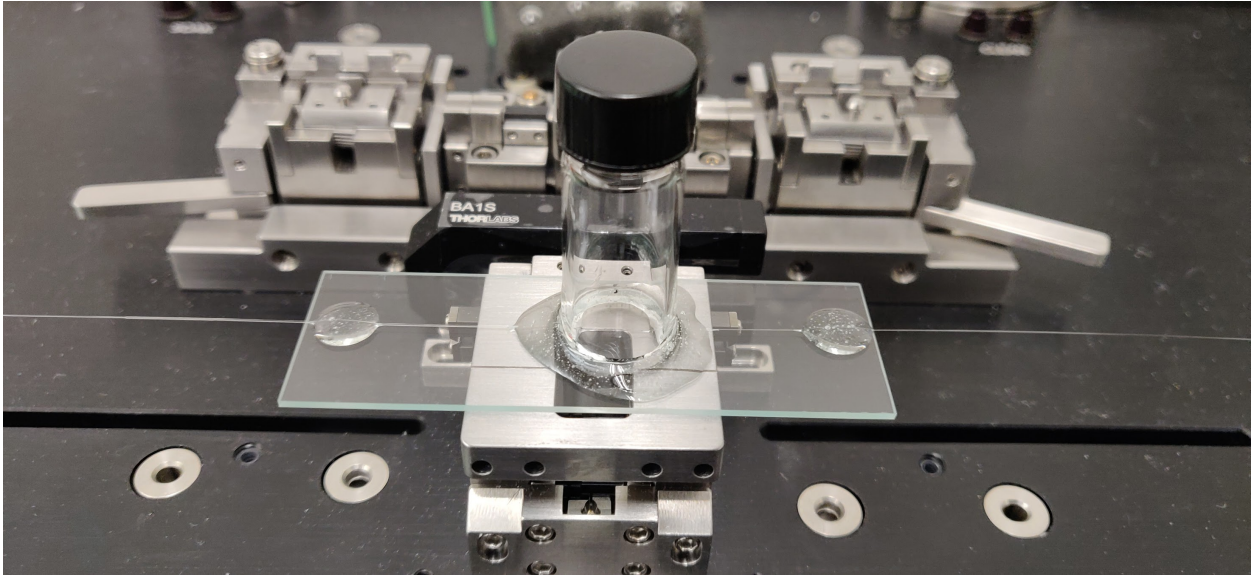


Figure A.5: Picture of a complete splice assembly (Section A.1.2). The hardened epoxy around the base of the vial securely holds the cut and notched vial onto the slide, forming a sealed reservoir around the critical splice. The reservoir is later filled with liquid CS_2 by easy removal of the screw-off cap in order to submerge the critical splice and begin the filling process of the hollow-core fiber via capillary action.

optical interface. Encapsulating the splice with a modified glass vial on a microscope slide allowed easy manipulation of the hollow core's environment, which was crucial for subsequent liquid filling and optical characterization experiments.

Finally, this entire procedure was repeated on the opposite side of the hollow-core fiber to complete the LCOF assembly. Each splice was carefully optimized to be robust enough to guide light but also unfused enough to allow CS_2 to enter the hollow core via capillary action.

A.1.3 Filling with Carbon Disulfide

Once both ends of the hollow-core fiber were successfully spliced to their respective fiber pigtails, the next critical step involved filling the hollow core with carbon disulfide. Because CS_2 is highly volatile and poses health risks if inhaled, all operations were carried out in a fume hood with proper protective equipment.

The prepared LCOF sample, securely taped to a poster board, was transferred to the fume hood. A small red laser source was connected to the input pigtail; this red beam served as an in situ indicator of the fluid-filling front. The vial on the input side was uncapped, and the vial on the opposite side was loosened to prevent pressure buildup within the fiber. This arrangement ensured that as CS_2 entered the hollow core, displaced air could escape through the opposite vial, allowing continuous capillary flow.

To deliver the CS_2 , a syringe was first used to extract an adequate volume from a sealed supply bottle.

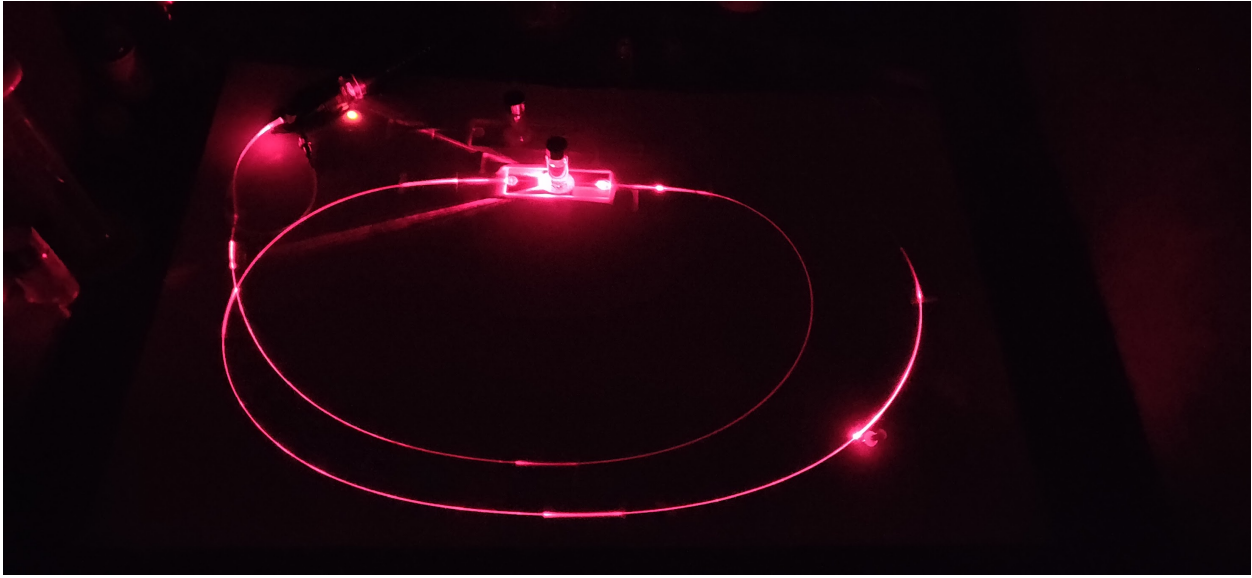
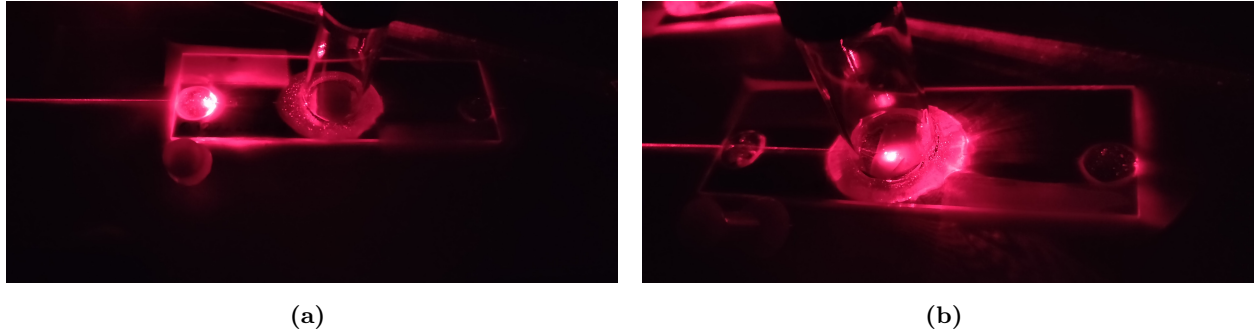


Figure A.6: Picture of a complete sample under the fume hood with lights dimmed and red laser light injected into the end of the sample for monitoring (Section A.1.3). The red light is partially guided along the length of fiber which has filled with liquid CS₂ and a thumb tack marks the progress of the CS₂-air interface.

The needle tip was then removed and replaced with a micron-level particulate filter, thereby minimizing the introduction of debris that could obstruct the hollow core. By gently angling the syringe, CS₂ was dispensed along the interior wall of the vial rather than dripping directly onto the delicate splice region. This careful approach reduced mechanical shocks, which could otherwise fracture or misalign the newly formed splice. Once the vial was filled, it was recapped promptly to prevent evaporation.

If a given splice was imperfect—fully sealed at the fiber core rather than partially open—it prevented CS₂ from flowing in. Under these circumstances, no visible progression of the fluid meniscus would appear in the red laser beam path, confirming an unsuccessful splice. In contrast, if the splice was partially open, capillary action would begin immediately, typically drawing CS₂ several centimeters into the hollow core within seconds. The interface between the CS₂ and the air still occupying the rest of the fiber showed up as a faintly scattering “dot” in the path of the red beam. By darkening the room, this dot could be easily observed and tracked. Once the fiber was fully filled, the second vial was also filled with filtered CS₂, then capped. If the second reservoir was filled prematurely, an air bubble would be trapped in the final short length of hollow-core fiber and the resulting transmission through the full length of the LCOF would be reduced to nearly 0%.

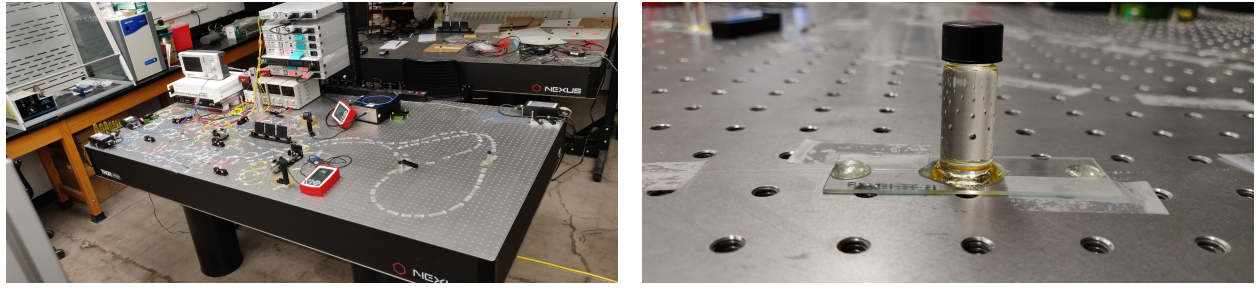
Figure A.6 shows a picture of a sample in the process of filling with CS₂. Progress is marked by a thumbtack next to the CS₂-air interface. With the lights turned off, the dot of scattered light at this interface was a reliable visible indicator. Figures A.7a and A.7b show images of a sample that has nearly



(a)

(b)

Figure A.7: Images of an LCOF sample in the filling process (Section A.1.3). Figure (a) shows the CS_2 -air interface a few centimeters from the end of the length hollow-core fiber, indicated by the red dot of scattered light just underneath the epoxy tack. From this position, the meniscus will typically reach the exit splice in approximately 4 hours. Figure (b) shows evidence of a fully-filled LCOF sample, indicated by the red dot of scattered light having reached the exit splice. If the pictured reservoir were to be filled prematurely, an air bubble would be locked in, reducing full transmission through the sample to nearly 0%.



(a)

(b)

Figure A.8: Images of a fully finished CS_2 -LCOF sample (Section A.1.4). Figure (a) shows a sample secured with tape to an optical table and integrated into an optical setup. Liberal use of tape ensured the safety of the sample as well as reduced vibrations and minimized changes in the polarization of light travelling through the sample. Figure (b) shows one splice assembly secured directly to the optical table via tape. Transfer of all parts of the sample from the poster board directly onto the optical table proved critical for eliminating noise and polarization drift issues with the pump-probe experiment.

finished and fully finished filling, respectively. The filling state captured by Figure A.7a indicates a likely time to finish filling of approximately 4 hours.

A.1.4 Typical Optical Performance

Optical transmission at each splice typically ranged from 5–25%. The final LCOF used to gather the experimental results published in the paper associated with this chapter achieved full throughput transmission of about 17%. This suggests each splice individually offered an average of approximately 41% transmission of the incident light, assuming each splice provided equal transmission. In the demonstration of optomechanical cooling of traveling-wave phonons in this LCOF, the light collected at the detector is backscattered

within the sample and thus passes back through the same splice that the incident pump light enters through. This round-trip backscattered LCOF transmission was treated as approximately equal to the full throughput transmission monitored to be exiting the sample, as light passes through two splices of assumed equal transmission in each case.

Figure A.8 shows two images of a complete LCOF secured to an optical table with Scotch tape and integrated into an optical setup. In later stages of experimentation it was discovered that a large amount of noise and changes in polarization of the light passing through the sample would be incurred if the LCOF were left attached to the poster board used in fabrication and transport. Despite taping all edges of the poster board securely down onto the optical table, minor flexing of the board from small temperature and humidity changes or air drafts in the room caused sufficient instability in the signal to delay successful data collection for the pump-probe experiment (Section 2.4.2).

Over periods of days, some evaporation was inevitable; replenishing the vials every two to three days extended the operational lifetime of the sample. Despite occasional epoxy degradation at the splice site, which might reduce forward transmission, the backscattering experiments remained unaffected except for a loss of forward transmission monitoring. In most cases, weeks-long sample preservation and continued experimentation was feasible with proper maintenance.

A.2 Improvements in Yield and Efficiency of LCOF Samples

A key refinement that greatly improved sample fabrication success rates was the adoption of extremely careful post-splice handling. Previously, standard procedure was to lift the newly spliced fiber assembly without ensuring that each side was completely free of the splicer's grooves. This led to abrupt bending or sudden "snapping" out of the clamp grooves, which almost invariably broke delicate splices that were only partially fused. The implementation of several measures helped to avoid this failure mode. First, folded-paper "sawhorses" and two small Kimwipe boxes on each side of the splice were placed to support the fibers and reduce vibration or flexing. Before switching off the vacuum seal, the clamp latches were gently lifted and small wooden sticks were used to ease the fibers out of the translation/rotation block grooves, ensuring there was no latent twisting or bending. Throughout these steps, the fibers were kept as close as possible to their natural resting position, minimizing stress that would be transferred to the just-completed splice. This careful approach not only reduced the chance of breakage but also allowed for the feasibility of splices that remained sufficiently "open" for CS_2 to enter the hollow core, substantially increasing the proportion of successfully filled samples.

In using the slow-rotation saw to cut and form notches in the glass vial, simple improvements in notch

geometry greatly reduced breakage of splices while placing the vial on the slide overtop the delicate splice, and straddling the fibers on either side. Cutting notches to be ~ 1 cm (10-20 times the width of the fiber) reduced the risk of inadvertently contacting the fibers and breaking the delicate splice during vial placement. Additionally, cutting the notches to be shallow (approximately 5 times the width of the fiber) prevented epoxy from running through the notch and sealing the splice. Previous standard procedure were opposite to this geometry as a natural result of the narrow width of the saw blade and the depth to which it could easily be allowed to cut.

A key innovation in the filling procedure was performing a long observation of the filling process for one sample. Previous standard procedure was to stop monitoring after 8 or 12 hours, assuming the fill process had ceased or completed but subsequently reversed if the fluid had not reached the far end by that time. Through extended trials, it was discovered that in successful splices, the fill front progresses at a nonlinear, steadily decreasing rate, and that a one-meter fiber segment might take more than 24 hours to completely fill. In one particularly instructive case, continuous monitoring for 27 hours without leaving the room as a sample filled confirmed that the CS₂ front never reversed; it merely advanced extremely slowly in the final length to reach the other end. Alarms were set for inspection every 90 minutes throughout the night in the final hours of monitoring the sample under the fume hood. Having observed and documented this behavior, the standard practice became allowing the sample to sit undisturbed for at least a full day or more, ensuring the fiber was completely saturated before concluding success or failure. This observation effort and resulting insight halted the regular production of significant waste of both material and time in the fabrication process of LCOF samples.

A final insight that improved the yield of successfully filled samples and mitigation of wasted materials was selecting the “less certain” end of a prepared sample for filling with CS₂. If that splice was sealed, only that end would need to be re-fabricated. Collectively, these simple method improvements in sample fabrication led to significantly shorter fabrication times and dramatically reduced material waste. Hollow-core fibers, which cost on the order of ten dollar per meter, were previously scrapped in large quantities when deemed “dead.” By implementing patient monitoring, careful handling, and mindful filling procedures each length of fiber was used more efficiently, saving significant time and expense while producing more effective samples.

our

Appendix B

Supplementary Information for Chapter 3

B.1 Coupled-Wave Equations

Here we derive the coupled wave equations that describe coherent stimulated Brillouin scattering involving a pump, Stokes, probe, and backscattered optical field given respectively by

$$\tilde{E}_P(z, t) = A_P e^{i(k_P z - \omega_P t)} + c.c., \quad (\text{B.1})$$

$$\tilde{E}_S(z, t) = A_S e^{i(-k_S z - \omega_S t)} + c.c., \quad (\text{B.2})$$

$$\tilde{E}_{Pr}(z, t) = A_{Pr} e^{i(k_{Pr} z - \omega_{Pr} t)} + c.c., \quad (\text{B.3})$$

$$\tilde{E}_{Sig}(z, t) = A_{Sig} e^{i(-k_{Sig} z - \omega_{Sig} t)} + c.c., \quad (\text{B.4})$$

and a common acoustic field given by

$$\tilde{\rho}(z, t) = \rho_0 + \rho(z, t) e^{i(qz - \Omega t)} + c.c., \quad (\text{B.5})$$

where $\Omega = \omega_P - \omega_S$ and $q = k_P - k_S \approx 2k_P$.

B.1.1 Acoustic Field

As in the case of SBS¹, we start by assuming that the material obeys the acoustic wave equation,

$$\frac{\partial^2 \tilde{\rho}}{\partial t^2} - \Gamma' \nabla^2 \frac{\partial \tilde{\rho}}{\partial t} - v_s^2 \nabla^2 \tilde{\rho} = \nabla \cdot \vec{f}, \quad (\text{B.6})$$

where v_s is the sound speed in the material and Γ' is a damping parameter given by

$$\Gamma' = \frac{1}{\rho} \left[\frac{4}{3} \eta_s + \eta_b + \frac{\kappa}{C_p} (\gamma - 1) \right], \quad (\text{B.7})$$

where η_s and η_b are the shear and bulk viscosity coefficients of the material, respectively. The source term on the right side of Equation B.6 is the divergence of the electrostrictive force:

$$\vec{f} = \nabla p_{st} = \nabla \cdot \left[-\frac{1}{2} \epsilon_0 \gamma_e \left(\langle \tilde{E}_P \cdot \tilde{E}_S \rangle + \langle \tilde{E}_{Pr} \cdot \tilde{E}_{Sig} \rangle \right) \right], \quad (\text{B.8})$$

which yields, assuming the acoustic wave varies slowly in time,

$$\nabla \cdot \vec{f} = \epsilon_0 \gamma_e q^2 (A_P A_S^* + A_{Pr} A_{Sig}^*) e^{i \Delta k z}, \quad (\text{B.9})$$

where $\Delta k = (k_{Pr} - k_{Sig}) - (k_P - k_S)$ is the phase mismatch between the four optical fields. Only two electrostrictive terms survive after accounting for the orthogonal polarization of the pump and Stokes fields with respect to that of the probe and backscattered signal. Inserting this electrostrictive force term (Equation B.9) and the acoustic field (Equation B.5) into the acoustic wave equation (Equation B.6), we find

$$-2i\Omega \frac{\partial \rho}{\partial t} - \Gamma' 2iq^2 \Omega \rho - 2iqv_s^2 \frac{\partial \rho}{\partial z} = \epsilon_0 \gamma_e q^2 (A_P A_S^* + A_{Pr} A_{Sig}^*) e^{i \Delta k z}, \quad (\text{B.10})$$

which can be restated in terms of the Brillouin linewidth, $\Gamma_B = q^2 \Gamma'$, as

$$-2i\Omega \frac{\partial \rho}{\partial t} - 2i\Omega \Gamma_B \rho - 2iqv_s^2 \frac{\partial \rho}{\partial z} = \epsilon_0 \gamma_e q^2 (A_P A_S^* + A_{Pr} A_{Sig}^*) e^{i \Delta k z}. \quad (\text{B.11})$$

Given the phonon dispersion relations $\Omega_B = |q_B|v_s$ and $\Omega^2 = q^2(v_s^2 - i\Omega\Gamma')$, Equation B.11 can be rewritten as

$$-2i\Omega \frac{\partial \rho}{\partial t} + (\Omega_B^2 - \Omega^2 - i\Omega\Gamma_B) \rho - 2iqv_s^2 \frac{\partial \rho}{\partial z} = \epsilon_0 \gamma_e q^2 (A_P A_S^* + A_{Pr} A_{Sig}^*) e^{i\Delta kz}. \quad (\text{B.12})$$

We take the common assumption that the phonon propagation distance is small compared to the distance over which the source term varies significantly, which allows the spatial derivative term in Equation B.12 to be dropped. We further assume steady-state conditions such that the time derivative term also vanishes, leaving

$$(\Omega_B^2 - \Omega^2 - i\Omega\Gamma_B) \rho = \epsilon_0 \gamma_e q^2 (A_P A_S^* + A_{Pr} A_{Sig}^*) e^{i\Delta kz}. \quad (\text{B.13})$$

We thus find the acoustic field amplitude to be

$$\rho(z, t) = \epsilon_0 \gamma_e q^2 \frac{(A_P A_S^* + A_{Pr} A_{Sig}^*) e^{i\Delta kz}}{\Omega_B^2 - \Omega^2 - i\Omega\Gamma_B}. \quad (\text{B.14})$$

B.1.2 Optical Fields

We now turn to the spatial evolution of the optical fields, described by the wave equation,

$$\frac{\partial^2 \tilde{E}_i}{\partial z^2} - \frac{n^2}{c^2} \frac{\partial^2 \tilde{E}_i}{\partial t^2} = \frac{1}{\epsilon_0 c^2} \frac{\partial^2 \tilde{P}_i}{\partial t^2}, \quad (\text{B.15})$$

where i denotes the four optical fields, namely: pump, Stokes, probe, and the backscattered signal. The total nonlinear polarization that gives rise to the source term in the wave Equation is given by

$$\tilde{P} = \epsilon_0 \Delta \chi \tilde{E} = \epsilon_0 \Delta \epsilon \tilde{E} = \epsilon_0 \rho^{-1} \gamma_e \tilde{\rho} \tilde{E}. \quad (\text{B.16})$$

The parts of \tilde{P} that can act as phase-matched source terms for the optical fields are

$$\tilde{P}_P = p_P e^{i(k_P z - \omega_P t)} + c.c. = \frac{1}{2} \epsilon_0 \rho_0^{-1} \gamma_e \rho A_S e^{i(k_P z - \omega_P t)}, \quad (\text{B.17})$$

$$\tilde{P}_S = p_S e^{i(-k_S z - \omega_S t)} + c.c. = \frac{1}{2} \epsilon_0 \rho_0^{-1} \gamma_e \rho^* A_P e^{i(-k_S z - \omega_S t)}, \quad (\text{B.18})$$

$$\tilde{P}_{Pr} = p_{Pr} e^{i(k_{Pr} z - \omega_{Pr} t)} + c.c. = \frac{1}{2} \epsilon_0 \rho_0^{-1} \gamma_e \rho A_{Sig} e^{i(k_{Pr} z - \omega_{Pr} t)} e^{i\Delta kz}, \quad (\text{B.19})$$

$$\tilde{P}_{Sig} = p_{Sig} e^{i(-k_{Sig} z - \omega_{Sig} t)} + c.c. = \frac{1}{2} \epsilon_0 \rho_0^{-1} \gamma_e \rho^* A_{Pr} e^{i(-k_{Sig} z - \omega_{Sig} t)} e^{-i\Delta kz}. \quad (\text{B.20})$$

Inserting the optical fields (Equations B.1-B.4) and phase-matched source terms (Equations B.17-B.20) into Equation B.15, we obtain

$$\frac{\partial A_P}{\partial z} + \frac{n}{c} \frac{\partial A_P}{\partial t} = \frac{i\omega_P \gamma_e}{2nc\rho_0} \rho A_2, \quad (\text{B.21})$$

$$-\frac{\partial A_S}{\partial z} + \frac{n}{c} \frac{\partial A_S}{\partial t} = \frac{i\omega_S \gamma_e}{2nc\rho_0} \rho^* A_P, \quad (\text{B.22})$$

$$\frac{\partial A_{Pr}}{\partial z} + \frac{n}{c} \frac{\partial A_{Pr}}{\partial t} = \frac{i\omega_{Pr} \gamma_e}{2nc\rho_0} \rho A_{Sig}, \quad (\text{B.23})$$

$$-\frac{\partial A_{Sig}}{\partial z} + \frac{n}{c} \frac{\partial A_{Sig}}{\partial t} = \frac{i\omega_{Sig} \gamma_e}{2nc\rho_0} \rho^* A_{Pr}, \quad (\text{B.24})$$

We again assume steady-state conditions, allowing the time derivative term to be dropped. Plugging in the acoustic field amplitude (Equation B.14), we arrive at the coupled-amplitude wave equations for the optical fields,

$$\frac{\partial A_P}{\partial z} = \frac{i\epsilon_0 \omega_P q^2 \gamma_e^2}{2nc\rho_0} \frac{(A_P |A_S|^2 + A_{Pr} A_{Sig}^* A_S) e^{i\Delta kz}}{\Omega_B^2 - \Omega^2 - i\Omega\Gamma_B}, \quad (\text{B.25})$$

$$\frac{\partial A_S}{\partial z} = -\frac{i\epsilon_0\omega_S q^2 \gamma_e^2}{2nc\rho_0} \frac{(|A_P|^2 A_S^* + A_{Pr} A_{Sig}^* A_P) e^{-i\Delta kz}}{\Omega_B^2 - \Omega^2 + i\Omega\Gamma_B}, \quad (\text{B.26})$$

$$\frac{\partial A_{Pr}}{\partial z} = \frac{i\epsilon_0\omega_{Pr} q^2 \gamma_e^2}{2nc\rho_0} \frac{(A_P A_S^* A_{Sig} + A_{Pr} |A_{Sig}|^2) e^{i\Delta kz}}{\Omega_B^2 - \Omega^2 - i\Omega\Gamma_B}, \quad (\text{B.27})$$

$$\frac{\partial A_{Sig}}{\partial z} = -\frac{i\epsilon_0\omega_{Sig} q^2 \gamma_e^2}{2nc\rho_0} \frac{(A_P A_S^* A_{Pr} + |A_{Pr}|^2 A_{Sig}^*) e^{-i\Delta kz}}{\Omega_B^2 - \Omega^2 + i\Omega\Gamma_B}. \quad (\text{B.28})$$

We drop the very small signal amplitude terms on the right side of Equations B.25-B.28 and integrate each along the effective length to get the amplitudes,

$$A_P = \frac{i\epsilon_0\omega_P q^2 \gamma_e^2}{2nc\rho_0} \frac{|A_P|^2}{\Omega_B^2 - \Omega^2 - i\Omega\Gamma_B} \frac{e^{i\Delta k L} - 1}{i\Delta k}, \quad (\text{B.29})$$

$$A_S = -\frac{i\epsilon_0\omega_S q^2 \gamma_e^2}{2nc\rho_0} \frac{|A_P|^2 A_S^*}{\Omega_B^2 - \Omega^2 + i\Omega\Gamma_B} \frac{e^{-i\Delta k L} - 1}{-i\Delta k}, \quad (\text{B.30})$$

$$A_{Pr} = \frac{i\epsilon_0\omega_{Pr} q^2 \gamma_e^2}{2nc\rho_0} \frac{A_P A_S^* A_{Sig}}{\Omega_B^2 - \Omega^2 - i\Omega\Gamma_B} \frac{e^{i\Delta k L} - 1}{i\Delta k}, \quad (\text{B.31})$$

$$A_{Sig} = -\frac{i\epsilon_0\omega_{Sig} q^2 \gamma_e^2}{2nc\rho_0} \frac{A_P A_S^* A_{Pr}}{\Omega_B^2 - \Omega^2 + i\Omega\Gamma_B} \frac{e^{-i\Delta k L} - 1}{-i\Delta k}. \quad (\text{B.32})$$

We focus on the signal amplitude given by Equation B.32, noting that close to resonance, the denominator of the middle term containing Ω can be approximated as,

$$\Omega_B^2 - \Omega^2 + i\Omega\Gamma_B \approx \Omega_B(\Omega - \Omega_B + i\Gamma_B), \quad (\text{B.33})$$

giving

$$A_{Sig} = -\frac{i\epsilon_0\omega_{Sig}q^2\gamma_e^2}{2nc\rho_0} \frac{A_PA_S^*A_{Pr}}{\Omega_B(\Omega - \Omega_B + i\Gamma_B)} \frac{e^{-i\Delta k L} - 1}{-i\Delta k}, \quad (\text{B.34})$$

and in fact on resonance the expression reduces to

$$A_{Sig} = -\frac{i\epsilon_0\omega_{Sig}q^2\gamma_e^2}{2nc\rho_0} \frac{A_PA_S^*A_{Pr}}{\Omega_B i\Gamma_B} \frac{e^{-i\Delta k L} - 1}{-i\Delta k}. \quad (\text{B.35})$$

Using $q = 2k_P = 2\omega n/c$ and $q = \Omega_B/v_s$, we can express the leading terms as

$$A_{Sig} = -\frac{\epsilon_0\omega^2\gamma_e^2}{c^2v_s\rho_0\Gamma_B} A_PA_S^*A_{Pr} \frac{e^{-i\Delta k L} - 1}{-i\Delta k}, \quad (\text{B.36})$$

where we have dropped the signal designator on ω . Defining the Brillouin gain factor, g_0 , as Boyd does,

$$g_0 = \frac{\gamma_e^2\omega^2}{nv_s c^3 \rho_0 \Gamma_B}, \quad (\text{B.37})$$

reduces this expression to

$$A_{Sig} = -\epsilon_0 nc g_0 A_PA_S^*A_{Pr} \frac{e^{-i\Delta k L} - 1}{-i\Delta k}. \quad (\text{B.38})$$

The intensity of the backscattered signal is given by the magnitude of the time-averaged Poynting vector, given by

$$I_i = 2n\epsilon_0 c |A_i|^2, \quad i = 1, 2, 3, \dots \quad (\text{B.39})$$

which produces for the signal intensity

$$I_{Sig} = 2\epsilon_0 nc (\epsilon_0 nc g_0)^2 |A_P|^2 |A_S^*|^2 |A_{Pr}|^2 \left| \frac{e^{-e\Delta k L} - 1}{-i\Delta k} \right|^2 = 2\epsilon_0^3 \epsilon_0 n^3 c^3 g_0^2 \frac{I_P}{2\epsilon_0 nc} \frac{I_S}{2\epsilon_0 nc} \frac{I_{Pr}}{2\epsilon_0 nc} \left| \frac{e^{-e\Delta k L} - 1}{-i\Delta k} \right|^2. \quad (\text{B.40})$$

The squared modulus term containing Δk can be reduced as

$$\begin{aligned} \left| \frac{e^{-i\Delta k L} - 1}{-i\Delta k} \right|^2 &= \frac{(e^{-i\Delta k L} - 1)(e^{i\Delta k L} - 1)}{(\Delta k)^2} = \frac{L^2}{(\Delta k L)^2} \left[2 - 2 \left(\frac{e^{i\Delta k L} + e^{-i\Delta k L}}{2} \right) \right] \\ &= \frac{2L^2(1 - \cos \Delta k L)}{(\Delta k L)^2} = \frac{4L^2 \sin^2 \left(\frac{\Delta k L}{2} \right)}{(\Delta k L)^2} = \frac{L^2 \sin^2 \left(\frac{\Delta k L}{2} \right)}{\left(\frac{\Delta k L}{2} \right)^2} = L^2 \operatorname{sinc}^2 \left(\frac{\Delta k L}{2} \right), \end{aligned} \quad (\text{B.41})$$

giving as a final expression for backscattered signal intensity,

$$I_{Sig} = \frac{1}{4}(g_0 L)^2 I_P I_S I_{Pr} \operatorname{sinc}^2 \left(\frac{\Delta k L}{2} \right). \quad (\text{B.42})$$

To find the power of the backscattered signal, we would integrate this intensity over the effective area. For a uniform area A_{eff} , this gives

$$P_{Sig} = I_{Sig} A_{eff} = \frac{1}{4}(g_0 L)^2 \frac{A_{eff}}{A_{eff}} I_P \frac{A_{eff}}{A_{eff}} I_S \frac{A_{eff}}{A_{eff}} I_{Pr} \operatorname{sinc}^2 \left(\frac{\Delta k L}{2} \right) A_{eff}, \quad (\text{B.43})$$

or,

$$P_{Sig} = \frac{1}{4}(G_B L)^2 P_P P_S P_{Pr} \operatorname{sinc}^2 \left(\frac{\Delta k L}{2} \right), \quad (\text{B.44})$$

where,

$$G_B = \frac{g_0}{A_{eff}}. \quad (\text{B.45})$$

It can be seen that off resonance, the Ω term from Equation B.34 goes to a lorentzian form after taking the squared modulus for intensity.

B.2 Scattered Power Comparison to Traditional Brillouin Scattering Processes

This appendix provides a comparative analysis of the scattered power produced by our instrument to that of standard Brillouin scattering processes—that is, spontaneous and stimulated Brillouin scattering. The difference in behavior of our instrument from the traditional techniques arises due to the coherent stimulation of the acoustic mode by the pump and Stokes fields, producing a 4-wave-coupled-amplitude interaction that yields much higher scattered powers in smaller lengths. While our instrument is particularly well suited to small interaction lengths due to enhanced phase-matching relaxation, it maintains production of a significant amount of scattered power at greater lengths as well (greater than 1 meter). This is because the reduction in scattered power from the breakdown of phase-matching relaxation at greater lengths is perfectly counterbalanced by the quadratic dependence on length in the overall scattered power, as seen in Equation 3.1. At very large lengths (greater than 1 km), the instrument is ultimately limited by the coherence length of the lasers employed, as the process relies on the coherent stimulation of the phonon mode and thus the mutual coherence of the pump and Stokes fields over the interaction length. Here we offer an exploration into the respective performance of each technique across the entire meaningful length scale, from nanometers to kilometers.

Despite shared dependence on basic Brillouin scattering principles, the three techniques compared here (spontaneous-, stimulated-, and coherently stimulated Brillouin scattering) yield significantly different scattered power for identical experimental parameters. At small lengths, the high-gain threshold for optical stimulation of the material fluctuations is often not achievable without the use of extremely large optical powers. This prevents the system from entering a process of exponential growth of the scattered Stokes light indicative of stimulated Brillouin scattering.¹ In this low-gain regime, any scattered Stokes light is spontaneously scattered from thermal fluctuations of the material, or from quantum-mechanical fluctuations of materials at the ground state. The low-gain regime is defined by an overall process gain factor, denoted by $G = G_P P_P L$, which is much less than unity ($G \ll 1$). Here, G_B is the effective Brillouin gain in $W^{-1}m^{-1}$ ($G_B = \frac{g}{A_{eff}}$), P_P is the pump power, and L is the effective length. This spontaneous scattering process follows a linear growth trend described by Boyd et al in 1990⁴¹ as

$$R = \frac{\langle |E_S|^2 \rangle}{\langle |E_P|^2 \rangle} = (\bar{n} + 1)g\hbar\omega_S\Gamma_B \frac{L}{4A_{eff}}, \quad (\text{B.46})$$

where R is the reflectivity, or the ratio of scattered Stokes intensity to incident pump intensity, and $\bar{n} = (e^{\frac{\hbar\Omega_B}{k_b T}} - 1)^{-1}$ is the mean number of phonons occupying the mode due to thermal fluctuations of the material. Rearranging this Equation and converting to effective Brillouin gain, G_B , and power by applying the effective area, we arrive at the scattered power of the Stokes spontaneous Brillouin scattering process,

$$P_S = \frac{1}{4} G_B P_P L \hbar \omega_S \Gamma_B (\bar{n} + 1). \quad (\text{B.47})$$

At room temperature and typical Brillouin frequencies in the GHz range, the quantity $k_b T \gg \hbar \Omega_B$, allowing

$$e^{\frac{\hbar \Omega_B}{k_b T}} \approx 1 + \frac{\hbar \Omega_B}{k_b T} \quad (\text{B.48})$$

to be a good approximation. We thus find that

$$(\bar{n} + 1) \approx \bar{n} \approx \frac{k_b T}{\hbar \Omega_B}. \quad (\text{B.49})$$

Inserting this reduced quantity into Equation B.47, we arrive at a convenient expression for the scattered power of the Stokes spontaneous Brillouin scattering process,

$$P_{S, SpontBS} = \frac{G_B P_P L \omega_S \Gamma_B k_b T}{4 \Omega_B}. \quad (\text{B.50})$$

It may be noted that the derived expression for the low-gain spontaneous regime here matches the form reported by Kharel et al. in 2016⁴² for the complementary forward scattering process. While the two scenarios—our backward scattering geometry versus the forward scattering geometry discussed by Kharel et al.—differ in directionality, the underlying physics of light coupling to thermally excited acoustic modes is the same and reflects the fundamental similarity in how thermal phonons mediate the interaction between optical fields in the low-gain (spontaneous) regime.

Next we turn to the high-gain regime leading to a stimulated Brillouin scattering process. This regime is defined by an overall process gain factor, $G = G_P P_P L$, that is much greater than unity ($G \gg 1$). For organic liquids, this crossover threshold from spontaneous to stimulated regimes occurs in the range of $20 < G < 25$,⁴¹ whereas for typical lengths of single mode fiber it can be lower¹² owing to the small effective area compared to longer effective lengths of fiber typically used.

The reflectivity of a stimulated Brillouin scattering process in the high-gain regime is given by⁴¹

$$R = \frac{\langle |E_S|^2 \rangle}{\langle |E_P|^2 \rangle} = \frac{Y}{\sqrt{\pi}} \frac{e^G}{G^{\frac{3}{2}}}, \quad (\text{B.51})$$

where Y is the reflectivity of the low-gain (spontaneous) regime given above and G is the overall process gain factor, $G = G_P P_P L$. Again, converting to the effective Brillouin gain, G_B , and power by applying the effective area, we solve for the scattered power of the Stokes field,

$$P_{S, StimBS} = \frac{G_B P_P L \omega_S \Gamma_B k_b T}{4\sqrt{\pi} \Omega_B} \frac{e^G}{G^{\frac{3}{2}}} \quad (\text{B.52})$$

This expression captures the exponential growth in scattered power as any parameter within the overall process gain factor, $G = G_B P_P L$, increases. However, this exponential growth can only continue while the pump is not significantly undepleted. Once the scattered power described by Equation B.52 grows to a significant fraction of the driving pump power, the exponential increase in scattered Stokes power asymptotically approaches the pump power. For very large G , virtually all of the pump energy is converted to scattered Stokes energy in a complete transfer process.¹ To account for pump depletion, we numerically solve the transcendental Equation derived in Boyd's Nonlinear Optics which describes the effects of pump depletion, given here in terms of power as

$$P_S(L) = \frac{P_S(0)x(1-x)}{e^{G_B P_P(0)L(1-x)} - x}, \quad (\text{B.53})$$

where $x = P_S(0)/P_P(0)$, or the ratio of the unknown Stokes power at the end of its journey through the medium ($z = 0$) to the known pump power at the beginning (also $z = 0$). This solution for x , specific to system parameters such as length, offers via its definition the solution to the unknown power of the scattered Stokes light at the end of its traversal through the effective length, given as

$$P_S(0) = xP_P(0). \quad (\text{B.54})$$

The solution to this numeric approach to scattered power in the high-gain (stimulated) Brillouin scattering regime with pump depletion effects at large G is plotted for varying effective lengths in Figure B.1, along with the analytical solutions derived previously for the low-gain (spontaneous) regime and our coherently stimulated Brillouin spectrometer given by Equation 3.1. System parameters used to generate the plot for each of the three processes are provided in Tables B.1 and B.2. Wherever possible, the parameters shared by all three Brillouin scattering processes were kept consistent, while quantities unique to each process were assigned their respective values.

Coherently Stimulated Brillouin Scattering Process Model System Parameters

G_B	P_P	P_S	P_{Pr}	$\Delta\lambda$
$0.6 \text{ W}^{-1}\text{m}^{-1}$	1 W	1 W	1 W	20 pm

Table B.1: Parameters relevant to the coherently stimulated backward Brillouin scattering process for the example UHNA3 fiber. G_B is the effective Brillouin gain, P_P is the pump power, P_S is the Stokes power, P_{Pr} is the probe power, and $\Delta\lambda$ is the wavelength detuning of the probe from the pump.

At lengths beyond a centimeter, the phase-matching relaxation of the coherently stimulated process begins

Spontaneous and Stimulated Scattering Process Model System Parameters

G_B	P_P	$P_{S,seed}$	n	λ_P	Γ_B	k_B	T	Ω_B
$0.6 \text{ W}^{-1}\text{m}^{-1}$	1 W	1 pW	1.48	1549 nm	$2\pi \cdot 80 \text{ MHz}$	$1.38 \times 10^{-23} \text{ J/K}$	295 K	$2\pi \cdot 9.18 \text{ GHz}$

Table B.2: Parameters relevant to the spontaneous and/or stimulated backward Brillouin scattering processes for the example UHNA3 fiber. G_B is the Brillouin gain coefficient, P_P is the pump power, ω is the optical angular frequency, Γ_B is the acoustic damping rate, k_B is Boltzmann's constant, T is the temperature, and Ω_B is the acoustic angular frequency.

to break down, and the specific choice in pump and probe detuning becomes critical. This corresponds to a narrowing of the $sinc^2$ function given in Equation 3.5. The scattered power beyond this length rises and falls according to the oscillations of the $sinc^2$ function far from the origin. As length increases continuously beyond 1 meter, the scattered power oscillates with increasing frequency and ceases to offer practical significance. To better visualize the scattered power offered by the instrument in this region, we have computed the envelope of scattered power. In a laboratory setting, the appropriate pump and probe detuning would be selected for the specific sample length being measured such that the scattered power function lies on a local peak of the $sinc^2$ function.

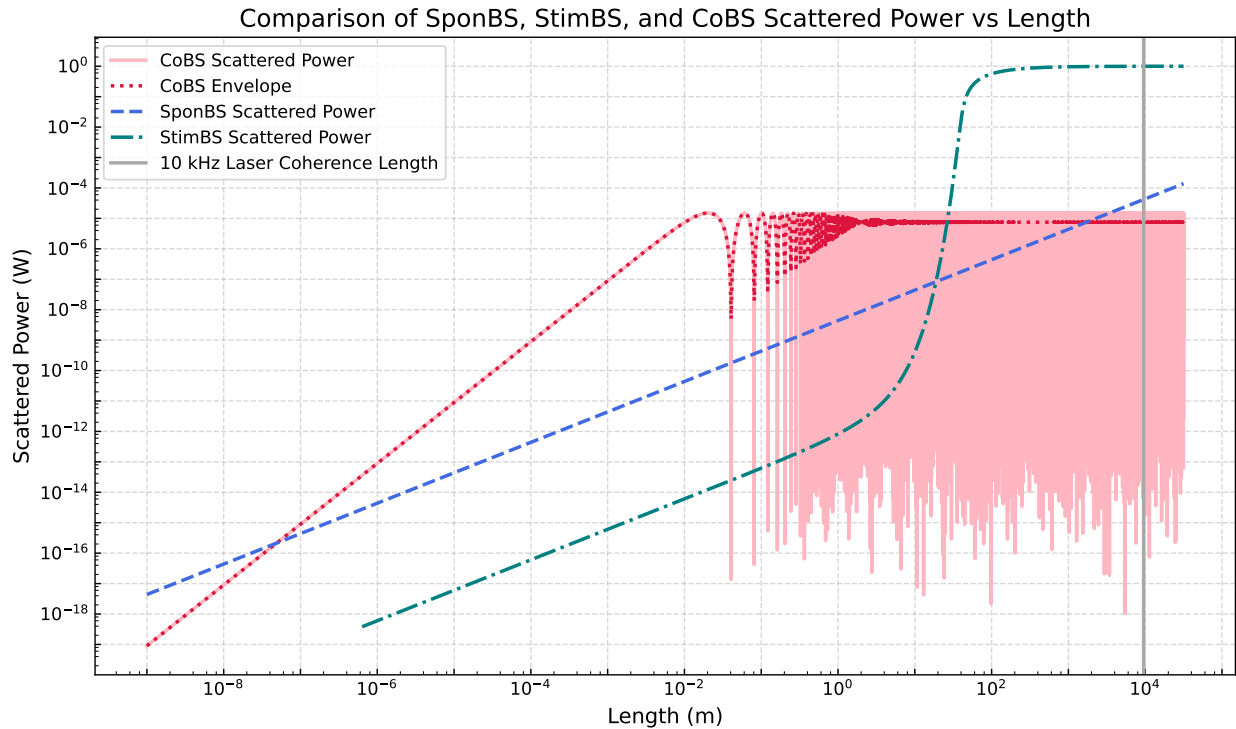


Figure B.1: Comparison of scattered power from a spontaneous Brillouin scattering process and our coherently stimulated Brillouin spectrometer.

Figure B.1 shows the advantage that our coherently stimulated Brillouin spectrometer offers compared to the traditional Brillouin processes for the example medium of UHNA3 fiber. For lengths up to about 50

meters and down to as low as 100 nanometers, the coherently stimulated process employed by our instrument offers superior scattered power, with the relative advantage peaking for a length just under 1 cm. At this length, the gain factor G places the traditional process within the low-gain (spontaneous) regime, and thus the scattered power generated is only on the order of 10s of picoWatts. In contrast, the scattered power for the same system offered by our instrument is on the order of 10s of microWatts, exceeding that of the spontaneous process by a factor of a million. This is, of course, the most ideal case for this system, however it can be seen from Figure B.1 that the coherently stimulated process offers orders of magnitude more scattered power than either traditional process through a wide range of lengths.

B.3 Observance of Fano-Resonant Asymmetries at Small Signals

In *Fano-Resonant Asymmetries at Small Signals* (Section 3.5.4 in the main text), we discussed how Fano-type interference can distort Brillouin line shapes in situations where the resonant Brillouin amplitude becomes comparable to the background continuum. We focus here on two experiments (A and B) that reveal these Fano asymmetries especially clearly. Experiment A is a measurement series using the same 1 cm UHNA3 fiber referenced in the main discussion, for which the main text showed only the fitted amplitudes (Figure 3.6). Here we show the full spectra, illustrating the emergence of asymmetries at lower amplitude conditions. Experiment B is a distinct measurement involving a short (~ 1 mm) bulk liquid sample of carbon disulfide (CS_2) that we briefly mentioned in Section 3.5.4 but did not detail. This experiment was performed specifically to further probe the unexpected Fano-like distortions observed in Experiment A. In each case, we outline the experimental setup, present the spectra, and highlight the appearance of Fano resonances. These observations corroborate the theoretical discussion of Fano line shapes (Section 3.5.4) and provide insight into when and why they are most prominent.

B.3.1 Experiment A: Extended 1 cm UHNA3 Fiber Spectra

In Section 3.5 of the main text, we introduced a phase-matching experiment on 1 cm of UHNA3 fiber in which the pump-probe detuning was varied from 5 GHz to 42 GHz in 0.5 GHz increments. There, we reported only the resulting peak amplitudes, showing how they follow a sinc^2 dependence on detuning (Figure 3.6 in the main text). However, each measurement in that scan also yields a full Brillouin spectrum—75 in total. Here, we present all 75 spectra to illustrate how the line shape transitions from nearly Lorentzian (when the Brillouin peak amplitude greatly exceeds the background continuum) to distinctly Fano-like (when the two amplitudes are comparable). We used the same setup and procedure described in *Phase Matching Characterization* in Section 3.5 of the main text. As the pump-probe detuning increases, the phase-matching term $\text{sinc}^2(\Delta kL/2)$ oscillates through peaks and troughs, causing the Brillouin peak amplitude to rise and fall. When the amplitude is sufficiently large, the Brillouin mode dominates the continuum and the spectrum appears nearly Lorentzian; when it drops to the order of the background amplitude, strong interference skews the line shape into a Fano-like profile.

Figure B.2 highlights the progressive shift from Lorentzian to asymmetric line shapes. Near 5 GHz detuning (top spectra), the resonant amplitude is large relative to the background, giving a classic Lorentzian peak ($|q| \rightarrow \infty$) at the resonance frequency (~ 9.17 GHz). By contrast, at detunings between ~ 15 - 20 GHz, where the sinc^2 factor is near a local minimum, the peak amplitude falls to roughly the same level as the continuum, and Fano interference is observed. Interestingly, as the detuning is increased further, and the

amplitude rises again on a subsequent “lobe” of the sinc^2 function, the spectra partly recover a Lorentzian shape. This cyclical behavior persists, with each local maximum yielding a near-Lorentzian profile and each local minimum reintroducing a strong Fano distortion. These observations confirm the relationship between Brillouin peak amplitude and continuum interference described in *Fano-Resonant Asymmetries at Small Signals* in Section 3.5. When the Brillouin amplitude significantly exceeds the background, the discrete phonon resonance dominates, resulting in little or no asymmetry ($|q| \rightarrow \infty$). Once the two amplitudes become comparable, Fano interference skews the line shape, shifting the apparent peak frequency slightly and altering the slope on either side of the resonance. Analyzing selected spectra with both Lorentzian and Fano fits indicates that ignoring these distortions can lead to up to a 5–10% misestimation of peak amplitude in the “trough” (low-amplitude) sets. This underscores the importance of employing a Fano model in small-signal measurements where the Brillouin peak may not tower over the background. A comparative analysis of a Lorentzian vs. Fano fit function applied to highly assymetric spectra is explored in the following section, for data gathered from Experiment B.

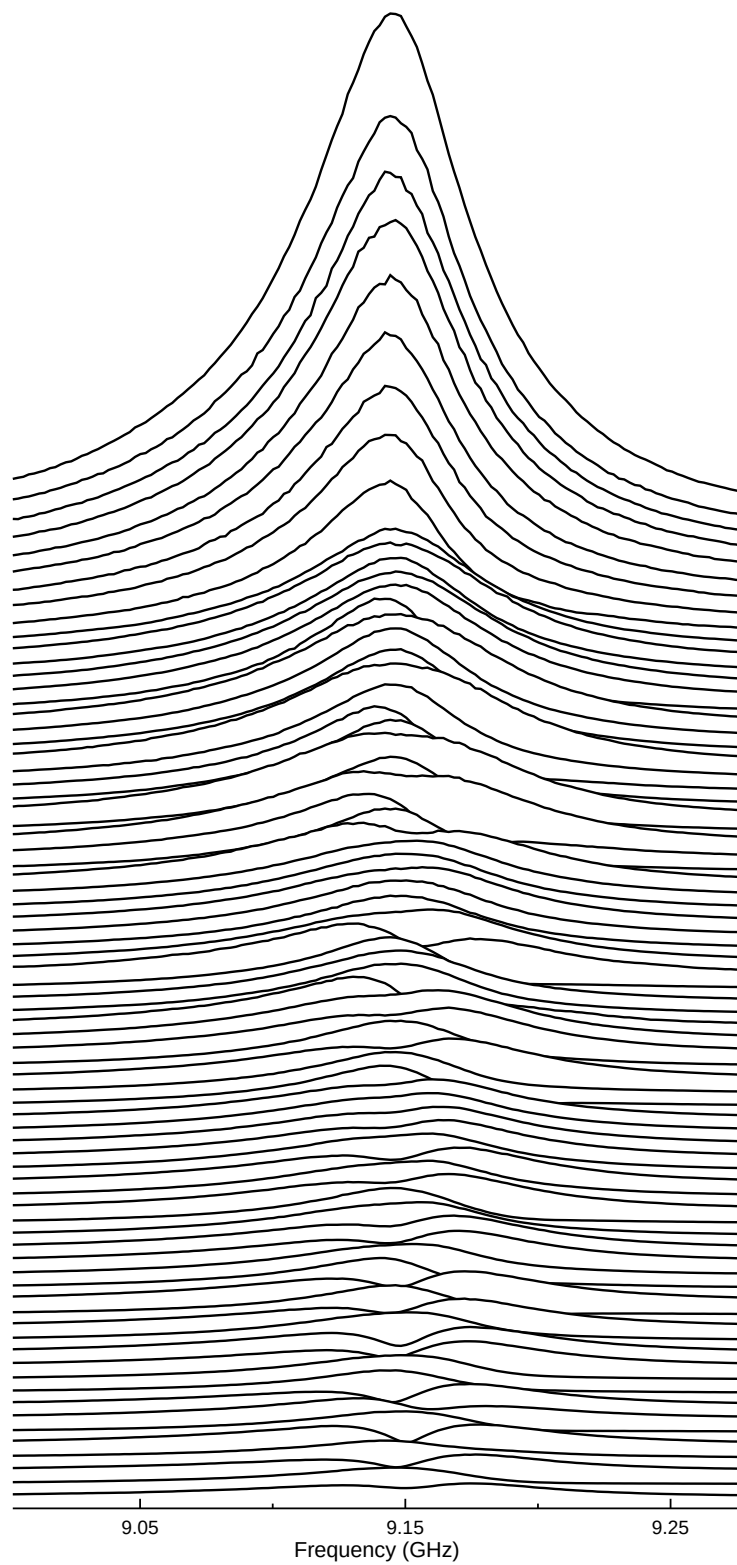


Figure B.2: All measured Brillouin spectra for 1 cm UHNA3 at detuning steps of 0.5 GHz from 5 GHz (top spectrum) to 42 GHz (bottom spectrum). Each trace is offset for clarity. The resulting asymmetries highlight the characteristic Fano-resonant behavior under low signal conditions.

B.3.2 Experiment B: 1 mm CS₂ Spectra and Fano Distortions

We now turn to measurements on a 1 mm-thick cell of CS₂ in a free-space geometry, complementing the 1 cm UHNA3 fiber results (Experiment A). Both experiments used comparable sub-Watt optical powers (on the order of \sim 60–70 mW pump, \sim 25–30 mW Stokes, and \sim 40–50 mW probe). However, unlike Experiment A, which probed a 1 cm fiber with 0.5 GHz detuning increments from 5 GHz to 42 GHz, here the detuning is stepped in 0.25 GHz increments between 10 GHz and 14 GHz. Because the CS₂ sample is an order of magnitude shorter (1 mm vs. 1 cm), its phase-matching bandwidth (sinc² profile) is roughly ten times wider, making these 0.25 GHz steps effectively twenty times finer than the 0.5 GHz steps used in the fiber experiment. This reduced range of detunings within a broader sinc² profile produce measured peaks all of similar amplitude to one another, as opposed to the dynamic evolution of peaks in the 1 cm UHNA3 fiber data.

Figure B.3 shows all 17 spectra obtained at detuning increments of 0.25 GHz, presented in order of increasing detuning from top spectrum to bottom spectrum. Each trace is offset vertically for clarity, with the topmost spectrum corresponding to 10 GHz and the bottom spectrum corresponding to 14 GHz detuning of the pump and the probe. A change in the detuning of the pump and probe via adjustment of the probe laser wavelength produces a change in phase of the resonant Brillouin signal. This changing resonant Brillouin phase relative to the background continuum produces spectra with different Fano-resonant distortions corresponding to specific values of the Fano parameter, q , as discussed in *Fano-Resonant Asymmetries at Small Signals* in the main text (Section 3.5.4). Fano-resonant asymmetries are seen in nearly every spectrum of this liquid experiment, indicating that the background continuum is competing strongly with the Brillouin amplitude in all measurements.

The Brillouin amplitudes featured in this experiment are an order of magnitude lower compared to the highest amplitudes seen in Experiment A. This is caused by the order of magnitude shorter sample length of CS₂ (1 mm) as compared to the 1 cm length of UHNA3 fiber used in Experiment A. The \sim 1000 times higher Brillouin gain offered by the CS₂ (1.5 m GW^{-1}) is discounted significantly by the \sim 350 times larger effective area offered by the beam waist in the free-space optical setup compared to the core of UHNA3 fiber used in Experiment A ($\sim 17 \mu\text{m}$ radius beam waist vs. $\sim 0.9 \mu\text{m}$ radius core of UHNA3). The effective Brillouin gain of the CS₂ used in Experiment B is thus a net ~ 3 times greater than that of the UHNA3 fiber. From Equations 3.1 and 3.2 in the main text, scattered power scales with the square of both the length and the effective Brillouin gain of the sample ($P_{\text{Sig}} \propto L^2 G_B^2$). Cumulatively, this makes for an approximate order-of-magnitude signal reduction for similar optical powers and pump-probe detuning.

However, both experiments (A and B) feature a sweep through a range of pump-probe detunings, with Experiment B featuring a step size effectively 25 times finer than that of Experiment A. This further cor-

robicates these two data sets, as the signal reduction from near-center peak to a side trough of the sinc^2 profile is also on the order of a 10 times reduction (Figure 3.6). This places the signal amplitudes of the CS_2 spectra from Experiment B (all near *peak-center* of its sinc^2 profile) on the same order as the signal amplitudes near the *troughs* of the UHNA3 fiber spectra from Experiment A. These spectra all share strong Fano asymmetries, indicating as they should that they all sit in a similar signal amplitude range: small enough that the background continuum competes but does not dominate over the signal.

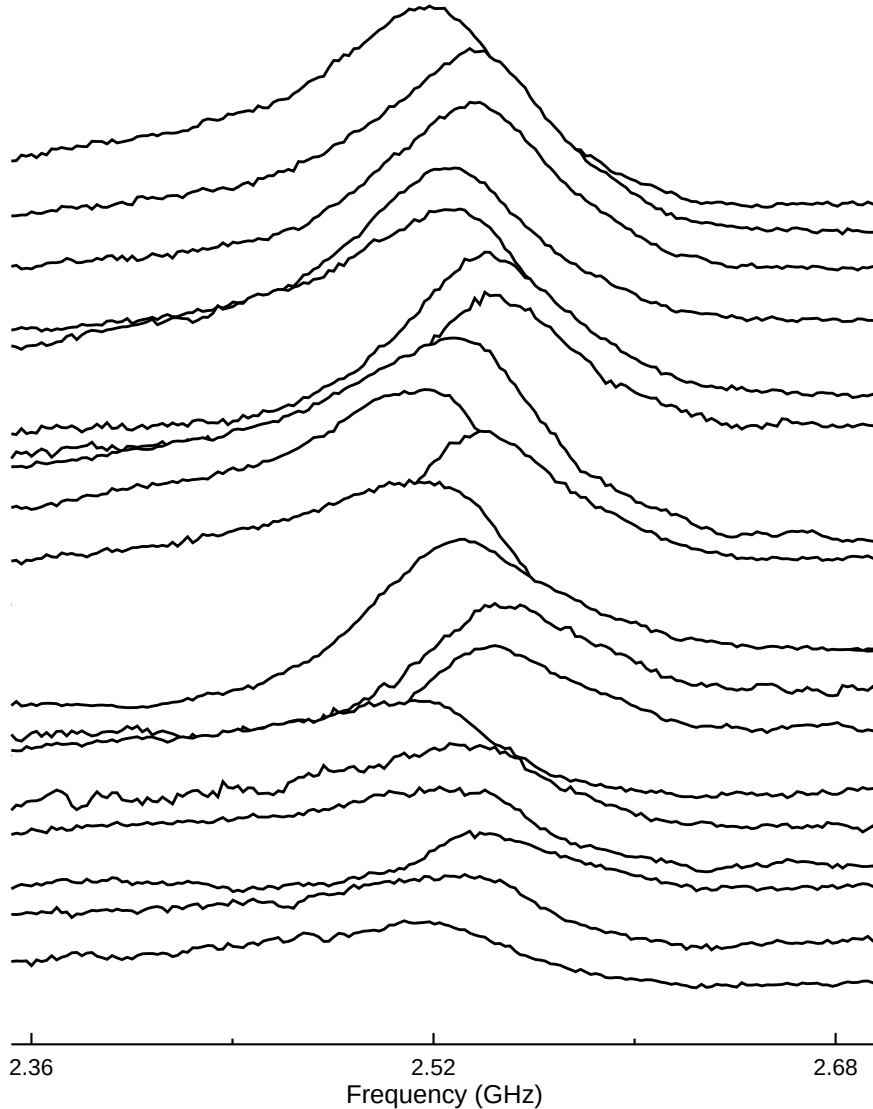


Figure B.3: All measured Brillouin spectra for 1 mm CS_2 at detuning steps of 0.25 GHz from 10 GHz (top spectrum) to 14 GHz (bottom spectrum). Each trace is offset for clarity.

To illustrate the strong distinction in line-shape of a spectra resulting from a positive vs. negative q value, we focus on two particular detunings that yielded notably skewed line shapes: 11 GHz and 13 GHz. Figures B.4 and B.5 compare the spectra for these two detunings normalized relative to the slightly larger

peak amplitude of the 11 GHz spectra. The line-shape of the 11 GHz spectrum exhibits a sharper rise on the higher-frequency side and a gentler roll-off on the lower-frequency side, indicative of $q < 0$, whereas that of the 13 GHz spectrum is skewed oppositely, featuring a sharper low-frequency side and a softer high-frequency roll-off, suggesting $q > 0$. Figure B.4 shows these two spectra with uncertainty-weighted Fano function fits applied, with the corresponding reduced χ^2 values reported in the legend. The Fano fits yield reduced χ^2 values of 2.45 and 8.41 for the 11 GHz and 13 GHz spectra, respectively (reduced χ^2 values near unity indicate a good fit to the data). Figure B.5 shows these same spectra with naïve Lorentz function fits applied and their corresponding reduced χ^2 evaluations of goodness-of-fit. These Lorentzian fits yield reduced χ^2 values of 39.45 and 146.5 for the 11 GHz and 13 GHz spectra, respectively, indicating that the Lorentzian function is a very poor fit to the data.. The poor fit of the Lorentzian function is due to its inherent symmetry, whereas the underlying data exhibit strongly asymmetric lineshapes. These results clearly demonstrate the superiority of the Fano model in capturing the asymmetry of small signals produced by the instrument due to Fano interference with the background continuum. This, in turn, emphasizes the importance of applying a Fano fit function when asymmetries arise to accurately extract valuable spectra parameters such as peak amplitude, center frequency, and linewidth from the data.

Notably, in the 11 GHz case, our Fano fit reveals a local amplitude slightly higher than what the Lorentzian fit suggests, sometimes referred to as a “peak boost.” In essence, partial *constructive* interference between the discrete Brillouin response and the broad continuum locally raises the amplitude, although it does not imply any net energy gain. As mentioned in *Fano-Resonant Asymmetries at Small Signals* (Section 3.5), this effect can aid in detecting weak resonances if the background is not too noisy. One could, in principle, tune the phase relationship to maximize this interference near the resonance, possibly producing a sharper or taller peak for certain values of q than would be achieved without interference with the background. This Fano interference-tuning of the discrete mode relative to the background can be done dynamically via adjustment of the probe laser wavelength and, critically, can be adjusted independently from the phase-matching bandwidth tuning (pump-probe detuning). This ability to dynamically adjust the discrete-continuum interference is an elegant and notable feature, as in typical systems this is adjusted via changes in physical geometry or material doping of the sample.^{39;40;43}

1 mm CS₂ CABS

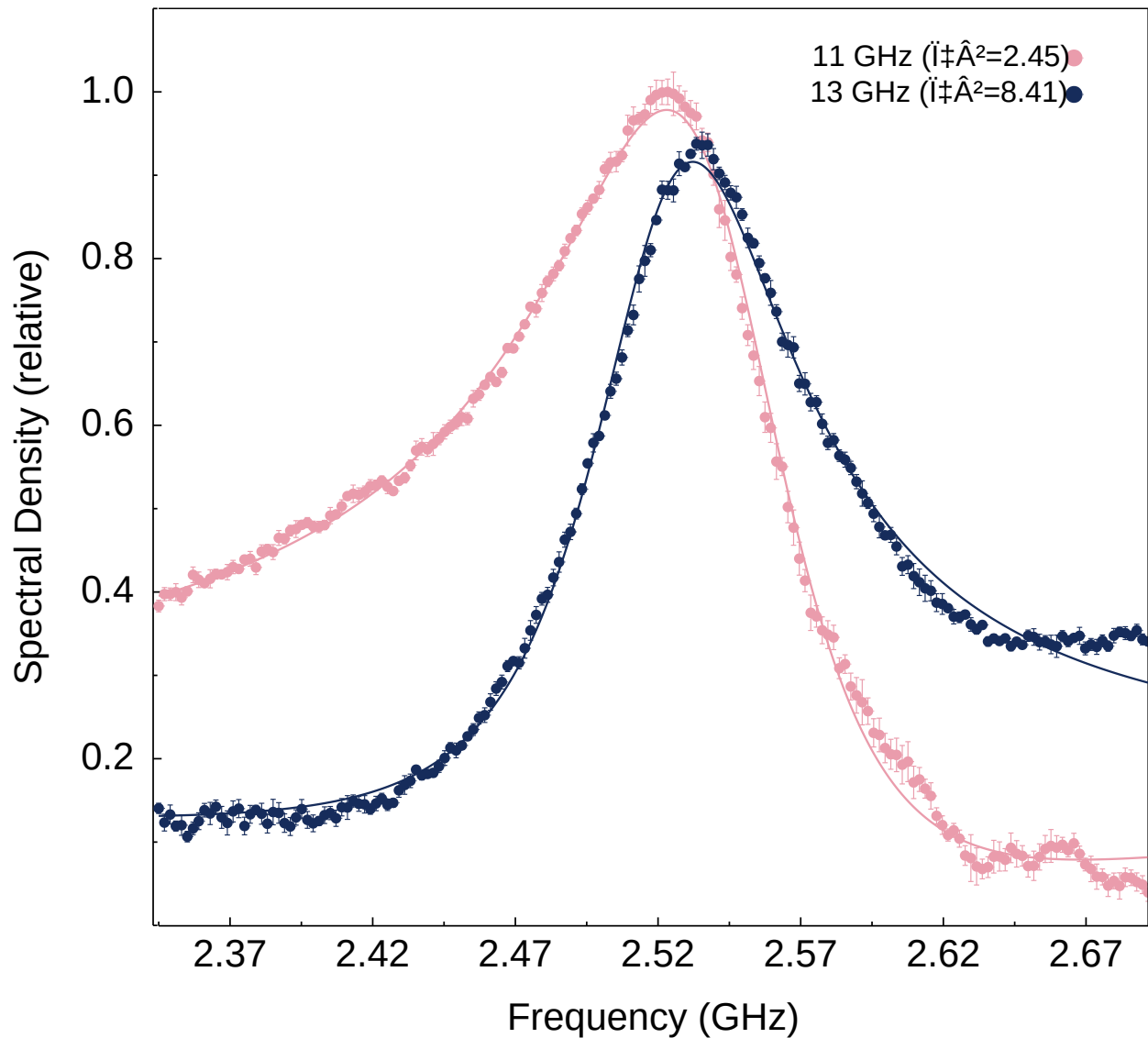


Figure B.4: Comparison of representative spectra at 11 GHz and 13 GHz, showing the positive vs. negative q asymmetry in 1 mm CS₂. A Fano function fit has been applied to each spectra, with χ^2 value for each fit listed in the plot legend.

1 mm CS₂ CABS

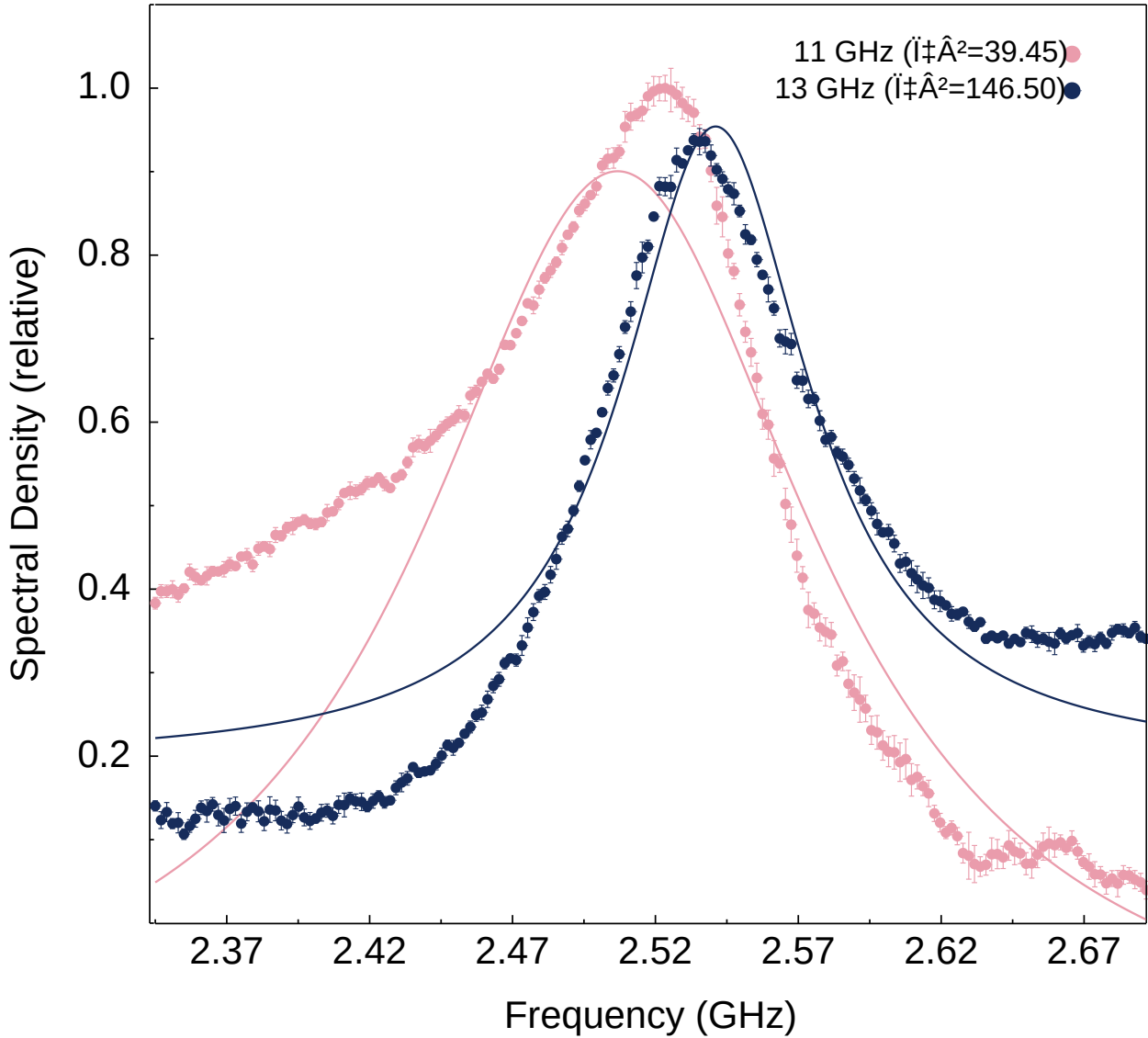


Figure B.5: Comparison of representative spectra at 11 GHz and 13 GHz, showing the positive vs. negative q asymmetry in 1 mm CS₂. Here, a naïve Lorentz function fit has been applied to each spectra, with χ^2 value for each fit listed in the plot legend. These spectra show strong Fano-resonant asymmetry and thus the standard Lorentz function offers a poor fit for these spectra, quantified by the χ^2 evaluation metric for goodness of fit as compared to the same evaluation of the Fano function fit.

To better convey the cyclical evolution of the 75 measured UHNA3 spectra from Experiment A, several animated GIFs have been generated. The following is a link to the GitHub repository which hosts these files, along with all raw data, measurement logs, and plots generated in support of this work (see See Appendix D):

<https://github.com/HamletTheHamster/Plotting-Data-in-Go>

The reader will find several GIFs which step through each spectrum in ascending pump–probe detuning at various frame rates. Readers are encouraged to view them for an animated perspective on how the spectra evolve with increasing pump–probe detuning, with special attention to transitions between Lorentzian and Fano-distorted line shapes.

B.4 Mini Experiment: Equal Contribution of Pump, Stokes, and Probe

Equation 3.1 gives the somewhat unintuitive result that the powers of the Pump, Stokes, and Probe waves contribute equally to the resulting scattered power of the Signal and invites verification with a miniexperiment. Initially, this experiment was motivated by a practical consideration: determination of whether the placement of a high power amplifier on any specific line of the setup (Pump, Stokes, or Probe) would offer any advantage over another.

To test this, we conducted a controlled experiment with a 1 mm carbon disulfide (CS_2) sample. For each measurement, one of the three source powers (Pump, Stokes, or Probe) was systematically reduced by 75% while holding the others constant and ensuring consistent experimental conditions across trials. Table B.3 shows the respective powers for each source during the three measurements, along with the multiplicative total contribution of the three powers for each measurement towards the generation of scattered power of the Signal.

Measurement	Pump Power (mW)	Stokes Power (mW)	Probe Power (mW)	Total (mW ³)
Pump Lower	19.190	32.210	54.560	3.372×10^4
Stokes Lower	76.600	8.020	54.650	3.359×10^4
Probe Lower	76.600	32.530	13.480	3.359×10^4

Table B.3: Power values for each source (Pump, Stokes, Probe) across the three measurements, with the multiplicative total power for each setup.

Figure B.6 displays the average results from these three measurements, plotted with error bars representing one standard deviation of the mean. For increased certainty, Figure B.7 presents the same data with error bars extended to two standard deviations, providing additional confidence in the reproducibility of the results. This experiment confirms that the scattered Signal power indeed depends equally on each of the three contributing wave powers, as expected from the theoretical framework. Consequently, boosting the power of any of the three sources affects the Signal power equally, allowing flexibility in pragmatic design across any of the three lines. Ultimately, this result reinforces the reliability of Equation 3.1 for predicting Signal power across a range of power distributions within practical settings.

1 mm CS2 CABS

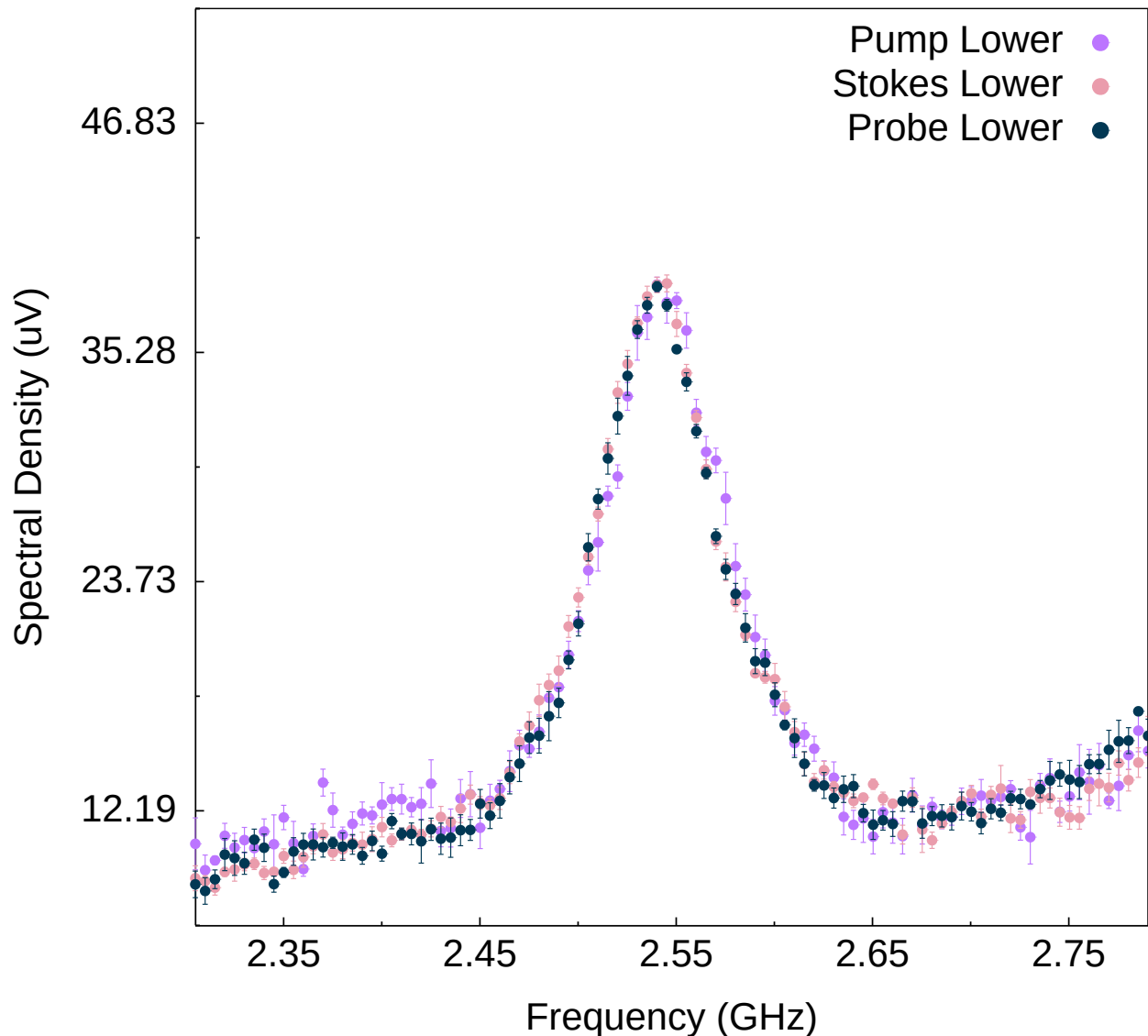


Figure B.6: Signal power contributions with error bars representing one standard deviation of the mean for each measurement.

1 mm CS2 CABS

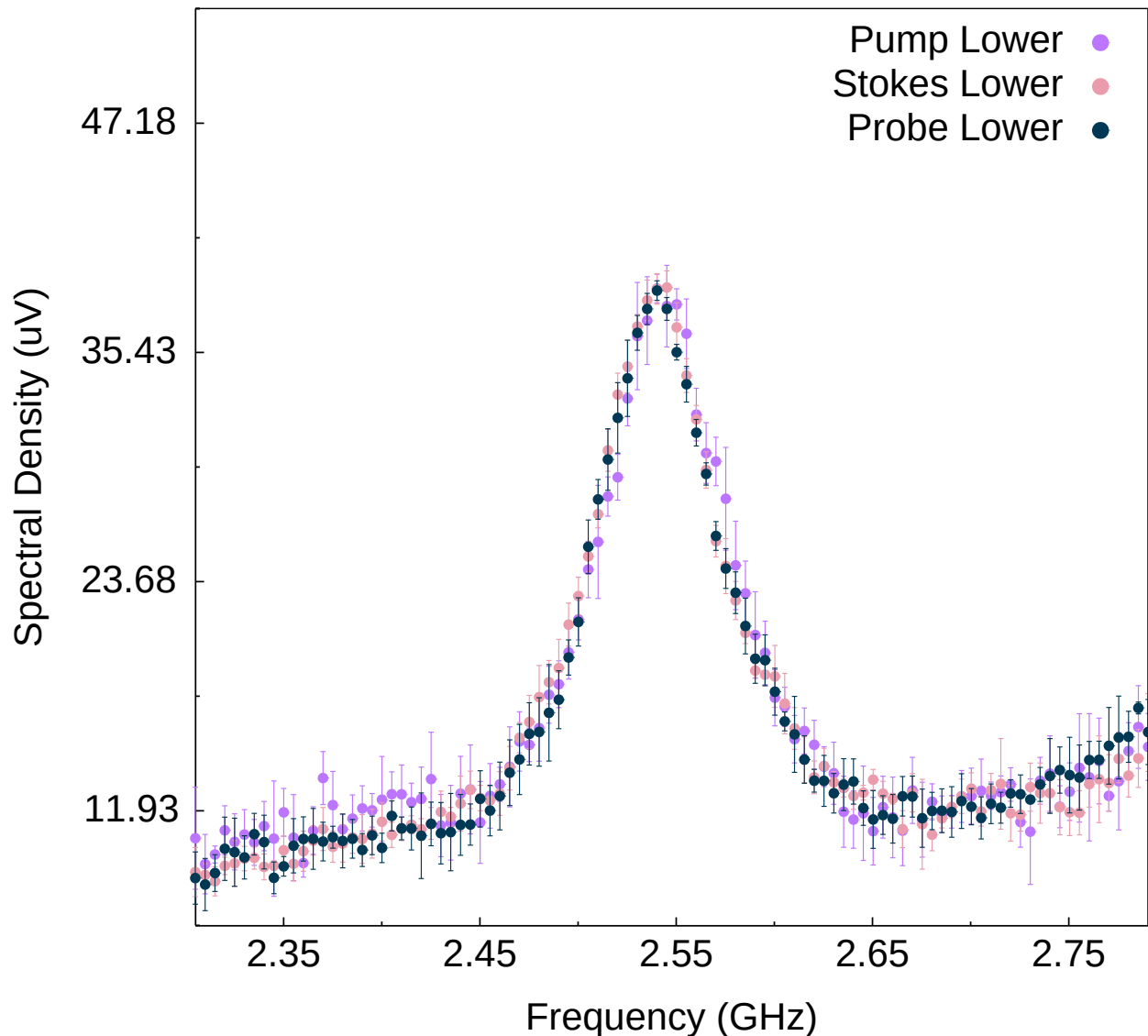


Figure B.7: Signal power contributions with error bars extended to two standard deviations of the mean for each measurement.

B.5 Data

Appendix C

Supplementary Information for Chapter 4

C.1 Fiber-Chip-Fiber Butt-Coupling Alignment

Appendix D

Code and Data Availability

D.1 Plotting Data In Go

Data plots presented in this dissertation were generated using custom programs written by the author in Golang or Python. The source code for these program, as well as all data collected and plots generated in support of the work presented in this dissertation, are publicly available on GitHub via the following link:

<https://github.com/HamletTheHamster/Plotting-Data-in-Go>

A video visualizing the evolution of data collection and development of functionality of the plotting program is available on YouTube:

<https://www.youtube.com/watch?v=PdoWVoJx2Vg>

References

- [1] Robert W Boyd. *Nonlinear Optics*. Academic Press, 2020.
- [2] Lord Rayleigh. On the light from the sky, its polarization and colour. *Phil Mag*, 41:274, 1871.
- [3] eg PA Franken, Alan E Hill, CW el Peters, and Gabriel Weinreich. Generation of optical harmonics. *Physical review letters*, 7(4):118, 1961.
- [4] Theodore H Maiman. Stimulated optical radiation in ruby. *nature*, 187(4736):493–494, 1960.
- [5] Joel N Johnson, Danielle R Haverkamp, Yi-Hsin Ou, Khanh Kieu, Nils T Otterstrom, Peter T Rakich, and Ryan O Behunin. Laser cooling of traveling-wave phonons in an optical fiber. *Physical Review Applied*, 20(3):034047, 2023.
- [6] K Kieu, L Schneebeli, RA Norwood, and N Peyghambarian. Integrated liquid-core optical fibers for ultra-efficient nonlinear liquid photonics. *Optics express*, 20(7):8148–8154, 2012.
- [7] Ryan O Behunin, Yi-Hsin Ou, and Khanh Kieu. Spontaneous forward brillouin scattering in carbon disulfide. *Physical Review A*, 99(6):063826, 2019.
- [8] RY Chiao, Ch H Townes, and BP Stoicheff. Stimulated brillouin scattering and coherent generation of intense hypersonic waves. *Physical review letters*, 12(21):592, 1964.
- [9] Benjamin J Eggleton, Christopher G Poulton, and Ravi Pant. Inducing and harnessing stimulated brillouin scattering in photonic integrated circuits. *Advances in Optics and Photonics*, 5(4):536–587, 2013.
- [10] AA Fotiadi, DA Korobko, and IO Zolotovskii. Brillouin lasers and sensors: Trends and possibilities. *Optoelectronics, Instrumentation and Data Processing*, 59(1):66–76, 2023.
- [11] Andrey Kobyakov, Michael Sauer, and Dipak Chowdhury. Stimulated brillouin scattering in optical fibers. *Advances in optics and photonics*, 2(1):1–59, 2009.
- [12] EP Ippen and RH Stolen. Stimulated brillouin scattering in optical fibers. *Applied Physics Letters*, 21(11):539–541, 1972.
- [13] Sergio Speziale, Hauke Marquardt, and Thomas S Duffy. Brillouin scattering and its application in geosciences. *Reviews in Mineralogy and Geochemistry*, 78(1):543–603, 2014.
- [14] Francesca Palombo and Daniele Fioretto. Brillouin light scattering: applications in biomedical sciences. *Chemical reviews*, 119(13):7833–7847, 2019.
- [15] JG Dil. Brillouin scattering in condensed matter. *Reports on Progress in Physics*, 45(3):285, 1982.
- [16] Benjamin J Eggleton, Christopher G Poulton, Peter T Rakich, Michael J Steel, and Gaurav Bahl. Brillouin integrated photonics. *Nature Photonics*, 13(10):664–677, 2019.
- [17] Robert Prevedel, Alba Diz-Muñoz, Giancarlo Ruocco, and Giuseppe Antonacci. Brillouin microscopy: an emerging tool for mechanobiology. *Nature methods*, 16(10):969–977, 2019.

- [18] Christina Conrad, Kelsey M Gray, Kimberly M Stroka, Imran Rizvi, and Giuliano Scarcelli. Mechanical characterization of 3d ovarian cancer nodules using brillouin confocal microscopy. *Cellular and molecular bioengineering*, 12:215–226, 2019.
- [19] Peter T Rakich, Charles Reinke, Ryan Camacho, Paul Davids, and Zheng Wang. Giant enhancement of stimulated brillouin scattering in the subwavelength limit. *Physical Review X*, 2(1):011008, 2012.
- [20] Flavien Gyger, Junqiu Liu, Fan Yang, Jijun He, Arslan S Raja, Rui Ning Wang, Sunil A Bhave, Tobias J Kippenberg, and Luc Thévenaz. Observation of stimulated brillouin scattering in silicon nitride integrated waveguides. *Physical review letters*, 124(1):013902, 2020.
- [21] Linfeng Yu, Chukun Huang, Ming Cheng, Kang Wang, Haotian Shi, Qiang Huang, and Junqiang Sun. On-chip stimulated brillouin scattering. *Chinese Optics Letters*, 22(2):020031, 2024.
- [22] Heedeuk Shin, Wenjun Qiu, Robert Jarecki, Jonathan A Cox, Roy H Olsson, Andrew Starbuck, Zheng Wang, and Peter T Rakich. Tailorable stimulated brillouin scattering in nanoscale silicon waveguides. *Nature communications*, 4(1):1–10, 2013.
- [23] Raphaël Van Laer, Bart Kuyken, Dries Van Thourhout, and Roel Baets. Interaction between light and highly confined hypersound in a silicon photonic nanowire. *Nature Photonics*, 9(3):199–203, 2015.
- [24] Eric A Kittlaus, Heedeuk Shin, and Peter T Rakich. Large brillouin amplification in silicon. *Nature Photonics*, 10(7):463–467, 2016.
- [25] Lionel Djadaojee, Albane Douillet, and Jules Grucker. Stimulated brillouin gain spectroscopy in a confined spatio-temporal domain (30 μm, 170 ns). *The European Physical Journal Applied Physics*, 89(3):30701, 2020.
- [26] Vitalyi E Gusev and Pascal Ruello. Advances in applications of time-domain brillouin scattering for nanoscale imaging. *Applied Physics Reviews*, 5(3), 2018.
- [27] A Gerakis, MN Shneider, and PF Barker. Coherent brillouin scattering. *Optics Express*, 19(24):24046–24054, 2011.
- [28] Ravi Pant, Enbang Li, D-Y Choi, CG Poulton, Stephen J Madden, Barry Luther-Davies, and Benjamin J Eggleton. Cavity enhanced stimulated brillouin scattering in an optical chip for multiorder stokes generation. *Optics letters*, 36(18):3687–3689, 2011.
- [29] Eric A Kittlaus, Nils T Otterstrom, and Peter T Rakich. On-chip inter-modal brillouin scattering. *Nature communications*, 8(1):15819, 2017.
- [30] Omer Shlomovits, Tomi Langer, and Moshe Tur. The effect of source phase noise on stimulated brillouin amplification. *Journal of Lightwave Technology*, 33(12):2639–2645, 2015.
- [31] PD Maker, RW Terhune, M Nisenoff, and CM Savage. Effects of dispersion and focusing on the production of optical harmonics. *Physical review letters*, 8(1):21, 1962.
- [32] RO Behunin, P Kharel, WH Renninger, H Shin, F Carter, E Kittlaus, and PT Rakich. Long-lived guided phonons in fiber by manipulating two-level systems. *arXiv preprint arXiv:1501.04248*, 2015.
- [33] Marc Nikles, Luc Thevenaz, and Philippe A Robert. Brillouin gain spectrum characterization in single-mode optical fibers. *Journal of Lightwave Technology*, 15(10):1842–1851, 1997.
- [34] Ugo Fano. Effects of configuration interaction on intensities and phase shifts. *Physical review*, 124(6):1866, 1961.
- [35] Mikhail F Limonov, Mikhail V Rybin, Alexander N Poddubny, and Yuri S Kivshar. Fano resonances in photonics. *Nature photonics*, 11(9):543–554, 2017.
- [36] Mikhail F Limonov. Fano resonance for applications. *Advances in optics and photonics*, 13(3):703–771, 2021.

- [37] Martin Kroner, Alexander O Govorov, Sebastian Remi, Benjamin Biedermann, Stefan Seidl, Antonio Badolato, Pierre M Petroff, Wei Zhang, R Barbour, BD Gerardot, et al. The nonlinear fano effect. *Nature*, 451(7176):311–314, 2008.
- [38] Andrey E Miroshnichenko, Sergej Flach, and Yuri S Kivshar. Fano resonances in nanoscale structures. *Reviews of Modern Physics*, 82(3):2257–2298, 2010.
- [39] Joo Hwan Ko, Jin-Hwi Park, Young Jin Yoo, Sehui Chang, Jiwon Kang, Aiguo Wu, Fang Yang, Sejeong Kim, Hae-Gon Jeon, and Young Min Song. Full-control and switching of optical fano resonance by continuum state engineering. *Advanced Science*, 10(32):2304310, 2023.
- [40] Linpeng Gu, Liang Fang, Hanlin Fang, Juntao Li, Jianbang Zheng, Jianlin Zhao, Qiang Zhao, and Xuetao Gan. Fano resonance lineshapes in a waveguide-microring structure enabled by an air-hole. *APL photonics*, 5(1), 2020.
- [41] Robert W Boyd, Kazimierz Rzaewski, and Paul Narum. Noise initiation of stimulated brillouin scattering. *Physical review A*, 42(9):5514, 1990.
- [42] Prashanta Kharel, Ryan O Behunin, William H Renninger, and Peter T Rakich. Noise and dynamics in forward brillouin interactions. *Physical Review A*, 93(6):063806, 2016.
- [43] D Rieger, S Günzler, M Spiecker, A Nambisan, W Wernsdorfer, and IM Pop. Fano interference in microwave resonator measurements. *Physical Review Applied*, 20(1):014059, 2023.